Title

Understanding the effects of nucleosome conformational dynamics on chromatin regulation

Author

Saunders, Hayden Samuel

Publication Date

2024

Peer reviewed|Thesis/dissertation

Understanding the effects of nucleosome conformational dynamics on chromatin regulation

by
Hayden Samuel Saunders

DISSERTATION
Submitted in partial satisfaction of the requirements for degree of
DOCTOR OF PHILOSOPHY

in

Biochemistry and Molecular Biology

in the

GRADUATE DIVISION
of the
UNIVERSITY OF CALIFORNIA, SAN FRANCISCO

Approved:

Signed by:
John D. Gross
723661740748414

John D. Gross

Chair

DocuSigned by:
Geeta Narlikar

Geeta J. Narlikar

DocuSigned by:
Danica Fujimori

Danica Fujimori

Signed by:
Hiten Madhani
9161290191 4492

Hiten Madhani

Committee Members

Acknowledgements

I am deeply grateful to so many wonderful people who have supported me personally and professionally to get to this point. I truly believe that I am the sum of all those who have helped me, and this work is a testament to the people listed here and countless others.

My parents have always provided me every opportunity in life, especially when it comes to pursuing an education. They saw from an early age a potential in me that they worked hard to nurture. Mom made sure I never became discouraged by disappointments, and Dad instilled in me a sense of discipline that allows me to achieve such things as this PhD. Faye as well saw my potential and always encouraged me to pursue a career in science as she had done. Not only this, but they always make it clear that they love me unconditionally and will support me no matter what. Although it may be easy to take that for granted, it is truly a massive blessing and privilege. Thank you so much. I would not be here without you.

I am extremely proud of the ways in which I see my grandparents' characteristics reflected in myself. Nana was a scientist in a time when women did not have the same opportunities to participate in this field. And even though she didn't stay in science professionally, her knowledge of and excitement about the natural world are the mark of a true scientist and something that always amazes me. Grandpa is an excellent engineer and is never afraid to take something apart to fix it. I feel this in my attraction towards biochemistry as a discipline, as I am always curious to understand the workings

of living things in granular detail. I have been so lucky to have had their emotional support throughout my PhD. Though they may not understand the ins and outs of what I do, they are always there for encouragement and to remind me how proud they are of me. I am so grateful that they could share in this experience with me.

I am so incredibly lucky to have three siblings whom I love so dearly and get along with so well. Kenneth, Nick and Sarah – we have all grown so much in these six and a half years, and I feel like it has brought about a new chapter in our lives. We have even added new family members in Danielle, Andrea and Henry (and hopefully more to come soon), who amplify the love I feel for each of you. I am so excited to continue to grow with you all and be a part of your lives.

Finally, to my extended Saunders, Williams and Pahlavan families, unfortunately I don't have the space here to thank every single one of you. But you all have been such integral parts of my life at different points. It is truly a mystery how life unfolds, and I am grateful for all you who have loved and supported me along the way.

Scientifically, I have been so incredibly privileged. My journey started as a high school student interning at the NIH in the lab of Silvio Gutkind under the careful guidance of Constantinos Mikelis. Dinos spent such time and care to teach me the basic principles of wet lab work, and I remain inspired by how he managed to do that on top of his many other responsibilities.

At UNC, I was lucky enough to be guided by two incredible scientists and teachers: Kelly and Brian Hogan. They created a home for us at UNC and gave us the tools to do so many amazing things. This led to my work in the labs of Paul and Amy Maddox, where I was helped along by an amazing graduate student in Anne Marie Ladouceur. It was here that I first developed curiosity and excitement for doing science. It was such an incredible privilege and opportunity, and it would not have been possible without these amazing people.

Then my journey led me back to the NIH, into the lab of Alexander Kelly. Alex believed in me way more than I think I believed in myself. It was during this time that he honed my excitement into skills in the lab. He never thought of me as just a postbac and provided me so many incredible opportunities to do amazing science, while training and teaching me at every step of the way. Though it was only two years, my time in Alex's lab had such a profound impact on my growth as a scientist and set me up for success in graduate school.

At UCSF, I have been so lucky for the opportunity to work with such inspiring and caring scientists who are truly at the forefront of their fields. Geeta Narlikar is unwavering in her principles of doing science rigorously while also treating people the right way. Her work and career are a testament to those ideals, and I hope that I can continue to do them justice. My mentors and lab mates in the Narlikar lab are all reflections of Geeta's vision, and I am eternally grateful for their help and companionship. None of this work would have been possible without them.

Contributions

Chapter 2 is adapted from an unpublished manuscript with the following authors: Hayden S. Saunders, Un Seng Chio, Camille M. Moore, Vijay Ramani, Yifan Cheng and Geeta J. Narlikar.

Chapter 3 is unpublished work which includes experiments performed by Michael J. Trnka.

Understanding the effects of nucleosome conformational dynamics on chromatin regulation

Hayden Samuel Saunders

Abstract

The nucleosome is a highly dynamic macromolecular complex that is at the center of regulating access to genetic information in eukaryotes. The structural dynamics of nucleosomes are an ensemble of the dynamics of its component parts: the globular histone octamer core, the wrapped DNA, and the flexible histone tails. The coordination of these dynamics presents modes of regulation of nucleosome function. Although nucleosomes have long been considered exceptionally static and stable complexes, it has become clear that this is not the case. This thesis builds upon past work highlighting the central importance of understanding both the nature of nucleosome dynamics and the ways in which they are regulated. This thesis first addresses how nucleosome conformational dynamics are regulated by a class of nuclear proteins termed architectural proteins. Nuclear architectural proteins globally alter nucleosome structure and dynamics to induce effects on chromatin genome wide. The two most abundant nuclear architectural proteins, the linker histone H1 and HMGB1 (high mobility group box 1), compete with one another in this respect. We present a molecular model for how HMGB1 and H1 compete at many scales. We find that HMGB1 and H1 co-occupy nucleosomes and chromatin and modulate one another's effect on DNA accessibility and mesoscale chromatin dynamics. This leads to a model wherein the dynamics of nucleosomes and chromatin can be precisely tuned by influencing the competition between these two proteins. This model also highlights the effect of altering

atomic-scale nucleosome conformational dynamics on the mesoscale function of chromatin and uncovers a global role for nucleosome conformational dynamics in chromatin regulation. In addition to the work on nuclear architectural proteins, we design a proteomics-based screening platform to identify novel regulators of nucleosome conformational dynamics. Initial results from this platform implicate a number of interesting chromatin proteins and complexes as potentially having an effect on the conformational dynamics of nucleosomes. These results also imply that nucleosome conformational dynamics can be a point of regulation in a wide variety of chromatin processes. Finally, this screening platform is highly adaptable. Future iterations of this screen could target specific subsets of chromatin, focus on the activities of chromatin modifying enzymes, and shed light on potential allosteric pathways of the nucleosome itself. Overall, this thesis explores the nature and the role of nucleosome conformational dynamics in regulating a wide variety of chromatin processes.

Table of Contents

List of Figures

List of Tables

Chapter 1: Introduction

1.1 Chromatin and nucleosomes are dynamic ensembles

In eukaryotes, genetic material is packaged into a nucleoprotein milieu known as chromatin. The basic unit of chromatin is the nucleosome, which consists of an octamer of histone proteins around which is wrapped ~147 base pairs (bp) of DNA. The primary function of histone proteins is to compact the roughly 2 meters of DNA contained within each cell into the nucleus, which is approximately 10 μm in diameter. Secondarily, the presence of nucleosomes serves as a steric barrier to accessing genetic material, and in this way, is a key point of regulation for nearly every nuclear process. Understanding the basic biophysical principles that govern nucleosomes is therefore essential for our understanding the cellular function of chromatin.

Macromolecules like DNA and proteins are essentially long polymer chains of basic building blocks – nucleotides and amino acids. These building blocks are strung together into long polymers by series of covalent bonds (phosphodiester in the case of DNA and peptide bonds in the case of proteins). Covalent bonds are flexible, so macromolecules, which string together hundreds to thousands of bonds, have vast degrees of freedom allowing them to flexibly adopt a variety of shapes or conformations. The array of conformations exhibited by a macromolecule is called a conformational ensemble and can be represented by a free energy landscape (Figure 1.1). Low energy minima represent more stable conformations which are separated by high energy transitional barriers. Individual molecules dynamically sample all available

conformations by transiently overcoming high energy barriers. Understanding the conformational states that are accessible to macromolecules and how these various states are regulated or modified by other factors is key to understanding their function.

Nucleosome structure, as any other large macromolecular complex, can be defined by a number of dynamic, interconverting conformational states (Figure 1.1A and 1.1B). Further, the nucleosome is a complex made up of many individual molecules – eight histone proteins forming a globular core that wraps ~147bp of DNA and highly flexible histone tails which protrude from the core. All these individual components contain their own unique conformational dynamics, which are highly correlated with one another when combined to form a nucleosome. Understanding the coordinated dynamics of such a macromolecular complex is essential to understanding its function and regulation. However, the conformational dynamics of nucleosomes remains largely understudied.

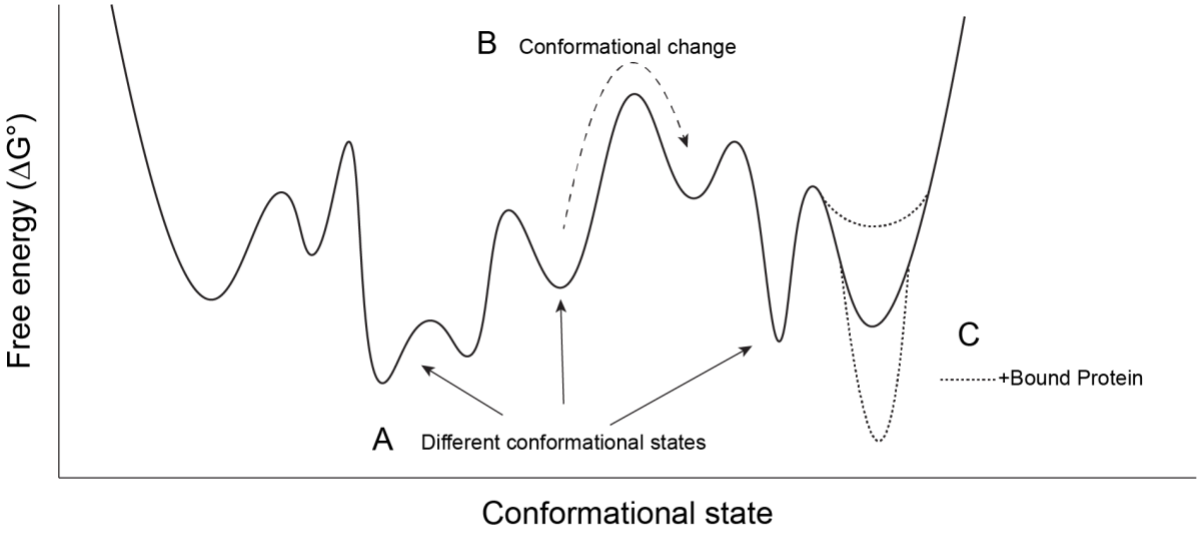

Figure 1.1 Free energy landscape of nucleosome conformations
(A) Different conformations of nucleosome structure are shown as free energy minima within the energy landscape. **(B)** Individual molecules undergo rapid conformational changes to sample many states by overcoming energy barriers. **(C)** Binding of additional proteins to nucleosomes can change the free energy landscape by stabilizing and/or destabilizing certain conformations.

1.2 The importance of nucleosome conformational dynamics

Since the first high-resolution glimpse at nucleosome structure in 1997, a growing number of nucleosome structures have been determined. These structures show nucleosomes with various DNA sequences, bound by different chromatin proteins, or composed of variant histones. Despite this variability, the structure of the octamer core and the majority of the ~147bp of wrapped DNA appears largely the same. This has naturally led to the assumption that the nucleosome, unlike all other macromolecules, is an exceptionally stable and static structure. However, much work has been put into highlighting the importance of the dynamic nature of nucleosome structure.

Even before a high-resolution structural view of the nucleosome had been obtained, foundational biochemical work revealed the conformational flexibility of nucleosomes. Early studies on purified nucleosomes showed how a cysteine residue within the core histone H3 can be chemically modified despite the fact that this cysteine is not solvent exposed in the canonical nucleosome structure, suggesting the presence of non-canonical nucleosome conformations (Prior et al., 1983). This first confirmed that nucleosomes, and specifically the histone octamer core, can undergo conformational rearrangements which could potentially influence gene expression. Later, pioneering work studying the accessibility of a restriction enzyme site buried within the nucleosomal DNA showed that nucleosomal DNA transiently unwraps from the histone octamer core (Anderson and Widom, 2000; Polach and Widom, 1995). These studies established that nucleosomes are indeed highly dynamic complexes and suggested that the dynamics of different components of nucleosomes could be related.

The two main structural techniques that have yielded the vast majority of nucleosome structures, x-ray crystallography and cryo-electron microscopy (cryo-EM), are performed under freezing conditions, which limits dynamics, and produce static views of macromolecular structure. Despite their incredible utility, this limits our imaginative ability to envision conformational dynamics of these macromolecules. Furthermore, x-ray and cryo-EM structures are obtained by averaging together many particles, which may exist in various conformations, into an average structure. However, this can actually be used as an advantage by analyzing the variability among all of the individual particles and sub-dividing into distinct conformations. Applying this technique to nucleosomes actually reveals remarkable heterogeneity in conformational states (Bilokapic et al., 2018a, 2018b). This analysis also reveals the coordination in the conformational dynamics of the various parts of the nucleosome. Transient unwrapping of nucleosomal DNA is shown to correlate with conformational changes in the histone octamer, suggesting conserved allosteric pathways for conformational rearrangement of the nucleosome as a whole. This high level of coordination is further validated by all-atom, microsecond-scale molecular dynamics simulations of nucleosomes, which reveal similar coordinated conformational changes (Armeev et al., 2021).

Equally important to understanding the conformational dynamics of nucleosomes in isolation is understanding the influence of other chromatin proteins on these dynamics (Figure 1.1C). This provides clues as to how the dynamics of nucleosomes may be regulated. It has been demonstrated that the wrapping of DNA around histones can be

altered by the ATP-dependent chromatin remodeling enzyme SWI/SNF (Côté et al., 1994; Imbalzano et al., 1994; Kwon et al., 1994; Lorch et al., 1998). However, to understand the regulation of nucleosome dynamics, it is important to understand how these changes in the DNA wrapping are accommodated by or induced by conformational changes within the histone octamer core.

A third structural technique, nuclear magnetic resonance (NMR), is much better suited for understanding protein dynamics. However, performing NMR on larger complexes has, until recently, been incredibly challenging. The advent of ^{1}H-^{13}C methyl-transverse relaxation optimized NMR spectroscopy (methyl-TROSY) facilitates selective detection of labeled Ile, Leu, and Val (ILV) residues within large macromolecules in a deuterated background (Rosenzweig and Kay, 2014; Tugarinov et al., 2003). This technique enabled for the first time a dynamic, NMR-based dynamic analysis of nucleosome structure, specifically of the buried ILV residues within the histone octamer core (Kato et al., 2011). In support of this, certain mutations within the histone core were shown to make the octamer more dynamic by methyl-TROSY NMR (Kitevski-LeBlanc et al., 2018). This powerful technique enabled solution-based, high-resolution structural understandings of nucleosome conformational dynamics and the factors that regulate it.

Methyl-TROSY NMR has since been applied to understand how a variety of nucleosome-binding proteins influence nucleosome conformational dynamics. It was first used to map the binding site of the architectural protein HMGN2 to the acidic patch on the histone octamer core (Kato et al., 2011). Since this initial study, methyl-TROSY

NMR has also been used to study how the ATP-dependent chromatin remodeling enzyme SNF2h and the *S. pombe* heterochromatin protein Swi6 interact with and deform the nucleosome (Sanulli et al., 2019; Sinha et al., 2017). Interestingly, these analyses revealed altered conformational dynamics within the histone octamer core upon binding of either of these two proteins. These studies further highlighted the importance of conformational changes within the histone octamer core by targeting dicysteine crosslinks to limit structural rearrangement of the nucleosome and inhibit SNF2h and Swi6's activity on nucleosomes.

As a whole, these studies have brought nucleosome conformational dynamics into the forefront of nucleosome structure and regulation. However, there is much left unexplored about the function of nucleosome conformational dynamics and how it may be regulated.

1.3 Open questions on nucleosome conformational dynamics

Although in depth structural studies have started to reveal a view of what the different conformational states of the nucleosome look like, how various chromatin proteins influence these conformations has been less studied. SNF2h and Swi6 have both been shown to induce conformational dynamics of the histone octamer core using methyl-TROSY NMR (Sanulli et al., 2019; Sinha et al., 2017). These studies are highly materially intensive, expensive and difficult, so they cannot realistically be used to study every chromatin protein that may interact with the nucleosome. Therefore, to ask the question of whether other proteins influence the conformational landscape of nucleosomes new methods must be developed that lend to high throughput studies.

These will not only reveal what other proteins are sensitive to nucleosome conformational dynamics but may also reveal regulatory patterns of nucleosome dynamics. This work would also highlight the importance of nucleosomes conformational dynamics in a variety of nuclear contexts that have yet to be studied through the lens of nucleosome conformational dynamics.

Although it is important to identify new regulators of nucleosome dynamics, there already exist a class of proteins known to regulate nucleosome structure and dynamics globally. Architectural proteins are the most abundant non-histone proteins within the eukaryotic nucleus. *In vivo*, this class of proteins is known to have global effects on all processes that need access to nucleosomal DNA, such as transcription, DNA replication and DNA damage repair. These proteins have the potential to globally regulate nucleosome conformational dynamics in the nucleus, however, this possibility has not been thoroughly explored.

The two most abundant nuclear architectural proteins, high mobility group box 1 (HMGB1) and the linker histone H1, are thought to compete to regulate nucleosomes and chromatin. HMGB1 is thought to enhance nucleosome and chromatin dynamics generally, while H1 is thought to inhibit them. However, the molecular mechanism of their competition and how they compete to influence nucleosome conformational dynamics has not been studied. A molecular mechanism of this competition would further our understanding not only of these two proteins but of the importance of regulating global nucleosome conformational dynamics.

Chapter 2: HMGB1 restores a dynamic chromatin environment in the presence of linker histone by deforming nucleosomal DNA

2.1 Abstract

The essential architectural protein HMGB1 increases accessibility of nucleosomal DNA and counteracts the effects of linker histone H1. However, HMGB1 is less abundant than H1 and binds nucleosomes more weakly, raising the question of how it competes with H1. Here, we find that HMGB1 increases nucleosomal DNA accessibility without displacing H1. HMGB1 also increases the dynamics of condensed, H1-bound chromatin. Unexpectedly, cryo-EM structures show HMGB1 bound at internal locations on nucleosomes and local DNA distortion. These sites are away from where H1 binds, explaining how HMGB1 and H1 can co-occupy a nucleosome. Our findings suggest a model where HMGB1 counteracts the effects of H1 by distorting nucleosomal DNA and by disrupting interactions of the H1 C-terminal tail with DNA. Compared to mutually exclusive binding, co-occupancy by HMGB1 and H1 allows greater diversity in dynamic chromatin states. More generally these results explain how architectural proteins acting at the nucleosome scale can have large effects on chromatin dynamics at the mesoscale.

2.2 Introduction

In eukaryotes, the fundamental unit of chromatin is a nucleosome, which is composed of ~147 base pairs (bp) of DNA wrapped around an octamer of histone proteins. Nucleosome formation typically inhibits access to DNA for processes such as transcription, replication or DNA repair (Lorch et al., 1987). It is well known that ATP-

dependent chromatin remodelers facilitate access to nucleosomal DNA (Clapier et al., 2017). There also exist ATP-independent mechanisms that regulate the intrinsic dynamics of nucleosomal DNA through the actions of architectural proteins (Anderson and Widom, 2000; Armeev et al., 2021; Bilokapic et al., 2018a, 2018b; Fyodorov et al., 2018; Polach and Widom, 1995; Thomas and Travers, 2001). In mammalian cells the two most abundant architectural proteins, HMGB1 (high mobility group box 1) and linker histone H1, regulate chromatin through opposing effects (Thomas and Stott, 2012). While the expression of HMGB1 is correlated with chromatin decompaction and transcriptional activation, the presence of H1 is associated with chromatin compaction and transcriptional repression (Fyodorov et al., 2018; Ogawa et al., 1995; Aizawa et al., 1994; Ju et al., 2006). Examples of transitions from HMGB1-bound chromatin to H1-bound chromatin have been observed during *Xenopus* and *Drosophila* embryonic development (Ner and Travers, 1994; Nightingale et al., 1996). Further, H1 turnover dynamics have been shown to be sensitive to HMGB1 concentration *in vivo* (Catez et al., 2004). Importantly, in stem cells, where HMGB1 is most highly expressed, H1 turns over more rapidly compared to differentiated cells (Meshorer et al., 2006; Müller et al., 2004). These results imply that the relative activities of HMGB1 and H1 are critical for defining cell identity. Despite the biological significance, the molecular basis for how HMGB1 and H1 counteract each other's activities is not known.

In current models it has been proposed that HMGB1 and H1 directly compete because they bind nucleosomes in a mutually exclusive manner near the entry/exit site of DNA (Thomas and Stott, 2012; Nightingale et al., 1996; Catez et al., 2004; Cato et al., 2008;

An et al., 1998). However, even at its highest expression level, HMGB1 is present in the nucleus at 10-fold lower concentration, has ~1000-fold weaker affinity for nucleosomes and shorter residence times on chromatin than H1 (Bonaldi et al., 2002; Duguet and de Recondo, 1978; Falciola et al., 1997; Phair et al., 2004; Scaffidi et al., 2002; Ueda et al., 2004; White et al., 2016). These differences raise the question of how HMGB1 effectively competes with H1 for the same binding site. Additionally, several structures exist of linker histones bound to nucleosomes, which explain how H1 inhibits nucleosomal DNA unwrapping (Song et al., 2014; Zhou et al., 2013). In comparison, there are no structures of HMGB1 bound to nucleosomes because its weak affinity for nucleosomes and high dissociation rates make it difficult to capture stable structures. A better understanding of how HMGB1 interacts with and perturbs nucleosome structure will enable a deeper understanding of how HMGB1 and H1 compete.

What is known about HMGB1's interaction with the nucleosome is based on synthesizing careful studies with a variety of substrates. The mammalian HMGB1 consists of two HMG box domains, which bind DNA without sequence specificity. Each box contains two hydrophobic residues that intercalate into the minor groove of DNA and induce a bend in the DNA (Thomas and Travers, 2001). HMGB1 also contains a C-terminal autoinhibitory domain consisting of 30 consecutive negatively charged Asp and Glu residues, which mimics DNA to occlude the DNA binding interface of the HMG boxes (Figure 2.1A) (Knapp et al., 2004; Stott et al., 2010; Watson et al., 2007). Therefore, DNA bound by HMGB1 is in competition with the auto-inhibitory C-terminal tail, resulting in a high off rate and low affinity. These binding and bending dynamics are

how HMGB1 lowers the persistence length of DNA to make it more flexible (McCauley et al., 2007). Additionally, the autoinhibition of HMGB1's C-terminal tail is relieved by interaction with the H3 tail (Kawase et al., 2008; Ueda et al., 2004; Watson et al., 2014). This work has led to the hypothesis that HMGB1 promotes unwrapping of nucleosomal DNA using its ability to bend DNA (Agresti and Bianchi, 2003; Travers, 2003; Watson et al., 2014). Indeed, yeast (Hmo1 and Nhp6) and Drosophila (HMG-D) homologs of HMGB1 partially unwrap nucleosomal DNA (McCauley et al., 2019; Ragab and Travers, 2003). Interestingly, H1 also relieves HMGB1's autoinhibition via direct interaction of their respective C-terminal tails, raising questions about a direct competition model (Cato et al., 2008). However, to date, competition between HMGB1 and H1 has not been studied *in vitro* on mononucleosomes, so other modes of competition have not been tested.

Here, to obtain a molecular understanding of how HMGB1 and H1 influence each other's activities, we study their impact on reconstituted mononucleosomes and nucleosomal arrays. Using a quantitative assay to measure the transient unwrapping of nucleosomal DNA and cryo-electron microscopy (cryo-EM) to determine the first structures of HMGB1 on nucleosomes, we find that HMGB1 and H1 do not compete for binding. Rather, our data suggest that HMGB1 binds and deforms DNA at multiple sites along the nucleosomal and flanking DNA, counteracting H1's inhibition of DNA accessibility without displacing it. We further show that HMGB1 increases the dynamics of H1 bound to condensed chromatin and of H1-bound chromatin itself. Overall, our findings provide a structural explanation for how HMGB1 affects nucleosomal DNA and

offer a molecular mechanism for how HMGB1 and H1 counter each other's activities to regulate chromatin dynamics at the atomic and mesoscales. This mechanism, based on binding and conformational equilibria, represents a distinct and ATP-independent mechanism for regulating global chromatin accessibility and dynamics.

2.3 Results

2.3.1 Quantitative assay to measure impact of HMGB1 on nucleosomal DNA unwrapping

Previous studies have shown that HMG box-containing proteins enhance unwrapping of nucleosomal DNA (Dodonova et al., 2020; McCauley et al., 2019; Ragab and Travers, 2003). To quantitatively test how human HMGB1 affects this process, we adapted a restriction enzyme accessibility (REA) assay, that has been used to measure intrinsic DNA unwrapping within a nucleosome (Polach and Widom, 1995). In this assay a restriction enzyme site is placed within the nucleosomal DNA and the transient unwrapping of DNA from the octamer core is measured by the rate of restriction enzyme cutting (Figure 2.1B). DNA unwrapping preferentially occurs near the entry/exit sites of nucleosomal DNA, where fewer histone-DNA interactions need to be disrupted to make the DNA accessible (Anderson and Widom, 2000). Given that HMGB1 has been hypothesized to bind near the entry exit site (An et al., 1998; Nightingale et al., 1996), we used nucleosomes with 10 base pairs (bp) of flanking DNA on either side of the Widom 601 nucleosome positioning sequence, which was modified to contain a PstI restriction enzyme site centered at position 137 (10/10-Pst137, Figure 2.1B). We find that restriction enzyme cleavage is enhanced in the presence of HMGB1 (Figure 2.1C and 2.1D), consistent with HMGB1's role in increasing DNA unwrapping.

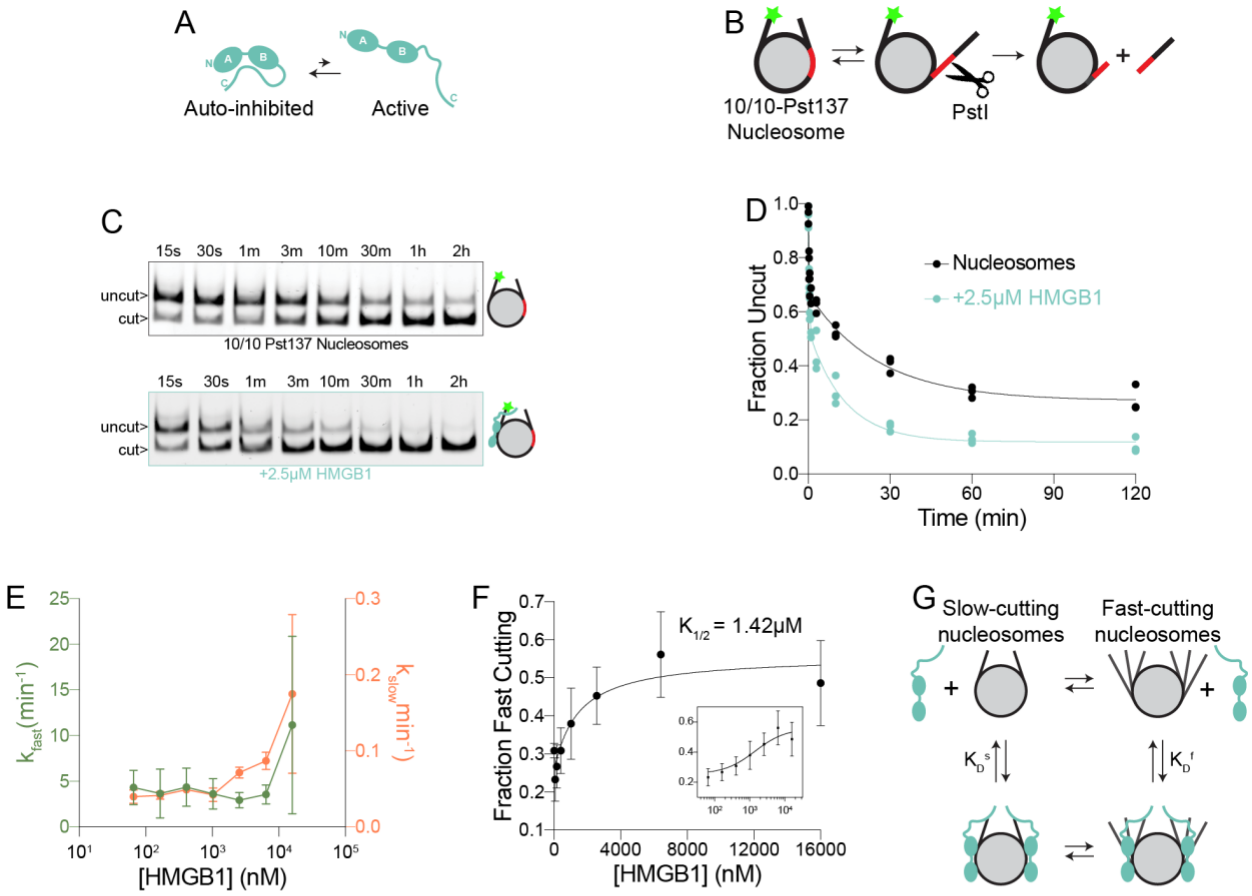

Figure 2.1 HMGB1 grants access to nucleosomal DNA
(A) A schematic of autoinhibition of HMGB1's DNA binding A and B-boxes by the negatively charged C-terminal tail. **(B)** A schematic of the restriction enzyme accessibility (REA) assay showing how nucleosomal DNA cutting by the restriction enzyme PstI occurs when nucleosomal DNA transiently unwraps from the octamer core. The green star represents the fluorescent label on the end of the DNA. **(C)** Representative gels of time courses of REA on 10/10-Pst137 nucleosomes with (bottom) and without (top) the presence of 2.5μM HMGB1. PstI cleavage results in the appearance of the lower, cut band over time. **(D)** Quantification of three replicate experiments of (B). The fraction of DNA that remains uncut is plotted as a function of time. The data for all three replicates are fit by a two-step exponential decay function. **(E)** Rate constants (k_{fast} and k_{slow}) for REA experiments on 10/10-Pst137 nucleosomes are shown as a function of HMGB1 concentration. Error bars represent the standard deviation for three separate replicates. **(F)** The fraction of nucleosomes that are described by k_{fast} is plotted as a function of HMGB1 concentration. Error bars represent the standard deviation for three separate replicates. Curve represents a fit by an equation derived from the model in (G). An overall half-maximal concentration of HMGB1 for its effect is 1.42μM ($K_{1/2}$). Inset shows the same plot with a logarithmic x-axis. **(G)** A schematic of a model showing a slow and a fast-cutting population of nucleosomes that interconvert slowly on timescale of PstI cutting and are bound by HMGB1 with different affinities. K_D^s is 2.4μM while K_D^f is 650nM. K_D's are derived from the equations in Materials and Methods.

It has previously been shown that HMGB1 prefers the presence of flanking DNA to interact with nucleosome substrates (Bonaldi et al., 2002; Ueda et al., 2004). To assess whether flanking DNA is also essential for HMGB1's effect on nucleosomal DNA unwrapping, we performed REA assays on nucleosomes with asymmetric flanking DNA (0/10 or 10/0). We found that HMGB1 enhances restriction enzyme cutting on both

substrates (Figure S2.1A and S2.1B). Although nucleosomal DNA is slightly less accessible when there is no flanking DNA proximal to the PstI cut site (10/0-Pst137, Figure S2.1B), HMGB1 still enhances restriction enzyme cutting on these nucleosomes. This suggests that HMGB1 enhances the existing unwrapping dynamics of nucleosomal DNA.

These results prompted us to look more closely at how exactly HMGB1 interacts with nucleosome substrates. In electrophoretic mobility shift-based binding experiments using fluorescently end-labelled nucleosomes, HMGB1 produces two up-shifted bands (Figure S2.2A). The two bands are consistent with a 2:1 stoichiometry of HMGB1 on nucleosomes. Interestingly, this two-step binding pattern is observed when HMGB1 binds symmetric 10/10 and asymmetric 0/10 nucleosomes (Figure S2.2A), suggesting that symmetric flanking DNA is dispensable for HMGB1's stoichiometry. Additionally, there is minimal effect on nucleosome affinity when removing one half of the flanking DNA, while removing all flanking DNA causes a 10-fold decrease in affinity (Figure S2.2B and S2.2C). Yet HMGB1 still promotes detectable enhancement of DNA unwrapping on core nucleosomes (Figure S2.1C). Overall, these results indicate that while flanking DNA increases the affinity of HMGB1 for nucleosomes, it is not essential for HMGB1's activity on nucleosomes, suggesting that other interactions with the nucleosome also facilitate HMGB1's activity.

It is known that the HMGB1 C-terminal tail interacts with the histone H3 N-terminal tail (Kawase et al., 2008; Ueda et al., 2004; Watson et al., 2014). It is also known that the

H3 tail interacts with nucleosomal DNA and inhibits DNA accessibility (Ghoneim et al., 2021; Polach et al., 2000). Therefore, it has been hypothesized that the interaction between the HMGB1 C-terminal tail and the H3 tail could result in sequestration of the H3 tail and relief of autoinhibition by HMGB1's C-terminal tail, both of which would increase HMGB1's ability to unwrap DNA (Watson et al., 2014). However, the H3-tail interaction may also provide an additional anchor to localize HMGB1 to a nucleosome. To test this possibility we deleted the C-terminal tail of HMGB1 (HMGB1-ΔC). HMGB1-ΔC does not yield the two-step nucleosome binding pattern of wildtype HMGB1 and instead binds non-specifically at a much higher stoichiometry and affinity (Figure S2.2A). Additionally, HMGB1-ΔC inhibits restriction enzyme cutting (Figure S2.3A and S2.3B), likely due to steric inhibition by the HMG boxes bound non-specifically to nucleosomal DNA. These results raise the possibility the interaction between the HMGB1 C-terminal tail and the histone H3 N-terminal tail localizes HMGB1 near the entry/exit site in addition to relieving auto-inhibition.

2.3.2 HMGB1 selectively stabilizes a nucleosome conformation with exposed nucleosomal DNA

In all REA experiments, we observe that nucleosomal DNA cutting contains two kinetic phases, suggesting that nucleosomes exist in two conformations that interconvert more slowly than cutting by PstI. In this model, one of the conformations is cut more rapidly (fast-cut) than the other (slow-cut), with respective rate constants of kfast and kslow. Interestingly, kfast is similar to the rate constant of cutting naked DNA (Figure S2.3D and S2.3E), suggesting that the fast-cut conformation has nucleosomal DNA at position 137 that is fully accessible to PstI. The fast cut population is not due to contaminating

free DNA as we do not detect substantial free DNA in our assembled nucleosomes (Figure S2.3C).

To investigate how HMGB1 influences these populations of nucleosomes, we performed REA at a range of HMGB1 concentrations and compared the rate constants of the fast and slow-cut populations (k_{fast} and k_{slow}) as a function of HMGB1 concentration (Figure S2.1D and S2.1E). To our surprise, we found that the magnitude of k_{fast} or k_{slow} was not substantially dependent on the concentration of HMGB1 (Figure 2.1E). Instead, the fraction of nucleosomes that were cut fast increased with increasing concentrations of HMGB1, indicating that at higher HMGB1 concentrations a greater population of nucleosomes have more accessible DNA. The increase in the fast cut fraction as a function of HMGB1 concentration resembles a binding curve (Figure 2.1F), implying that HMGB1 binding correlates with an increase in the population of fast-cutting nucleosomes. To quantify this effect, we fit a model to the data whereby HMGB1 binds the fast-cut nucleosomes more strongly than the slow-cut nucleosomes, resulting in shift in the equilibrium towards the fast cut population when nucleosomes are fully bound by HMGB1 (Figure 2.1G). This analysis revealed that HMGB1 has a roughly 4-fold binding preference for fast-cut over slow-cut nucleosomes (Figure 2.1G). Additionally, the analysis showed that 50% of HMGB1's stimulatory effect on nucleosomal DNA unwrapping occurred at ~1.4 μM, a $K_{1/2}$ value that is comparable to the K_D measured for HMGB1 to nucleosomes (Figure S2.2C). Overall, these results are consistent with a model where HMGB1 increases nucleosomal DNA accessibility by preferentially stabilizing fast-cut nucleosomes.

2.3.3 Cryo-EM structures of HMGB1 bound to nucleosomes imply transient interactions at multiple sites

To date there are structures of HMGB1 bound to DNA but no structures of HMGB1 bound to nucleosomes (Sánchez-Giraldo et al., 2015; Stott et al., 2006). A key challenge in capturing nucleosome bound structures is the weak affinity of HMGB1. While cross-linking is often used to stabilize weak chromatin binding proteins for cryo-electron microscopy (cryo-EM) we wanted to preserve any effects of HMGB1 on nucleosome dynamics. Therefore, we optimized the cryo-EM protocol to visualize how HMGB1 interacts with a nucleosome without cross-linking. We collected a cryo-EM dataset of 0/10 nucleosomes bound by HMGB1. Despite HMGB1's low affinity to this substrate, we were able to determine a 3D reconstruction where we detect one HMG box bound directly to the nucleosomal DNA at superhelical location (SHL) -2 on the nucleosomal DNA (Figure 2.2A, 2.2B, S2.4, and S2.5). Surprisingly, unlike previous data predicting HMGB1 to interact near the entry/exit site (An et al., 1998; Nightingale et al., 1996), we see HMGB1 interacting directly with the nucleosome at an internal site. This position is notably similar to recent cryo-EM structures of the related transcription factors SOX2 and SOX11 (Dodonova et al., 2020). However it is noteworthy that unlike the SOX proteins, this structure of an ancestral HMG box protein shows binding to this site in a sequence-independent manner. The ability to bind an internal nucleosomal site such as SHL-2 may therefore more generally represent an intrinsic capability of HMG box domains.

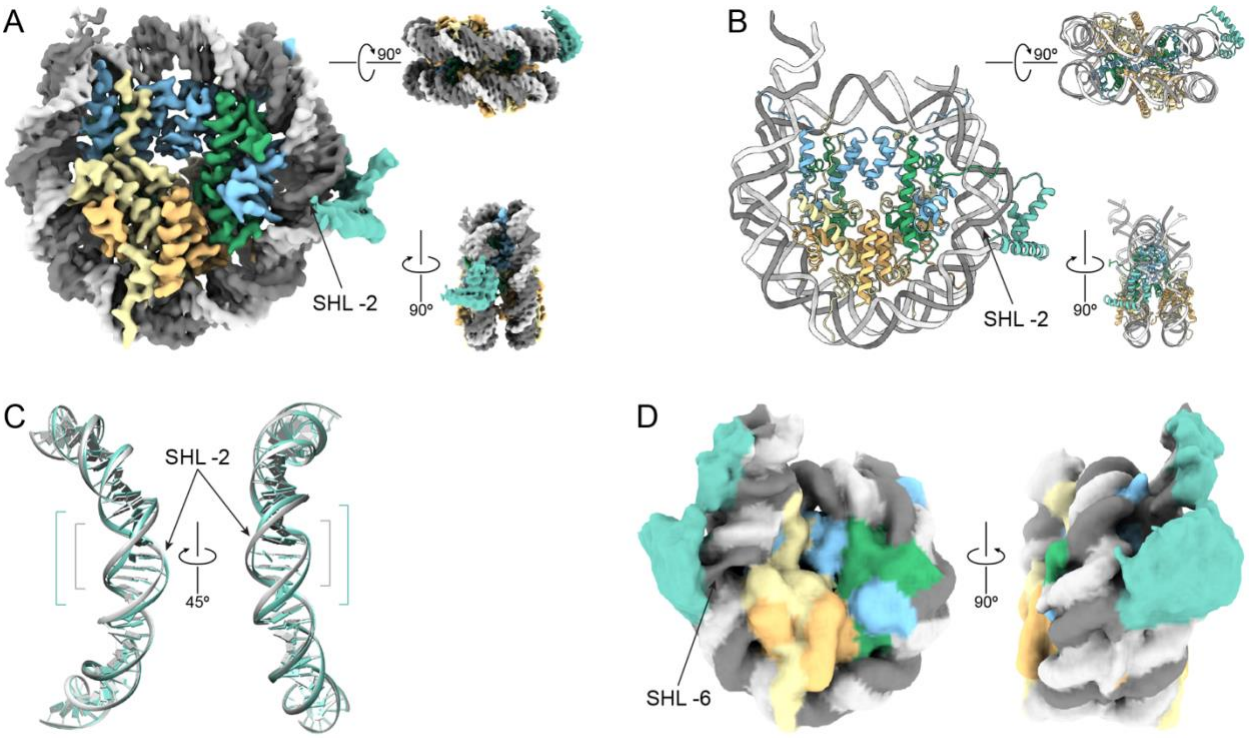

Figure 2.2 HMGB1 distorts nucleosomal DNA at multiple sites
(A) Cryo-EM density map of the A box of HMGB1 bound to a 0/10 nucleosome at SHL -2 at 2.9Å resolution. **(B)** Atomic model built using the density in (A). **(C)** A comparison of the DNA bound by HMBG1 at SHL -2 (gray) to the unbound DNA at SHL +2 (teal), showing the widening of the minor grove by the HMG box. **(D)** An additional cryo-EM class revealed by cryoDRGN showing extra density for HMGB1 bound at SHL -6.

While the local resolution of the HMG box density was insufficient for *de novo* model building, we find that the density most likely represents box A of HMGB1 by docking previously determined models of HMGB1 box A and box B (PDB 4QR9 and PDB 2GZK, respectively) (Sánchez-Giraldo et al., 2015; Stott et al., 2006) into the cryo-EM density followed by real space refinement (Figure 2.2B and S2.7). We base this interpretation on the ability to see density for phenylalanine in box A but not in box B (Figure S2.7) and the fact that box A bends DNA less than box B (Teo et al., 1995), which would make it more likely to fit the curvature of nucleosomal DNA. As in the structure of SOX11, we also see a modest widening of the minor groove of the nucleosomal DNA at SHL -2 (Figure 2.2C), consistent with the effect of HMG box domains on DNA. Due to HMGB1's high off rate, we could only resolve a single HMG box in our structure, while there could

be up to four HMG boxes if two HMGB1 molecules are bound to a single nucleosome. We hypothesize that there are other regions of nucleosomal DNA where the HMG boxes can transiently interact that are being averaged out in our structure. Thus, there may be an ensemble of rapidly interconverting nucleosome bound conformations of HMGB1.

To visualize other conformations of HMGB1 on nucleosomes that may be present in our dataset, we used the cryoDRGN heterogeneity analysis (Zhong et al., 2021). This analysis revealed various structural classes from our dataset, including ones that correspond to HMGB1 bound at SHL -2 as detected by our earlier analysis (Figure S2.6). Interestingly, in one particular class, there is extra density at SHL -6, which we interpret to be HMGB1 (Figure 2.2D). In this class, we see a modest kink in the nucleosomal DNA, representing the bend induced by the HMG boxes (Figure S2.8). Additionally, in a related reconstruction, we also see this nucleosomal DNA kink at SHL -6 even though HMGB1 density is more poorly resolved (Volume 19, Figure S2.6 and S2.8). The DNA distortions at SHL -6 in these two classes are consistent with our REA results, where we see an increase in DNA accessibility at position 137, which resides between SHL -6 and -7. Together, these structures imply that the two HMG boxes of HMGB1 bind transiently at multiple sites along the nucleosomal DNA. Importantly, these findings are inconsistent with the prevalent model of binding competition between HMGB1 and H1 as none of the observed HMGB1 binding sites overlap with H1's binding site at the dyad. Additionally, in support of our results on core nucleosomes, we see that HMGB1 is able to directly interact with nucleosomal DNA at multiple sites.

When we do observe binding of an HMG box, it correlates with modest local distortion of the nucleosomal DNA. Rapid binding and unbinding of the two HMG boxes and corresponding transient DNA distortion at multiple sites could contribute to HMGB1's overall effect of increasing nucleosomal DNA accessibility. Further if the C-terminus is anchored by the H3 tail, such positioning could synergize with preferential DNA unwrapping at the entry/exit sites, where DNA is less restricted by contacts with the octamer core.

2.3.4 HMGB1 and H1 directly obstruct each other's effects on nucleosomes

Previous biochemical studies have investigated the effects of either HMGB1 alone or H1 alone on nucleosomes, but no studies to date have investigated the biochemical effects of one protein in the presence of the other. Therefore to test how HMGB1 and H1 influence each other's activities, we performed REA experiments in the presence of both proteins on a minimal nucleosome substrate for H1 binding (10/10-Pst137) (White et al., 2016). Consistent with previous REA results using *Drosophila* H1 (Ragab and Travers, 2003), when nucleosomes are bound by H1 there is no detectable cutting (Figure 2.3A), as a closed conformation of the entry/exit DNA is stabilized by H1 (Syed et al., 2010). However, even when HMGB1 is added at concentrations 16-fold over its K_D for nucleosomes, cutting is not recovered (Figure 2.3A and 2.3B). H1's K_D for nucleosomes is in the picomolar-nanomolar range (White et al., 2016), compared to the micromolar K_D for HMGB1 (Figure S2.2C). This large difference in affinities could in principle explain why HMGB1 may not displace H1. However, this explanation does not take into account that the two proteins can interact with each other via their oppositely charged C-terminal tails (Cato et al., 2008). We therefore hypothesized that this direct

interaction enables H1's inhibition of HMGB1 activity. To test this possibility, we investigated the effects of a mutant of H1 (H1-ΔCTE), which lacks the C-terminal basic tail that interacts with HMGB1. This construct still inhibits DNA unwrapping in our REA assay (Figure 2.3A). However, the inhibition of unwrapping is rescued by HMGB1 in a concentration-dependent manner (Figure 2.3A and 2.3B). One interpretation of this result is that direct interaction between the two proteins via their C-terminal tails is essential for H1's inhibition of HMGB1. However deletion of H1's C-terminal tail is known to reduce its affinity for nucleosomes ~100-fold (White et al., 2016). Therefore, an alternative explanation is that due to the lower affinity of the H1-ΔCTE protein, HMGB1 can now compete for binding.

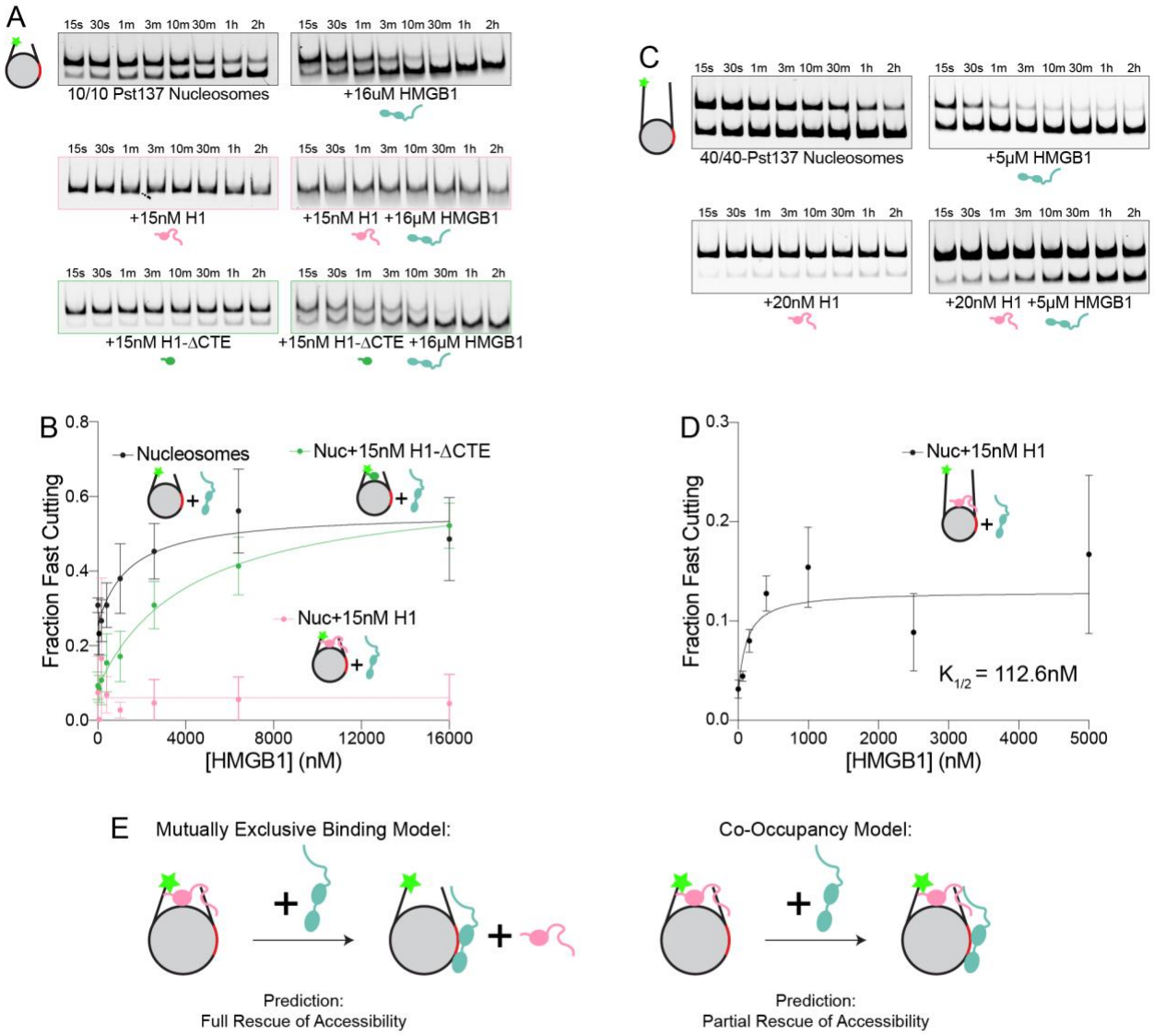

Figure 2.3 HMGB1 and H1 compete to tune nucleosomal DNA accessibility
(A) Representative time-course gels of REA experiments in the presence of indicated concentrations of H1 and/or HMGB1. **(B)** The fraction of fast cutting nucleosomes is shown as a function of HMGB1 concentration. Before HMGB1 is added, nucleosomes are either bound by no H1 (black), 15nM H1 (coral), or 15nM H1-ΔCTE (green). Curve represents a fit by an equation derived from the model in Figure 3E. **(C)** Representative REA time courses of 40/40-Pst137 nucleosomes with or without H1 and/or HMGB1. **(D)** The fraction of fast cutting nucleosomes is shown as a function of HMGB1 concentration. 40/40-Pst137 nucleosomes were pre-incubated with 20nM H1 before HMGB1 was added. Curve represents a fit by an equation derived from the model in Figure 3E. $K_{1/2}$ is 112.6nM, K_D^s is 126.3nM and K_D^f is 21.25nM. **(E)** A schematic of the predictions of the mutually exclusive binding model and the co-occupancy model. The mutually exclusive binding model would predict that titrating HMGB1 would displace H1 from nucleosomes, totally rescuing nucleosomal DNA accessibility. The co-occupancy model would predict that titrating HMGB1 would not displace H1 from nucleosomes and nucleosomal DNA accessibility would only be partially rescued, which is what is observed in (D).

In mammalian chromatin, linker lengths vary from 5bp to over 100 bp (Abdulhay et al., 2020). To investigate the HMGB1 and H1 interplay in the context of linker lengths longer than 10 bp, we used nucleosomes with 40bp of flanking DNA on either side (40/40-

Pst137). Similar to the 10/10 nucleosomes, H1 also inhibits REA on 40/40 nucleosomes (Figure 2.3C). However, unlike 10/10 nucleosomes, on 40/40 nucleosomes, HMGB1 can partially rescue the inhibition of DNA unwrapping caused by H1, indicating that linker DNA length tunes the competition between HMGB1 and H1 (Figure 2.3C). A competition model where binding of H1 and HMGB1 is mutually exclusive predicts that at some saturating concentration of HMGB1, H1 would be fully displaced from the nucleosome (Figure 2.3E). At such a concentration the nucleosomal DNA accessibility should match that observed when HMGB1 is added to nucleosomes in isolation (Figure 2.3E). However, we observe that in the presence of saturating HMGB1, nucleosomal DNA accessibility remains at an intermediate level between H1-inhibited and fully HMGB1-enhanced (Figure 2.3C and 2.3D). This result indicates that HMGB1 counteracts the effects of H1 without displacing H1 from nucleosomes and implies that HMGB1 and H1 can co-occupy a nucleosome. Additionally, the concentration at which DNA unwrapping is 50% rescued ($K_{1/2}$) is 112.6nM (Figure 2.3D), similar to HMGB1's K_D for DNA and 40/40 nucleosomes (Figure S2.2C). This finding suggests that HMGB1 binding to 40/40 nucleosomes is insensitive to the presence of H1, further implying the formation of a ternary complex. Unlike on 10/10 nucleosomes, the flanking DNA on 40/40 nucleosomes is sufficient to accommodate an entire HMGB1 molecule. We therefore propose that 40/40 nucleosomes allow more modes of HMGB1 binding thereby changing how HMGB1 and H1 interact and compete.

2.3.5 HMGB1 stimulates nucleosomal DNA accessibility within chromatin fibers

We next asked whether HMGB1 promotes access to nucleosomal DNA in the context of a chromatin array template. To look at accessibility of DNA within chromatin, we

employed the single-molecule adenine methylated oligonucleosome sequencing assay to test chromatin accessibility on assembled templates (SAMOSA-ChAAT) (Abdulhay et al., 2023). We assembled nucleosomes onto a DNA template containing 12 successive 601 sequences interspersed by 46bp of flanking DNA (Gibson et al., 2019). The pattern of DNA accessibility within the chromatin array showed increased and asymmetric accessibility near the entry/exit sites of the nucleosome (Figure 2.4A and 2.4B), consistent with intrinsic nucleosomal DNA unwrapping and the asymmetry of the 601 sequence (Anderson and Widom, 2000; Ngo et al., 2015). With increasing HMGB1 concentrations, the nucleosomal DNA within the chromatin arrays became more exposed (Figure 2.4A). Furthermore, we see that the increase in DNA accessibility is most pronounced near the entry/exit sites of the nucleosome resulting in a decreased nucleosome footprint size (Figure 2.4B and 2.4C), consistent with the model that HMGB1 enhances existing unwrapping dynamics to expose nucleosomal DNA. The increase in restriction enzyme cutting we observe at position 137 with nucleosomes, is well within the region of increased accessibility we observe by SAMOSA-ChAAT on chromatin arrays, suggesting that HMGB1 acts similarly on nucleosomes within chromatin arrays as it does on mononucleosomes.

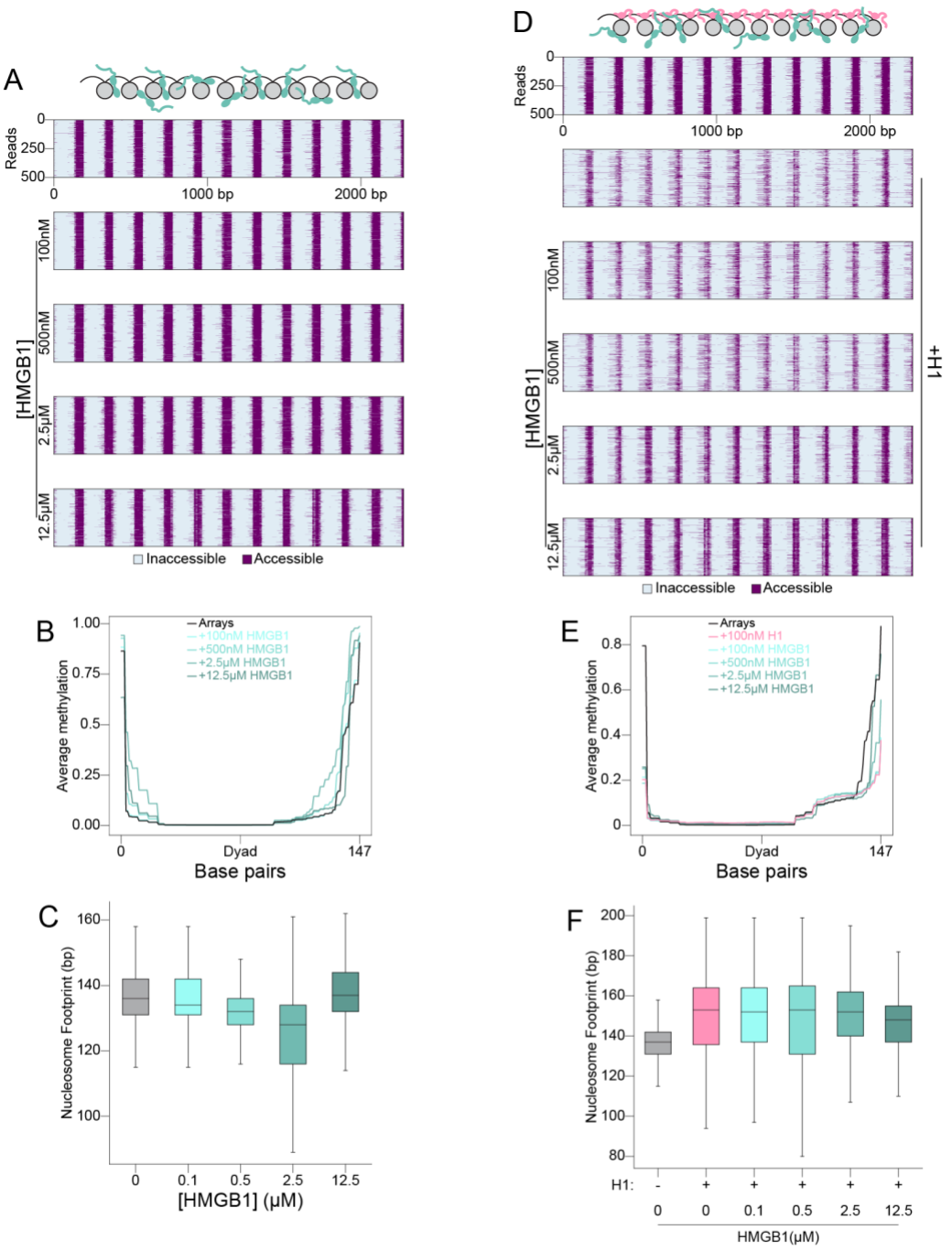

Figure 2.4 HMGB1 increases accessibility of DNA within chromatin
(A) Heat maps of SAMOSA-ChAAT experiments showing nucleosome footprints on a 12x601 array with a range of HMGB1 concentrations. Purple represents DNA that is accessible as assessed by the presence of adenine methylation. Grey represents DNA that is inaccessible as assessed by the lack of methylation and is interpreted as a nucleosome footprint. **(B)** The average methylation across every 601 sequence within the array is combined to show an average nucleosome footprint within the array. **(C)** Box and whiskers plot of nucleosome footprint size is plotted as a function of HMGB1 concentration. Solid line represents the median footprint size, while the height of the box represents the interquartile range, and the error bars represent the farthest data point within 1.5x the interquartile range from the box. **(D)** Heat maps of SAMOSA-ChAAT experiments showing nucleosome footprints on a 12x601 array with H1 and a range of HMGB1 concentrations. Purple and grey represent accessible and inaccessible DNA, respectively as in (A). **(E)** The average methylation across every 601 sequence within the array is combined to show an average nucleosome footprint within the array. **(F)** Box and whiskers plot of nucleosome footprint size is plotted as a function of HMGB1 concentration. Solid line represents the median footprint size, while the height of the box represents the interquartile range, and the error bars represent the farthest data point within 1.5x the interquartile range from the box.

Interestingly, at the highest concentration of HMGB1 tested, we notice a decrease in accessibility and a larger footprint (12.5μM HMGB1, Figure 2.4A, 2.4B and 2.4C). We attribute this effect to bending of the linker DNA caused by binding of additional HMGB1 molecules leading to internucleosome interactions that inhibit access to nucleosomal DNA. This possibility is consistent with previous observations showing that yeast Hmo1 and Nhp6 can promote compaction of chromatin arrays (McCauley et al., 2019).

To explore how HMGB1 and H1 compete to regulate DNA accessibility within chromatin, we performed SAMOSA-ChAAT on chromatin arrays in the presence of both proteins. Consistent with H1's role in forming stable, higher-order structures of chromatin arrays (Robinson et al., 2006; Song et al., 2014), when we add H1 to our arrays, the amount of DNA protection increases (Figure 2.4D). Consistent with REA results on 40/40 nucleosomes, when increasing amounts of HMGB1 are added in the presence of H1, we see a corresponding rescue of DNA accessibility near the entry/exit sites (Figure 2.4D and 2.4E). This is also evidenced by a decrease in the average nucleosome footprint size at higher HMGB1 concentrations (Figure 2.4F). This result indicates that the opposing effects of HMGB1 and H1 observed on mononucleosomes translate to a chromatin substrate.

2.3.6 HMGB1 makes H1 and condensed chromatin more dynamic

Chromatin arrays also provide the opportunity to test the dynamics of HMGB1 and H1 in the context of condensed chromatin, which may more accurately recapitulate *in vivo* chromatin properties. Cellular data on the competition between HMGB1 and H1 comes from fluorescence recovery after photobleaching (FRAP) studies, which showed that

fluorescently labelled H1 recovers faster in the presence of increased concentrations of HMGB1 (Catez et al., 2004). However, it is unclear if this effect is due to direct binding competition between HMGB1 and H1 or an indirect effect. To investigate any direct effects of HMGB1 on H1's binding and turnover dynamics within condensed chromatin, we used well-established previous methods to generate phase-separated chromatin condensates *in vitro* (Gibson et al., 2019). We compacted the chromatin arrays by the addition of 3mM $MgCl_2$ and 100mM KCl in the presence or absence of Alexa555-labeled H1, such that H1 to nucleosome stoichiometry is 1:1, and varied the concentration of HMGB1. HMGB1 causes chromatin condensates containing H1 to become larger, although we see no loss of H1 intensity within condensates (Figure 2.5A and 2.5B). These results suggest that even in condensed chromatin HMGB1 does not simply displace H1 and are consistent with our data suggesting co-occupancy of HMGB1 and H1 on nucleosomes. We next explored whether HMGB1 affects the dynamics of H1 within condensed chromatin as has been reported *in vivo* (Catez et al., 2004).

Consistent with previous results (Gibson et al., 2019), we observe that in the absence of HMGB1, H1 fluorescence recovers to about 45% of pre-bleach intensity within two minutes (Figure 2.5C). Upon addition of HMGB1, we observe an increase in the rate of recovery and the mobile fraction of H1 that recovers, both of which are HMGB1 concentration-dependent (Figure 2.5D and 2.5E). Taken together with the observation that HMGB1 does not decrease the amount of H1 in condensates, we conclude that HMGB1 alters the on/off dynamics of H1's interaction with chromatin, but that binding of HMGB1 and H1 to chromatin is not mutually exclusive.

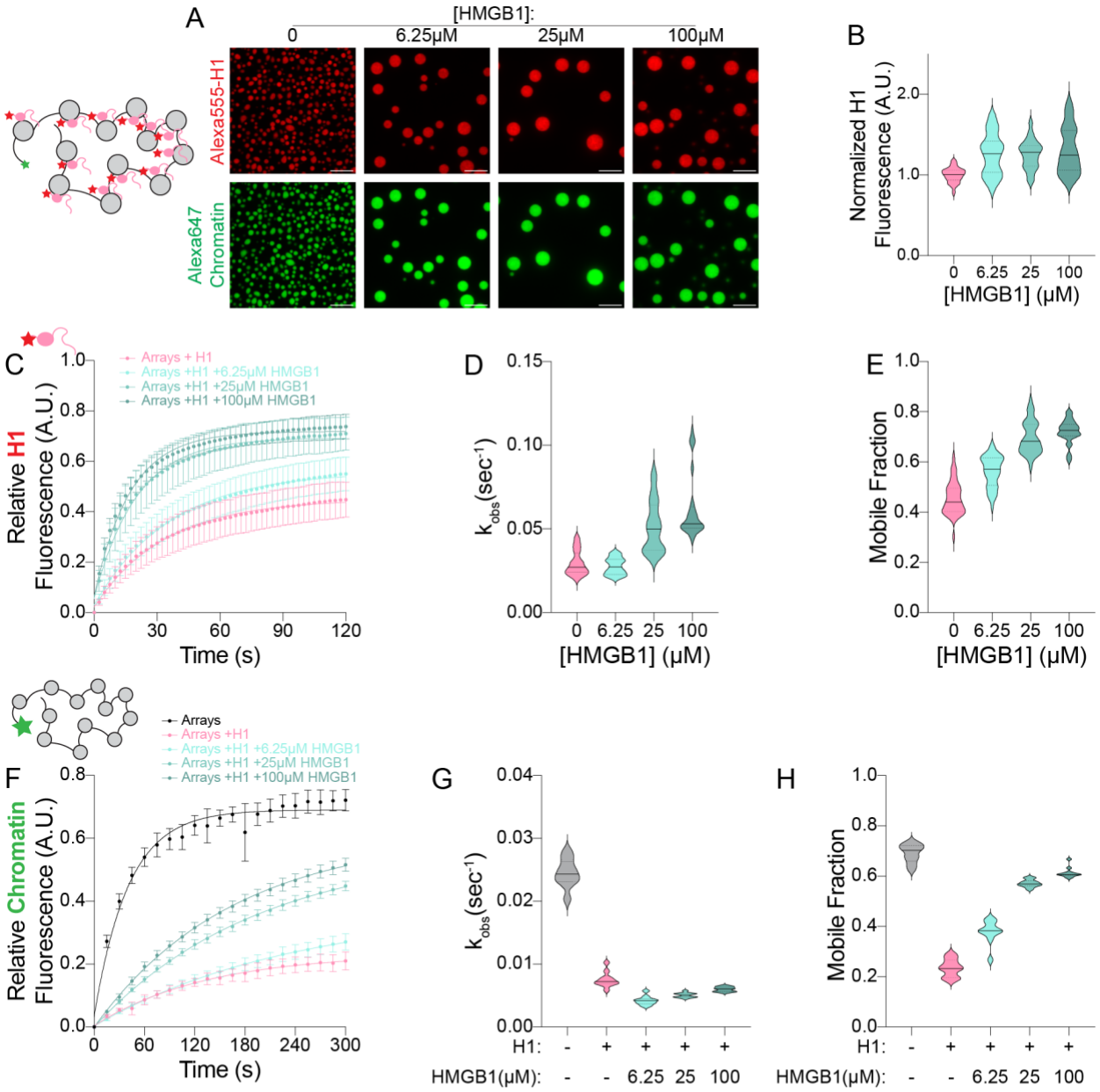

Figure 2.5 HMGB1 increases the turnover dynamics of H1 and chromatin
(A) Representative microscopy images of chromatin condensates. 30nM Alexa647-12x601 arrays are mixed with 360nM Alexa555-H1 and varying concentrations of HMGB1. Scale bar represents 10μm. **(B)** Violin plots of the quantification of the average Alexa555-H1 fluorescence intensity within chromatin condensates. All values are normalized to chromatin and H1 alone with no HMGB1 added. Solid and dotted lines represent the median and interquartile values respectively. Values represent an average of three experimental replicates with n>10 condensates per replicate. **(C)** Quantification of the fluorescence recovery after photobleaching of Alexa555-H1 within chromatin condensates. Values are normalized from 0 to 1 corresponding to post and pre-bleach respectively. Points represent an average of three experimental replicates with n>10 condensates per replicate. Error bars represent standard deviation of all condensates within the three replicates. Data are fit to a one-phase exponentially association. **(D** to **E)** Violin plots of the quantification of the fits to the FRAP data in (C). The rate constant for recovery (kobs) and the plateau of recovery (Mobile Fraction) are plotted for the four different conditions in (D) and (E) respectively. Solid and dotted lines represent the median and interquartile values respectively. **(F)** Quantification of the fluorescence recovery after photobleaching of Alexa647-12x601 arrays within condensates. Values are normalized from 0 to 1 corresponding to post and pre-bleach respectively. Points represent a single experimental replicate with n>10 condensates. Error bars represent standard deviation of all condensates. Data are fit to a one-phase exponentially association. **(G and H)** Violin plots of the quantification of the fits to the FRAP data in (F). The rate constant for recovery (kobs) and the plateau of recovery (Mobile Fraction) are plotted for the five different conditions in (G) and (H) respectively. Solid and dotted lines represent the median and interquartile values respectively.

This finding raises the possibility that while HMGB1 and H1 do not compete by binding the same site within chromatin, their activities on regulating chromatin dynamics are in competition with one another. To investigate this possibility, we performed FRAP on the Alexa647-labeled chromatin arrays within condensates. Consistent with previous FRAP results within chromatin condensates (Gibson et al., 2019), we find that 70% of the chromatin recovers to pre-bleach intensity within five minutes (Figure 2.5F). The addition of H1 slows recovery by ~3-fold and reduces the fraction that recovers to 25%, also consistent with previous results (Gibson et al., 2019) (Figure 2.5F, 2.5G, and 2.5H). Upon addition of increasing amounts of HMGB1, we see a partial rescue of chromatin dynamics (Figure 2.5F). HMGB1 restores the mobile fraction of chromatin to 60% but interestingly does not increase the rate constant of recovery (Figure 2.5G and 2.5H). This result suggests that HMGB1's effect is due to altering H1's activity since in the absence of H1, HMGB1 has minimal effect on chromatin dynamics (Figure S2.9). Together with results showing that H1 is not displaced from the droplets, these findings provide further evidence that HMGB1 and H1 modulate each other's activities by co-occupying chromatin.

2.4 Discussion

Compared to its competitor H1, less is known about HMGB1's interaction with nucleosomes and its effects on chromatin at the mesoscale. Our findings suggest that HMGB1 enhances the dynamics of nucleosomes through rapid sampling and local distortion of multiple locations on nucleosomal DNA by its HMG boxes while its C-terminus is anchored by the H3 tail. Our results also shed light on the competition between HMGB1 and H1. Whereas H1 inhibits dynamics of nucleosomes and

chromatin, HMGB1 appears to act as a molecular stir bar to increase chromatin dynamics at multiple scales. This interplay between these two abundant nuclear architectural proteins presents new opportunities for chromatin regulation. Below we discuss the mechanistic and biological implications of our findings in the context of previous results.

2.4.1 Multiple modes of engagement explain how HMGB1 enhances nucleosomal dynamics

Substantial previous work has led to the model that HMGB1 exposes nucleosomal DNA through its DNA bending activity (Agresti and Bianchi, 2003; Balliano et al., 2017; Bonaldi et al., 2002; Hepp et al., 2014; Joshi et al., 2012; Travers, 2003; Ugrinova et al., 2009). Work with the H3 tail peptide indicates that interactions between the C-terminal tail of HMGB1 and the H3 tail relieve auto-inhibition to allow bending of nucleosomal DNA and facilitate nucleosomal DNA accessibility (Watson et al., 2014). Here we've directly tested these models in the context of a nucleosome. Our results show that the HMG boxes interact with and locally deform nucleosomal DNA. Further, our results suggest an additional role for the interaction between HMGB1's C-terminal tail and the H3 tail. Not only does this interaction sequester the H3 tail away from nucleosomal DNA, allowing DNA to unwrap more readily and relieve autoinhibition of the HMG boxes as proposed previously (Watson et al., 2014), but our results imply that the H3 tail also orients HMGB1 on nucleosomes in a way that promotes unwrapping of nucleosomal DNA (Figure 2.6A). We propose that interaction of the C-terminal tail of HMGB1 with the H3 tail spatially localizes the HMG boxes to certain regions of nucleosomal DNA, such as SHL -2 and SHL -6. Amongst these sites, those where nucleosomal DNA is less

restricted by histone interactions, HMG box-induced DNA bending is more likely to result in unwrapping. Further, we speculate that HMGB1's high off rate and the dynamic interconversion between bound and unbound states allow the nucleosome to rapidly sample multiple states in which different regions of nucleosomal DNA become accessible. Substantial previous work has uncovered how histone chaperones catalyze interconversions between assembled and disassembled nucleosomes and how ATP-dependent chromatin remodelers slide and conformationally alter nucleosomes (Clapier et al., 2017; Winkler and Luger, 2011). The mechanism for HMGB1 provides a third and qualitatively distinct way to make nucleosomal DNA accessible, by promoting a rapid equilibrium between differently bound states, each with a different region of nucleosomal DNA made more accessible.

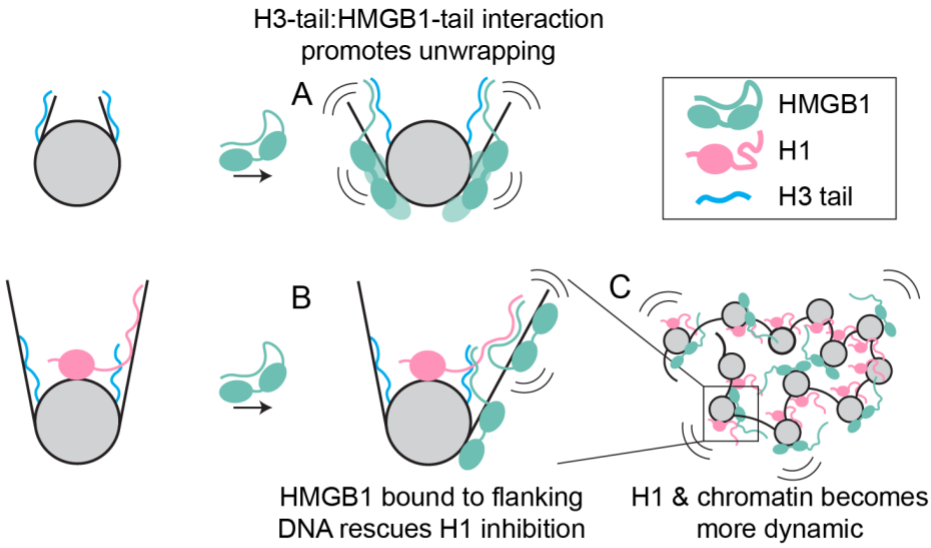

Figure 2.6 HMGB1 and H1 compete to regulate chromatin dynamics across scales
(A) HMGB1 promotes unwrapping through interaction with the H3 tail. This replaces the H3 tail's interaction with nucleosomal DNA and relieves autoinhibition of HMGB1, allowing the HMG boxes to bind and unwrap nucleosomal DNA. **(B)** When longer flanking DNA is present, HMGB1 is able to rescue H1 inhibition of DNA unwrapping. The extra flanking DNA allows additional HMGB1 molecules to interact, which loosens H1's interaction with the flanking DNA, allowing HMGB1 to rescue DNA unwrapping. **(C)** HMGB1's loosening of H1's interaction with flanking DNA makes both H1 and chromatin itself more dynamic within condensed chromatin.

2.4.2 HMGB1 and H1 oppose one another's activities as a function of flanking DNA length

Our data suggest that HMGB1 and H1 counteract each other's activities while co-occupying a nucleosome. Further, the ability of HMGB1 to counteract H1's inhibition of DNA unwrapping increases with increasing flanking DNA length and when the H1 C-terminal tail is deleted. H1 reduces nucleosome dynamics by interacting with and stabilizing the flanking DNA proximal to the entry/exit site (Syed et al., 2010). It is also proposed that interaction between the HMGB1 C-terminal tail and the H1 C-terminal tail relieves autoinhibition of HMGB1 (Cato et al., 2008). We hypothesize that on nucleosomes with short flanking DNA (10 bp or less) HMGB1 can interact with the H1 C-terminal tail, but that this interaction does not sufficiently outcompete the interaction of the H1 tail with nucleosomal DNA. As a result, on nucleosomes with 10 bp of flanking DNA, HMGB1 cannot overcome H1's inhibition of DNA unwrapping. However, when longer flanking DNA is present, the H1 C-terminal tail can now bind flanking DNA in addition to nucleosomal DNA and HMGB1 molecules can be accommodated on the flanking DNA in addition to the core nucleosome (Figure 2.6B). We propose that in this context, the C-terminal tails of HMGB1 and H1 interact resulting in (i) stabilization of HMG box binding to flanking DNA, (ii) displacement of the H1 tail from flanking DNA and (iii) bending of the flanking DNA by the HMG box. Additionally, the bending of flanking DNA by HMGB1 binding could enable additional HMGB1 molecules to more readily distort and bind nucleosomal DNA. Together these coupled outcomes would increase the probability of DNA unwrapping. In this model, the tail-tail interaction between HMGB1 and H1 and the length of flanking DNA tune the two proteins' effects on DNA

accessibility. Overall, we propose that the transient interactions of HMGB1, and the H1 and H3 tails with nucleosomal and flanking DNA creates an ensemble of rapidly interconverting nucleosome bound states. This lowers the energetic barrier of switching between different states in response to changes in linker length or HMGB1 and H1 concentrations to regulate DNA accessibility.

Deletion of H1's C-terminal tail increases H1's turnover *in vivo* and *in vitro* (Gibson et al., 2019; Phair et al., 2004). We find that HMGB1 increases H1's turnover dynamics within condensed chromatin, consistent with the model that the interaction between HMGB1 and H1's C-terminal tail loosens the H1 C-terminal tail's interaction with flanking DNA. This interaction would also have the effect of rescuing H1's inhibition of chromatin dynamics, since the H1 C-terminal tail is necessary for its inhibition of chromatin turnover (Gibson et al., 2019). Overall, by creating more conformational states of chromatin, HMGB1 may function as a molecular stir bar, enhancing the dynamics of nucleosomes and condensed chromatin.

2.4.3 Mechanistic basis for HMGB1's diverse roles in vivo

Overexpression of HMGB1 has been linked to transcription activation (Aizawa et al., 1994), suggesting HMGB1 reduces the inhibitory effect of nucleosomes. Interestingly, a knockout of HMGB1 in mice is associated with a global reduction of nucleosomes, and *in vitro*, HMGB1 enhances the assembly of chromatin (Celona et al., 2011; Lange et al., 2008; Osmanov et al., 2013). Our findings provide a molecular explanation for these results. We observe that HMGB1 drives a transient increase in nucleosomal DNA accessibility and distorts nucleosomal DNA without disassembling the nucleosome. We

therefore propose that HMGB1-induced nucleosomal DNA flexibility allows nucleosomes to dynamically accommodate transient structural changes in DNA, without falling apart. Such accommodation would increase nucleosome stability in the face of factors that try to access nucleosomal DNA. Indeed, the FACT nucleosome chaperone complex, that protects nucleosomes from polymerases, contains an HMG box domain (Winkler and Luger, 2011).

Consistent with the proposed model, HMGB1 has been shown to enhance the affinity of the estrogen receptor to a nucleosomal site and enhance ATP-dependent remodeling by ISWI and SWI/SNF family of chromatin remodelers at the nucleosome scale (Bonaldi et al., 2002; Hepp et al., 2014; Joshi et al., 2012; Patenge et al., 2004; Ugrinova et al., 2009). HMGB1 has also been shown to increase binding of various transcription factors (TF's) to DNA via DNA bending and direct interactions with the TF (Boonyaratanakornkit et al., 1998; Das et al., 2004; Decoville et al., 2000; Jayaraman et al., 1998; Joshi et al., 2011; Oñate et al., 1994; Zappavigna et al., 1996; Zwilling et al., 1995). We therefore speculate that a transient HMGB1-TF complex could act as a bi-partite pioneer factor, enabling access to nucleosomal DNA sequences without disassembly of the histone octamer. Indeed, the SOX family of pioneer factors contains HMG boxes that have evolved sequence specificity, hinting at a possible universal mechanism of HMG box domains for accessing nucleosomal DNA.

Our findings further suggest that the H3 tail-HMGB1 interaction not only releases auto-inhibition by the HMGB1 C-terminal tail, but also orients the HMG boxes for effective

DNA unwrapping. Post-translation modifications of the H3 tail could thus alter how HMGB1 interacts with nucleosomes and its effect on DNA accessibility and serve as a cue to where in the genome HMGB1 acts. One possibility is that HMGB1 cooperates with histone acetyltransferases to induce DNA accessibility. Consistent with this model, HMGB1 localizes to sites in the genome marked by acetylation of Lys27 on H3 (Sofiadis et al., 2021).

2.4.4 Consequences of competition between HMGB1 and H1 in vivo

In vivo, HMGB1 and H1 have been shown to compete with one another, despite HMGB1's lower concentration and weaker affinity to chromatin (Bonaldi et al., 2002; Catez et al., 2004; Duguet and de Recondo, 1978; Thomas and Stott, 2012; Ueda et al., 2004; White et al., 2016). Our model reconciles this paradox by providing a molecular mechanism whereby HMGB1 counteracts H1 activity without displacing it from chromatin. In this model, HMGB1 concentrations do not need to be high enough to competitively displace H1 from a nucleosome. HMGB1 concentrations only have to be high enough to co-occupy nucleosomes in a manner that allows the C-terminal tail of HMGB1 to interact with the H1 tail. This model explains why in stem cells, where HMGB1 expression is highest, H1 turnover is increased compared to differentiated cells which have less HMGB1 (Meshorer et al., 2006; Müller et al., 2004), suggesting that HMGB1 may be especially important for pluripotency. HMGB1 expression is also elevated in some cancers, which could present an opportunity for therapeutic intervention (Müller et al., 2004).

Along with expression levels, phosphorylation of the H1 C-terminal tail could modulate the competition between HMGB1 and H1. Indeed in metaphase, when H1 phosphorylation is higher, HMGB1 is displaced from chromosomes while H1 remains bound (Contreras et al., 2003; Falciola et al., 1997). H1 phosphorylation has also been linked to both activation and repression of transcription (Bhattacharjee et al., 2001; Dou et al., 1999; Dou and Gorovsky, 2000), suggesting that there could exist a variety of modes of regulation of this competition via H1 phosphorylation. Further exploration of the role of H1 tail phosphorylation will reveal how competition with HMGB1 is modulated *in vivo*.

Recent attempts to determine nucleosome structures *in situ* have found that the majority of nucleosomes do not have stable flanking DNA conformations, and many nucleosomes appear partially unwrapped (Arimura et al., 2021; Cai et al., 2018c, 2018b, 2018a; Tan et al., 2023). We propose that the competition between HMGB1 and H1 is responsible for creating some of these more heterogeneous nucleosome structures, yet HMGB1, due to its high off rate and multiple modes of binding cannot be captured structurally, unlike H1. Additional heterogeneity may also arise from variations in linker lengths as we find that flanking DNA length is an important factor that tunes the competition between HMGB1 and H1, with H1 effects predominating at shorter linker lengths and HMGB1 effects at longer lengths. Linker DNA lengths *in vivo* vary from 5bp to over 100bp (Abdulhay et al., 2020) and thus likely regulate where in the genome HMGB1 or H1 affect nucleosomal DNA accessibility.

This study emphasizes the essential role of architectural proteins in modulating global effects on chromatin dynamics. Despite what the name suggests, we find that the abundant architectural protein HMBG1 does not serve as a structural support for chromatin, but rather our data suggests that HMBG1 increases the dynamics and accessibility of chromatin to enable DNA access without nucleosome disassembly. Further we propose that the interplay between HMGB1 and architectural proteins like H1 that act more canonically to inhibit chromatin dynamics increases the number of states of the system allowing chromatin dynamics to be finely tuned at the molecular and mesoscale.

2.5 Materials and Methods

Preparation of DNA substrates

DNA used for mononucleosomes was generated using large scale PCR of a plasmid containing the Widom 601 sequence. Various primers, labeled with either Alexa Fluor 488 or Cy5 (IDT), were used to generate different lengths of flanking DNA around the 601 sequence. When noted in the text, the 601 sequence contained a restriction enzyme site for PstI at position 137. PCR products were run over an 8% acrylamide gel and the band was cut out based on the DNA shadow. The gel band was crushed by passage through a 5-mL syringe and soaked in 1x TE overnight before the crushed gel was removed with a 0.22-μm filter. The DNA was further ethanol precipitated and resuspended in 1x TE.

DNA for chromatin arrays was generated from a plasmid containing 12 successive 601 sequences, interspersed by 46 bp’s of linker DNA (Gibson et al., 2019). The plasmid

was grown in STBL2 cells (Thermo Fisher) and giga prepped (QIAGEN). The plasmid was then digested with EcoRV to cut out the array sequence and digest the plasmid backbone. To make Alexa Fluor 647-labeled arrays for condensate experiments, the DNA was additionally digested with XhoI to leave a sticky end on one end of the DNA. The array DNA was then purified over a Sephacryl S-1000 column and fractions containing the array DNA were pooled and isopropanol precipitated, before being resuspended in 1x TE. We note that two successive runs over the S-1000 column were necessary to fully remove the plasmid backbone.

To generate labeled array DNA, the sticky end generated by XhoI digest was filled in using Klenow polymerase (Invitrogen) with an Alexa Fluor 647-labeled dCTP (Invitrogen) along with unlabeled dATP, dTTP, and dGTP according to manufacturer's instructions. DNA was then purified by phenol:chloroform extraction and ethanol precipitation before resuspension in 1x TE.

Assembly of nucleosomes and chromatin arrays

Recombinant *Xenopus laevis* histones H3, H4, H2A, and H2B were expressed and purified from *E. coli* as previously described (Luger et al., 1999). Histone octamer and dimer was then reconstituted as previously described (Luger et al., 1999). Mononucleosome and chromatin arrays were assembled via salt gradient dialysis as previously described (Luger et al., 1999). Mononucleosomes were further purified over a glycerol gradient. All samples were quantified using a NanoDrop to measure the concentration of DNA within the sample.

HMGB1 purification

A codon-optimized cDNA of *Homo sapiens* HMGB1 was generated by Twist Biosciences and cloned into a pBH4 plasmid backbone. Briefly the construct contains an N-terminal 6xHis tag followed by a TEV protease cleavage site, which when cleaved leaves a single Gly-Ser linker before the start Met of HMGB1. The plasmid is transformed into Rosetta (DE3) competent cells (Sigma Aldrich) and grown in 2xYT (20g tryptone, 10g NaCl, 10g yeast extract per 1L) supplemented with 50µg/mL carbenicillin and 25µg/mL chloramphenicol at 37ºC. Once cells have reached log phase (OD = 0.5-0.6), expression was induced with 1mM IPTG at 37ºC for 4 hours. Cells were then pelleted by spinning at 5000 x g for 30min at 4ºC and pellets were stored at -80ºC.

Pellets were resuspended in Lysis Buffer with 2x protease inhibitor (20mM HEPES-KOH pH 7.5, 500mM KCl, 10% Glycerol, 7.5mM Imidazole, 2mM BME, 2mM PMSF, 2µg/mL Pepstatin A, 6µg/mL Leupeptin, and 4µg/mL Aprotinin). The cell suspension was homogenized by passage through a Dounce homogenizer. Cells were lysed with an Emulsiflex at 15,000 psi for 15 minutes. Lysate was then clarified by centrifugation at 40,000 x g for 30min at 4ºC. Lysate was then incubated with TALON affinity resin (Takara, 1mL bead volume/1L bacterial culture) for 1hour at 4ºC while nutating. Beads were then washed in batch two times with two bead volumes of Lysis Buffer with 1x protease inhibitor (20mM HEPES-KOH pH 7.5, 500mM KCl, 10% Glycerol, 7.5mM Imidazole, 2mM BME, 1mM PMSF, 1µg/mL Pepstatin A, 3µg/mL Leupeptin, and 2µg/mL Aprotinin) to remove any remaining lysate. Beads were then added to plastic disposable

gravity columns and washed with 20 bead volumes of Lysis Buffer (20mM HEPES-KOH pH 7.5, 500mM KCl, 10% Glycerol, 7.5mM Imidazole, 2mM BME). His-tagged HMGB1 was then eluted with 5 bead volumes of Elution Buffer (20mM HEPES-KOH pH 7.5, 150mM KCl, 400mM Imidazole, 2mM BME) (Figure S2.10A). Cleavage of the His tag was then induced with TEV protease (150µg TEV/1L bacterial culture) and left to dialyze overnight in TEV dialysis buffer (20mM HEPES-KOH, 150mM KCl, 2mM DTT) (Figure S2.10B).

TEV-cleaved, full-length HMGB1 was then added to a Mono-Q anion exchange column equilibrated with 10% Buffer QB (Buffer QA: 20mM HEPES-KOH pH 7.5, 3mM DTT Buffer QB: 20mM HEPES-KOH pH 7.5, 1.5M KCl, 3mM DTT). HMGB1 was eluted from the Mono-Q column with a linear gradient from 10 to 60% Buffer QB (150mM to 900mM KCl) over 20 column volumes. Full length HMGB1 comes off between 32-35% Buffer QB (~500mM KCl), while many products that do not contain the full C-terminal domain come off at lower [KCl], therefore this anion exchange step is crucial to obtaining pure, full-length HMGB1 (Figure S2.10C and S2.10D). These fractions are then pooled and concentrated in a 3000 Da molecular weight cut off spin filter device. HMGB1 is finally purified over a Superdex 75 Increase size exclusion column equilibrated in Size Exclusion buffer (20mM HEPES-KOH pH 7.5, 300mM KCl, 10% Glycerol, 3mM DTT) (Figure S2.10E and S2.10F). Fractions containing HMGB1 are pooled and concentrated in a 3000 Da molecular weight cut off spin filter device, before being aliquoted, flash-frozen, and stored at -80ºC in Size Exclusion buffer.

HMGB1-ΔC is purified identically, except a HiTrap SP cation exchange column is used in place of the Mono-Q anion exchange column, as the pI of HMGB1-ΔC is basic, while HMGB1-WT is acidic. A 10 to 60% gradient of Buffer QB (150mM to 900mM KCl) is still used, and HMGB1-ΔC elutes between 29-33% Buffer QB (~465mM KCl). We do not see any contaminating expression products, because the C-terminal domain has been removed.

H1 purification

Homo sapiens H1.4 purification was adapted from (Gibson et al., 2019) using a construct containing an N-terminal MBP, followed by a TEV cleavage site, followed by H1.4 (full length or ΔCTE), followed by an additional TEV cleavage site, and a C-terminal 6xHis tag. This construct was transformed into Rosetta pLysS competent cells (EMD Millipore) and grown in 2xYT (20g tryptone, 10g NaCl, 10g yeast extract per 1L) supplemented with 50µg/mL carbenicillin and 25µg/mL chloramphenicol at 37ºC. Once cells have just reached log phase (OD = 0.4), cultures are moved to 18ºC for 1 hour. After 1 hour, expression is induced with 0.5mM IPTG for 18 hours at 18ºC. Cultures are then pelleted at 5000 x g for 30min at 4ºC and pellets are stored at -80ºC.

Pellets are resuspended in Lysis Buffer with 2x protease inhibitor (20mM HEPES-KOH pH 7.5, 1M NaCl, 10% Glycerol, 7.5mM Imidazole, 2mM BME, 2mM PMSF, 2µg/mL Pepstatin A, 6µg/mL Leupeptin, and 4µg/mL Aprotinin) The cell suspension was homogenized by passage through a Dounce homogenizer. Cells were lysed with an Emulsiflex at 15,000 psi for 15 minutes. Lysate was then clarified by centrifugation at

40,000 x g for 30min at 4ºC. Lysate was then incubated with TALON affinity resin (Takara, 1.5mL bead volume/1L bacterial culture) for 1hour at 4ºC while nutating. Beads were then washed in batch two times with two bead volumes of Lysis Buffer with 1x protease inhibitor (20mM HEPES-KOH pH 7.5, 1M NaCl, 10% Glycerol, 7.5mM Imidazole, 2mM BME, 1mM PMSF, 1µg/mL Pepstatin A, 3µg/mL Leupeptin, and 2µg/mL Aprotinin) to remove any remaining lysate. Beads were then added to plastic disposable gravity columns and washed with 20 bead volumes of Lysis Buffer with 1x protease inhibitor (20mM HEPES-KOH pH 7.5, 1M NaCl, 10% Glycerol, 7.5mM Imidazole, 2mM BME, 1mM PMSF, 1µg/mL Pepstatin A, 3µg/mL Leupeptin, and 2µg/mL Aprotinin). Tagged H1 was then eluted with 5 bead volumes of Elution Buffer (20mM HEPES-KOH pH 7.5, 150mM NaCl, 10% Glycerol, 350mM Imidazole, 2mM BME, 1mM PMSF, 1µg/mL Pepstatin A, 3µg/mL Leupeptin, and 2µg/mL Aprotinin). Eluted protein was then incubated with amylose affinity resin (NEB, 2mL bead volume/1L bacterial culture) for 1hour at 4ºC while nutating. The beads are then added to plastic disposable gravity columns and washed with 20 bead volumes of Amylose Wash Buffer (20mM HEPES-KOH pH 7.5, 150mM NaCl, 10% Glycerol, 2mM BME, 1mM PMSF, 1µg/mL Pepstatin A, 3µg/mL Leupeptin, and 2µg/mL Aprotinin). H1 is then eluted with 5 bead volumes of Amylose Elution Buffer (20mM HEPES-KOH pH 7.5, 150mM NaCl, 10% Glycerol, 2mM BME, and 1% Maltose). Cleavage of the MBP and His tags was then induced with TEV protease (225µg TEV/1L bacterial culture) and left to dialyze overnight in TEV dialysis buffer (20mM HEPES-KOH, 150mM KCl, 2mM DTT).

H1 is then loaded onto a HiTrap SP cation exchange column equilibrated with TEV dialysis buffer. H1 is then eluted with a linear gradient from 10 to 60% Buffer SB (Buffer SA: 20mM HEPES-KOH pH 7.5, 2mM BME Buffer SB: 20mM HEPES-KOH pH 7.5, 1.5M NaCl, 2mM BME) over 20 column volumes. Fractions containing H1 were then incubated with 2mL bead volume of TALON affinity resin (Takara) for 1 hour at 4ºC nutating, to remove contaminating His-tagged TEV protease. The beads were removed using a plastic gravity column and the flow through is concentrated using a 3000 Da molecular weight cut off spin filter device. H1 was then purified over a Superdex 75 Increase size exclusion column equilibrated in Size Exclusion buffer (20mM HEPES-KOH pH 7.5, 150mM NaCl, 10% Glycerol, 1mM DTT). Fractions containing H1 were pooled and concentrated in a 3000 Da molecular weight cut off spin filter device, before being aliquoted, flash-frozen, and stored at -80ºC in Size Exclusion buffer.

For purification of fluorescently labeled H1, a Lys-Cys-Lys was added N-terminal to the start Met of H1. The protein was purified identically to H1-WT, however, before size exclusion chromatography, H1 was dialyzed overnight into Labeling Buffer (20mM HEPES-KOH pH 7.5, 150mM NaCl, 1mM TCEP). Protein was then labeled with 3-fold molar excess of Alexa Fluor 555 maleimide (Invitrogen) at room temperature for 15 minutes. The labeling was quenched with 10-fold excess DTT. The protein was then concentrated using a 3000 Da molecular weight cut off spin filter device, and the unincorporated dye was removed by purification over a Superdex 75 Increase size exclusion column equilibrated in Size Exclusion buffer (20mM HEPES-KOH pH 7.5, 150mM NaCl, 10% Glycerol, 1mM DTT). Fractions containing H1 were pooled and

concentrated in a 3000 Da molecular weight cut off spin filter device, before being aliquoted, flash-frozen, and stored at -80ºC in Size Exclusion buffer.

Restriction enzyme accessibility (REA) assays

For all restriction enzyme accessibility assays, 10nM of fluorescently labeled nucleosomes containing a PstI site at position 137 within the nucleosomal DNA are used. Purified HMGB1 or H1 is added to nucleosomes in the presence of a 10x buffer that supplements to a final buffer of: 19mM HEPES-KOH pH7.5, 1mM Tris-HCl pH7.4, 30mM KCl, 45mM NaCl, 5mM $MgCl_2$, 2mM DTT, 9% Glycerol, 0.11mM EDTA, 20µg/mL BSA, 0.015% Triton-X100, and 0.02% NP-40. Nucleosomes are allowed to equilibrate with HMGB1 or H1 for 30 minutes at 37ºC. When both proteins are present, H1 is allowed to equilibrate first for 30 minutes, before adding HMGB1 and waiting another 30 minutes to start the reaction. The time course is started upon addition of PstI (NEB, 100U/uL) to a final concentration of 10U/uL. At each time point, 5µL of the reaction is removed and added to a 2x REA Stop Mix (20mM Tris-HCl pH8, 70mM EDTA, 2% SDS, and 20% Glycerol). After the time course, 2uL of Proteinase K (NEB, 800U/mL) is added to each time point and allowed to incubate for 30 minutes at 55ºC. For reactions in which >5µM of HMGB1 was added, an additional 2uL of 800U/mL Proteinase K was added after 15 minutes. After incubation, each time point is loaded onto a 8% acrylamide (29:1 acrylamide:bis) 1x TBE gel and run at 150V for at least 2 hours. Gels are imaged using a Typhoon laser-scanning gel imager (GE). The fraction of DNA that is uncut is measured using ImageJ and plotted as a function of time. All nucleosome REA experiments are fit to a two-step exponential decay function in GraphPad Prism:

$$SpanFast = (Y0 - Plateau) * PercentFast * .01$$

$$SpanSlow = (Y0 - Plateau) * (100 - PercentFast) * .01$$

$$Y = Plateau + SpanFast*exp(-KFast*X) + SpanSlow*exp(-KSlow*X)$$

The fraction of nucleosomes that is cut fast is calculated using the following equation, which also factors in the fraction of nucleosomes that are not cut (Plateau):

$$Fraction\ Fast = ((1 - Plateau) * PercentFast) / 100$$

All REA experiments on DNA are fit to a one-step exponential decay function in GraphPad Prism:

$$Y = (Y0 - Plateau)*exp(-K*X) + Plateau$$

Two-phase REA fitting and modeling

A model for how HMGB1 interacts with both fast and slow-cutting nucleosome populations is shown in Figure 3E. The fraction fast calculated above is plotted as a function of HMGB1 concentration and fit to the following equations derived based on this thermodynamic cycle to calculate the K_D for the fraction that is cut fast and slow (K_D^f and K_D^s respectively) and the overall half maximal concentration of HMGB1 ($K_{1/2}$):

$$Y = (K_D^f + X) / ((X/B_{max}) + (K_D^f/B_{min}))$$

$$K_D^s = (K_D^f*(B_{max} / (1 - B_{max}))) / (B_{min} / (1 - B_{min}))$$

$$(1/K_{1/2}) = B_{min}/K_D^f + (1 - B_{min})/K_D^s$$

B_{min} and B_{max} represent the fraction of fast cutting nucleosomes when fully unbound (B_{min}) and fully bound (B_{max}).

Electrophoretic mobility shift assays (EMSA)

Fluorescently labeled nucleosomes (10nM) were incubated with various concentrations of HMGB1 in the presence of a 10x buffer that supplements the final buffer composition to be: 20mM HEPES-KOH pH7.5, 75mM KCl, 10% Glycerol, 1mM EDTA, 2mM DTT, and 0.02% NP-40. Binding was allowed to equilibrate at room temperature for 30 minutes before loading onto a 6% acrylamide (29:1 acrylamide:bis) 0.5x TBE gel. The gel was run for 2.5 hours at 125V and imaged using a Typhoon laser scanning gel imager (GE). The fraction of nucleosomes that are bound is calculated by measuring the unbound nucleosomes band and subtracting that value from the intensity of the whole lane. The fraction bound is then plotted as a function of HMGB1 concentration and fit to the following binding equation with the Hill coefficient N:

$$Y = ((X\text{^}N*B_{max}) + (K_D\text{^}N*B_{min}))/(X\text{^}N + K_D\text{^}N)$$

Cryo-EM sample preparation and data collection

HMGB1 and 0/10 nucleosomes were dialyzed into EM buffer (20 mM HEPES-KOH pH 7.5, 25 mM KCl, 1 mM EDTA, 2 mM DTT, 1.5% glycerol) overnight. Due to the relatively low affinity (micromolar range), HMGB1 was mixed with nucleosomes at final concentrations of 12 μM HMGB1 and 1 μM nucleosome and allowed to incubate at 20°C for 30 minutes prior to plunge freezing on Quantifoil R 1.2/1.3 200 mesh Au grids. Grids were cleaned beforehand for 15s using a PELCO easiGLOW glow discharge system.

Sample grids were plunge frozen using a FEI Mark IV Vitrobot set at 4°C and 100% humidity. 3 μL of sample was applied to each grid. Each grid was blotted with humidity-

saturated Whatman 1 filter papers for 3s with a blot force of -1 before being plunge frozen into liquid ethane.

Sample grids were first screened using a 200 kV FEI Talos Arctica at UCSF. A larger dataset was then collected on two grids on a 300 kV Titan Krios at UCSF using a K3 camera at a nominal magnification of 105kx (0.834 Å/pix). All data was collected using Serial EM v3.7 or newer.

Cryo-EM data processing

Raw movies were motion-corrected using UCSF MotionCor2 v1.4.1 (Zheng et al., 2017). Dose-weighted micrographs were imported into cryoSPARC v4.1.1 (Punjani et al., 2017) and patch CTF estimation (multi) was used to estimate defocus values. Micrographs were filtered using Curate Exposures based on average defocus, estimated CTF, and relative ice thickness. A nucleosome map was used to generate templates for particle picking using Template Picker. A total of ~8.5 million particles were extracted at 288 pix box downsampled to 72 pix. To remove junk particles, extracted particles were filtered through three rounds of Heterogeneous Refinement, where in each round a good nucleosome map and 3 junk maps (generated using Ab Initio on a small subset of remaining particles) were used as templates. After classification, the remaining good particles were re-extracted at 288 pix box downsampled to 192 pix and duplicate picks were removed using Remove Duplicates, resulting in 561,888 particles.

The 561,888 particles were then used in Ab Initio to generate 3 classes, and the output volumes were used as templates for Heterogeneous Refinement to further classify the remaining particles. One good class containing 339,268 particles was further refined first using Homogenous Refinement and then Non-Uniform Refinement, optimizing for per-particle defocus and per-group CTF parameters. The resulting map showed a hint of density for an HMG box at SHL -2.

To further classify the particles for nucleosomes that contain an HMG box, the particles were exported using UCSF pyem v0.5 (Asarnow et al., 2019) to RELION v4.0 (Scheres, 2012). 3D classification without alignment was performed using a spherical mask centered on the SHL -2 region. One class out of 4 showed density for the HMG box domain, and the 47,813 particles in this class were imported back into cryoSPARC v4.1.1 and re-extracted at 288 pix box. One round of 2D classification was performed to remove remaining obvious junk, resulting in 42,115 particles. This final set of particles was refined using Non-Uniform Refinement, resulting in the final map at ~3 Å global resolution for an HMGB1 box domain bound to nucleosome at SHL -2.

cryoDRGN analysis

The 339,268 particles that showed a hint of density for an HMG box at SHL -2 were re-extracted at 300 pix downsampled to 240 pix. The particles were exported using UCSF pyem v0.5 to generate a .star file, and a corresponding .mrcs particle stack was generated using RELION. Inputs were preprocessed using cryoDRGN v1.1.2 (Zhong et al., 2021) to generate pose and CTF .pkl files compatible with cryoDRGN. Images were

downsampled further from 240 pix to 120 pix and used to train a cryoDRGN model with an 8-dimensional latent variable over 50 epochs of training. cryoDRGN analysis was then performed using the resulting model to visualize the latent space and generate density maps using default settings.

Model building

The ~3 Å global resolution output volume from cryoSPARC Non-Uniform Refinement was used to build a model for the HMGB1 box domain bound to nucleosome at SHL -2. The nucleosome from PDB 8V4Y (Chio et al., 2024) was used as the initial template for the nucleosome, and an HMGB1 Box A domain from PDB 4QR9 (Sánchez-Giraldo et al., 2015) was used as the initial template for the HMG box domain. DNA, histones, and the HMG box were adjusted using COOT v0.9.6 to account for differences in base pairs and residues that are resolved or not resolved in the current map. The ISOLDE plug-in (Croll, 2018) for UCSF ChimeraX v1.7.1 was used to correct for Ramachandran and rotamer outliers. COOT v0.9.6 was then used to correct bond angle and bond length outliers. The quality of all refined models was assessed using model validation in Phenix v1.18.2 and the wwPDB validation server.

Single-molecule adenine methylated oligonucleosome sequencing assay to test chromatin accessibility on assembled templates (SAMOSA-ChAAT)

Unlabeled chromatin arrays (1ng/μL) were incubated with varying concentrations of HMGB1 and H1 (50nM when present) in the presence of 1x CutSmart Buffer (NEB), 2mM DTT and 1mM S-Adenosyl methionine in 100μL. Binding was allowed to

equilibrate for 30 minutes at 37ºC. In the cases when HMGB1 and H1 were present, H1 was allowed to bind first for 30 minutes before addition of HMGB1 and an additional 30 minutes to equilibrate. To induce DNA methylation, 1µL of EcoGII (NEB) was added to a final concentration of 50U/mL. Methylation proceeded for 30 minutes at 37ºC before adding 10µL of 10% SDS 2.5µL ProK (NEB, 800U/mL). Proteinase K digestion proceeded for 2 hours at 65ºC. Methylated DNA was purified from these reactions via 1X SPRI Select Beads.

PacBio Library Preparation and Sequencing

Entire binding reactions were used as input for PacBio SMRTbell library preparation. SMRTbell preparation of libraries was done using the SMRTbell prep kit 3.0 and included DNA damage repair, end repair, SMRTbell ligation, and exonuclease cleanup according to the manufacturer's instruction. After exonuclease cleanup and purification via 1x v/v SMRTbell cleanup beads, DNA concentration was measured by Qubit High Sensitivity DNA Assay (1 µl each sample). Data was collected over 30-hour Sequel II movie runs with 2 hours pre-extension time and 2.1 polymerase.

SMRT Data Processing

Sequencing reads were processed as homogenous samples as described in (Abdulhay et al., 2023) with slight variations.

Chromatin Sample Processing

Raw sequencing reads from chromatin samples were processed using software from Pacific Biosciences:

1. Generate circular consensus sequences (CCS)

   CCS were generated for each sequencing cell using ccs 6.9.99. The --hifi-kinetics flag was used to generate kinetics information (interpulse duration, or IPD) for each base of each consensus read. Values were stored for each base as 50*(mean logIPD) + 1.

2. Demultiplex consensus reads

   Consensus reads were demultiplexed using lima. The flag '–same' was passed as libraries were generated with the same barcode on both ends. This produces a BAM file for the consensus reads of each sample.

3. Align consensus reads to the reference genome

   pbmm2, the pacbio wrapper for minimap2 (Li, 2018), was run on each CCS BAM file (the output of step 2) to align reads to the reference sequence, producing a BAM file of aligned consensus reads.

Extracting interpulse duration measurements

The IPD values were accessed from the aligned, demultiplexed consensus BAM files.

Model Training

Neural network, SMM, and SVD models were trained on fully methylated and unmethylated controls similarly to (Abdulhay et al., 2023) but using IPD values from the aligned, demultiplexed consensus BAM files.

The Hidden Markov model was structured similarly to (Abdulhay et al., 2023) but was refactored from pomegranate to use cython and numba.

Processed data analysis

All processed data analyses and associated scripts are available at GitHub. All analyses were computed using python. Plots were constructed via Matplotlib. Each analysis is briefly described below:

Defining inaccessible regions and counting nucleosomes

Inaccessible regions were called from HMM output data identically to (Abdulhay et al., 2020). Briefly, inaccessible regions were defined as continuous stretches with accessibility ≤0.5. Periodic peaks were observed that approximated sizes of regions containing one, two, three, or more nucleosomes. Cutoffs for each size were manually defined using the histogram of inaccessible region lengths from a control sample.

Fluorescence recovery after photobleaching (FRAP) of chromatin condensates

Purified HMGB1 and H1 were dialyzed overnight in Protein Dialysis Buffer (20mM HEPES-KOH pH7.5, 200mM KCl, 7mM $MgCl_2$, and 2mM BME). Arrays were diluted to

60nM in buffer from the chromatin array assembly (20mM HEPES-KOH pH7.5, 1mM EDTA, and 2mM BME). For each reaction, 10μL of arrays, 2μL H1 (or buffer), and 8μL HMGB1 (or buffer) were added to a microcentrifuge tube so that the final buffer is 20mM HEPES-KOH pH7.5, 100mM KCl, 3.5mM $MgCl_2$, 0.5mM EDTA, and 2mM BME. After 30 minutes at room temperature, reactions were transferred to a 384-well glass bottom plate (Cellvis), which had been mPEGylated and passivated with BSA according to (Gibson et al., 2019). Condensates were allowed to settle in the well for at least 1 hour before imaging with a Plan Apo VC 100x/1.4NA (Nikon) oil immersion objective on a Nikon Ti2 microscope equipped with a CREST-V2 LFOV Spinning Disk (Crest Optics), Celesta Light Engine (Lumencor), with excitation wave lengths 546nm or 647nm and emission filters FF01-595/31 or FF02-685/40 (Semrock) to Image Alexa Fluor 555 or 647 respectively, a 405/488/561/640/750 Dichroic (Crest), a Prime 95B 25mm sCMOS camera, run using NIS Elements 5.41.01 build 1709 (Nikon). Fluorescence recovery after photobleaching was achieved with a Opti-Microscan FRAP unit with a 405nm Reflect/430-800nm Trans Dual TIRF (FRAP) dichroic and 405nm laser for photobleaching. 20% laser power was used to bleach Alexa Fluor 555-labeled H1 and 15% laser power was used to bleach Alexa Fluor 647-labeled chromatin arrays. Average H1 intensity within the bleached area was measured at 2.5 second intervals for 2 minutes. Average chromatin intensity within the bleached area was measured at 10 second intervals for 5 or 10 minutes. The signal was background subtracted and corrected for photobleaching by measuring the average intensity in an identical area of a condensate in the same field of view that had not been bleached using the following formula:

$$CorrectedInt = (BleachInt – BackgroundInt) / (ControlInt – BackgroundInt)$$

The fluorescence recovery was normalized to both the pre-bleach intensity and post-bleach intensity using the following formula:

$$NormalizedInt = (CorrectedInt – PostBleachInt) / (PreBleachInt – PostBleachInt)$$

The data were then fit to the following one-phase exponential association function in GraphPad Prism to determine the rate and mobile fraction of recovery:

$$Y = Y0 + (MobileFraction - Y0) * (1-exp(-K*x))$$

2.6 Supplemental Figures and Tables

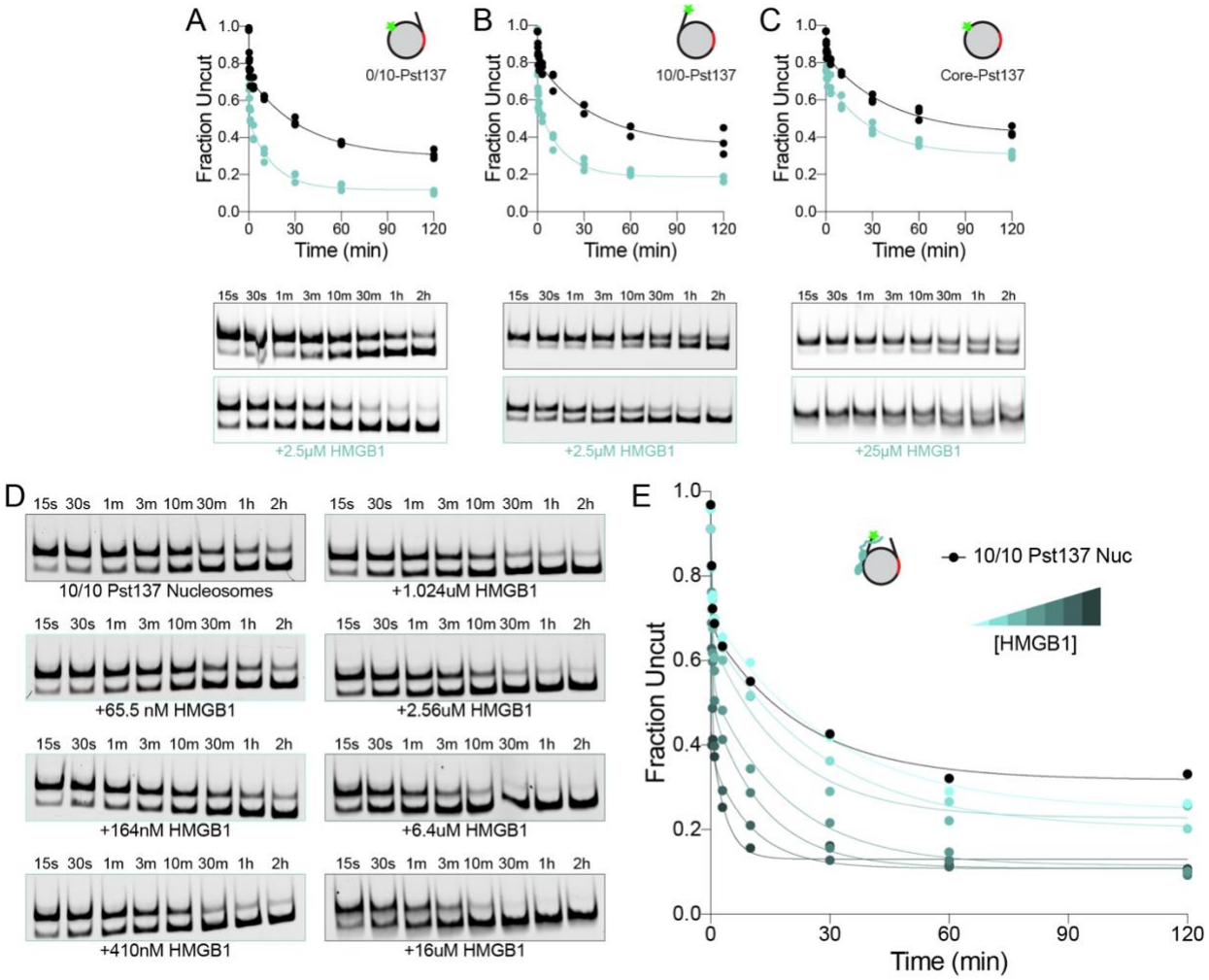

Figure S2.1 Flanking DNA is dispensable for HMGB1's effect on REA
(A, B and C) Top panels show quantification of three replicate REA experiments on 0/10-Pst137 (A), 10/0-Pst137 (B) and Core-Pst137 (C) with (teal) and without (black) HMGB1. The fraction of DNA that remains uncut is plotted as a function of time. The data for all three replicates are fit by a two-step exponential decay function. Bottom panels show representative gels of time courses of REA on nucleosomes with (bottom) and without (top) the presence of 2.5μM HMGB1 or 25μM HMGB1 for Core Pst137. **(D)** Representative time-course gels of REA experiments on 10/10-Pst137 nucleosomes as a function of varying HMGB1 concentrations (65.5nM, 164nM, 410nM, 1.024μM, 2.56μM, 6.4μM, and 16μM). **(E)** Quantification of REA experiments in (D). Each time course is fit by a two-step exponential decay. These experiments were performed in triplicate and used to make the data seen in Figure 1E and 1F.

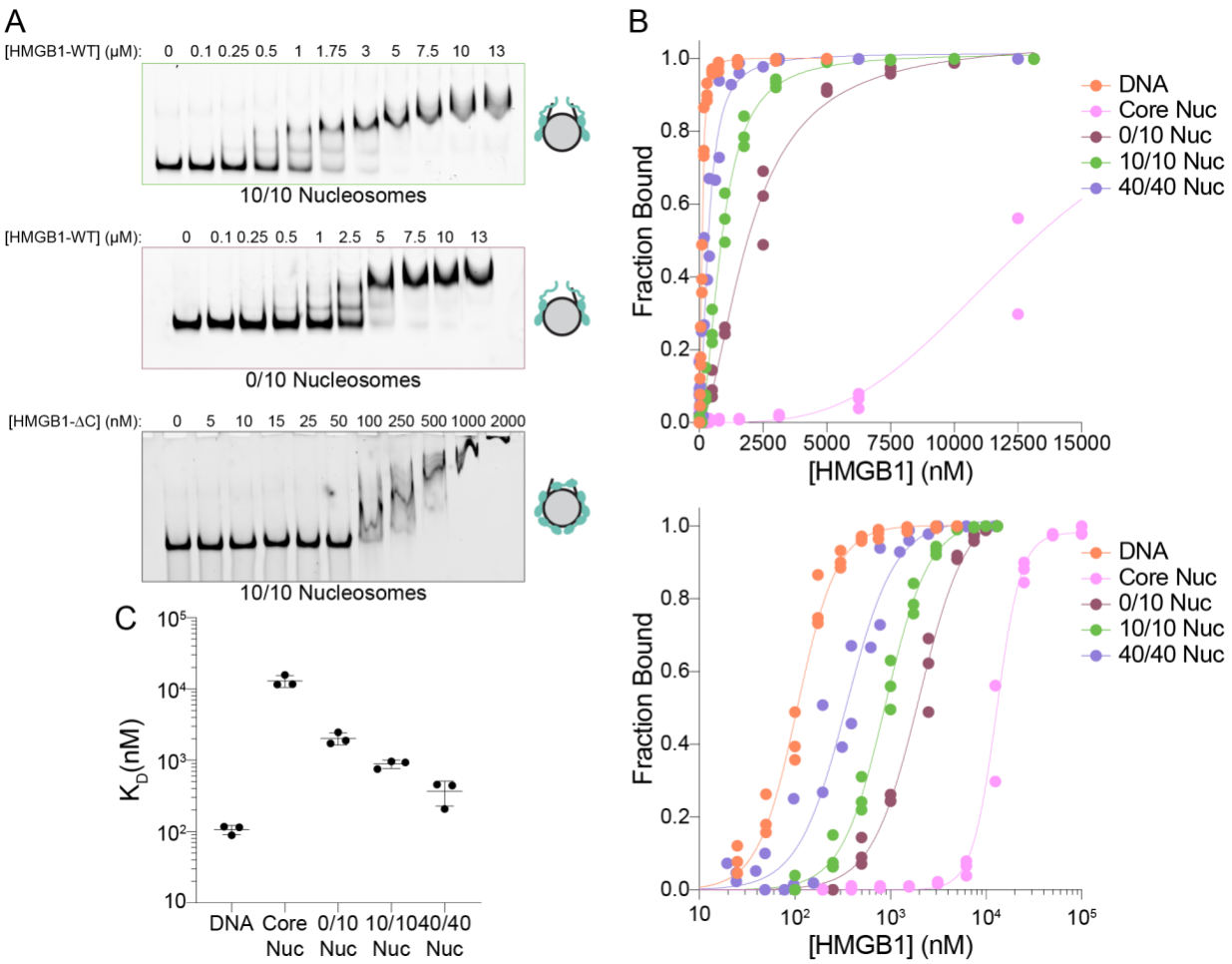

Figure S2.2 HMGB1 binding to nucleosomes and DNA

(A) Representative images of gels depicting electrophoretic mobility shift assays (EMSA) showing binding HMGB1-WT (top 2 gels) and HMGB1-ΔC to labeled 10/10 nucleosomes (top and bottom gels) or labeled 0/10 nucleosomes (middle gel). **(B)** Quantification of binding of HMGB1-WT measured by EMSA assays as shown in (A). HMGB1-WT binding to DNA (orange), core nucleosomes (pink), 0/10 nucleosomes (burgundy), 10/10 nucleosomes (green) and 40/40 nucleosomes (purple) are shown. Each condition was performed in triplicate and fit to a binding equation. Bottom panel shows the same quantification on a semi-log plot. **(C)** Quantification of the K_D values of HMGB1-WT binding to various DNA and nucleosome substrates. K_D values are extracted from binding curve fits in (B).

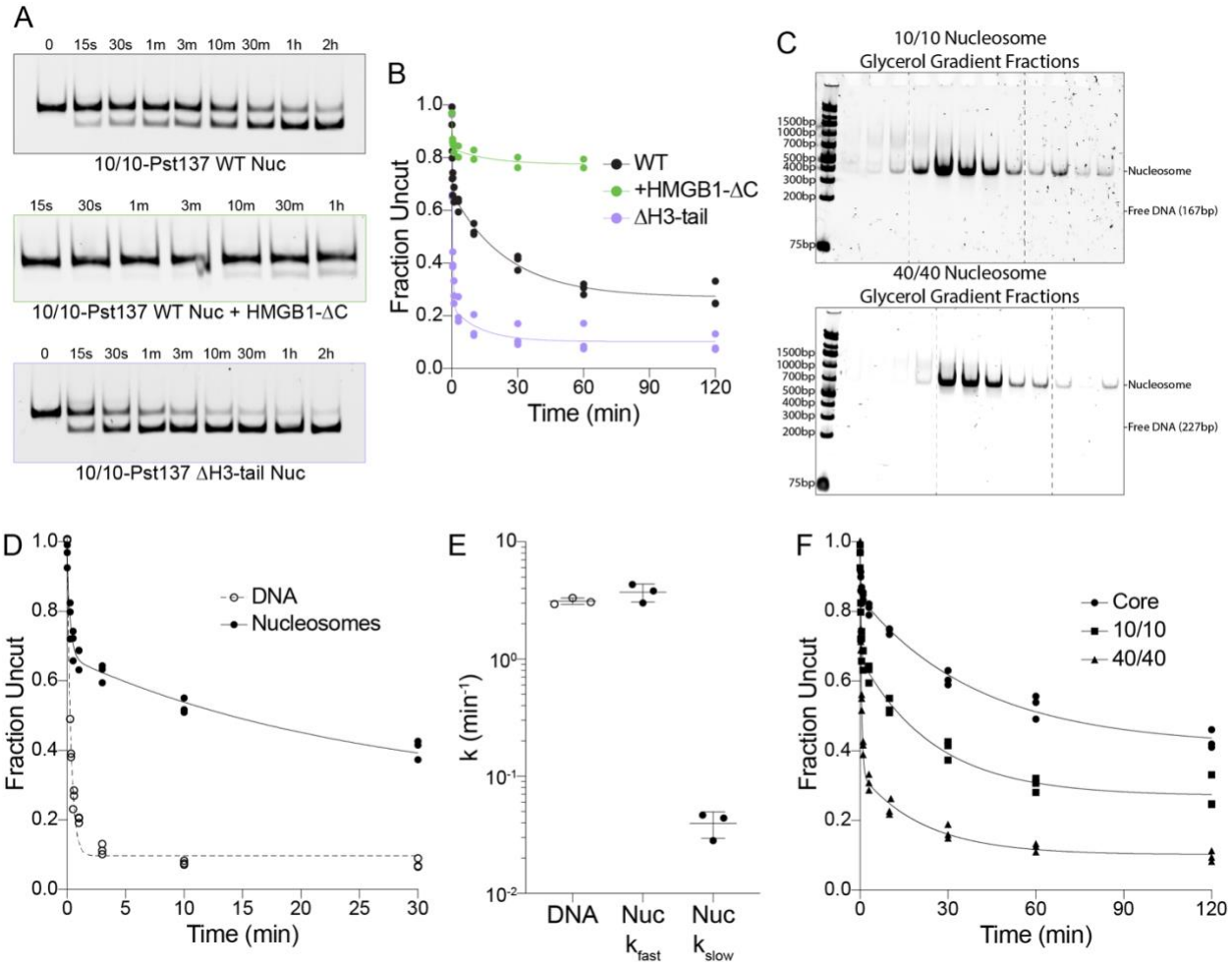

Figure S2.3 Additional REA experiments

(A) Representative gels of REA experiments on 10/10-Pst137 WT (black) or ΔH3-tail (magenta) nucleosomes. Bottom gel is of WT nucleosomes in the presence of 100nM HMGB1-ΔC (green). **(B)** Quantification of REA experiments from (A). Nucleosome alone experiments are shown in triplicate, and nucleosomes with 100nM HMGB1-ΔC in duplicate. The data are fit to a two-step exponential decay function. **(C)** Representative gels of glycerol gradient fractions showing the purification of assembled 10/10 (top) and 40/40 (bottom) nucleosomes, showing the lack of free DNA. Dashed lines represent the fractions that were pooled. **(D)** Quantification of REA experiments on 10/10-Pst137 WT nucleosomes (closed circles) and DNA (open circles). Nucleosome REA is fit to a two-step exponential decay function (solid line), while DNA REA is fit to a one-step exponential decay function (dashed line). **(E)** Quantification of the rate constants derived from the curves in (C). Error bars represent the standard deviation of three experimental replicates. **(F)** Quantification of REA experiments on Pst137 nucleosomes with either no flanking DNA (Core, circles), 10bp of flanking DNA on either side of the nucleosome (10/10, squares), or 40bp of flanking DNA on either side of the nucleosome (40/40, triangles). Each condition is fit to a two-step exponential decay function.

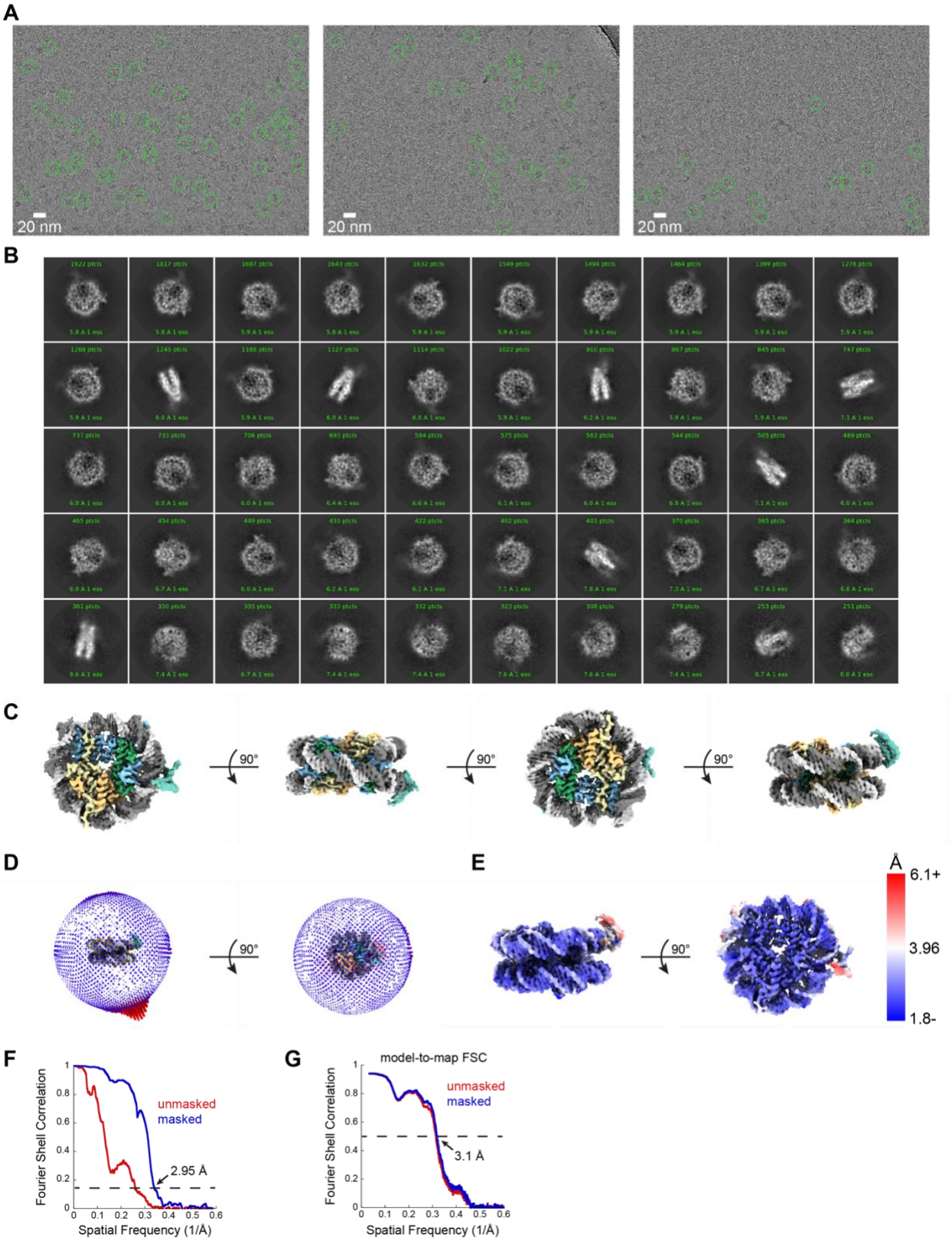

Figure S2.4 Single-particle cryo-EM of HMGB1 with 0/10 nucleosomes

(A) Representative motion-corrected micrographs from the HMGB1 with 0/10 nucleosome dataset. **(B)** Representative 2D classes of HMGB1 bound to 0/10

nucleosome. **(C)** Four different views of the cryo-EM map of HMGB1 bound to 0/10 nucleosome at SHL -2 generated with non-uniform refinement in cryoSPARC v4.1.1. The structure is color-coded with histone H3 in light blue, histone H4 in green, histone H2A in yellow, histone H2B in orange, DNA strands in light/dark gray, and HMGB1 in teal. **(D)** Angular distribution of particles used to generate the cryo-EM map of HMGB1 bound to 0/10 nucleosome at SHL -2 with non-uniform refinement in cryoSPARC v4.1.1. **(E)** Cryo-EM map of HMGB1 bound to 0/10 nucleosome at SHL -2 generated with non-uniform refinement in cryoSPARC v4.1.1 colored by estimated local resolution determined with FSC = 0.143 cutoff in cryoSPARC v4.1.1. **(F)** Unmasked (red) and masked (blue) Fourier shell correlation curves between two half-maps for the HMGB1 bound to 0/10 nucleosome at SHL -2 non-uniform refinement determined by cryoSPARC v4.1.1. **(G)** Unmasked (red) and masked (blue) model-to-map Fourier shell correlation curves between the model and map for HMGB1 bound to 0/10 nucleosome at SHL -2 determined by Phenix v1.19.

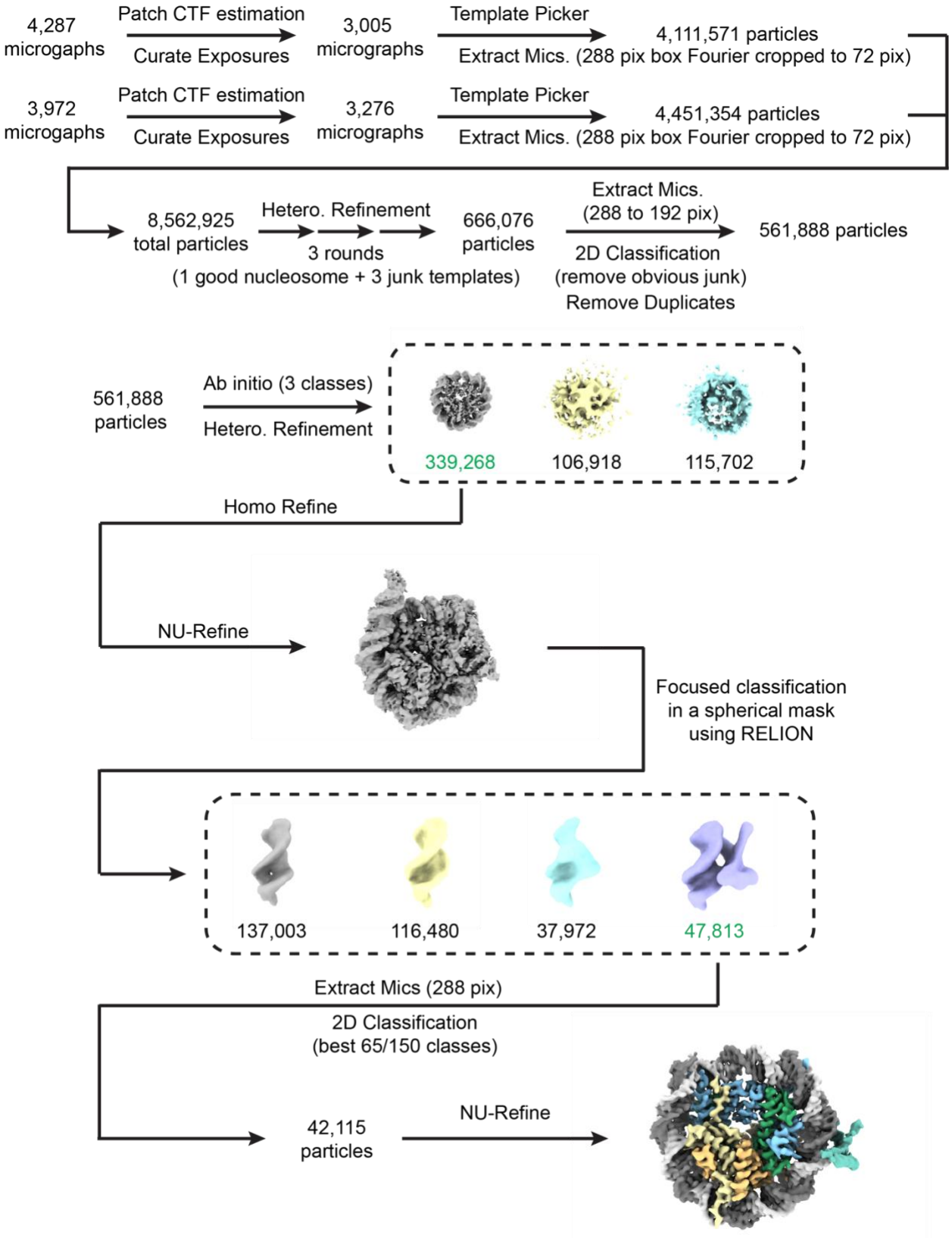

Figure S2.5 Data processing for HMGB1 with 0/10 nucleosome

Flowchart for cryo-EM data processing of the HMGB1 with 0/10 nucleosome dataset as described in Methods. Most processing steps were performed in cryoSPARC v4.1.1 with the numbers of micrographs and particles moving into each step noted. Focused classification without alignment was performed in RELION v4.0 to improve HMGB1 density. Final non-uniform refinement was performed with cryoSPARC v4.1.1.

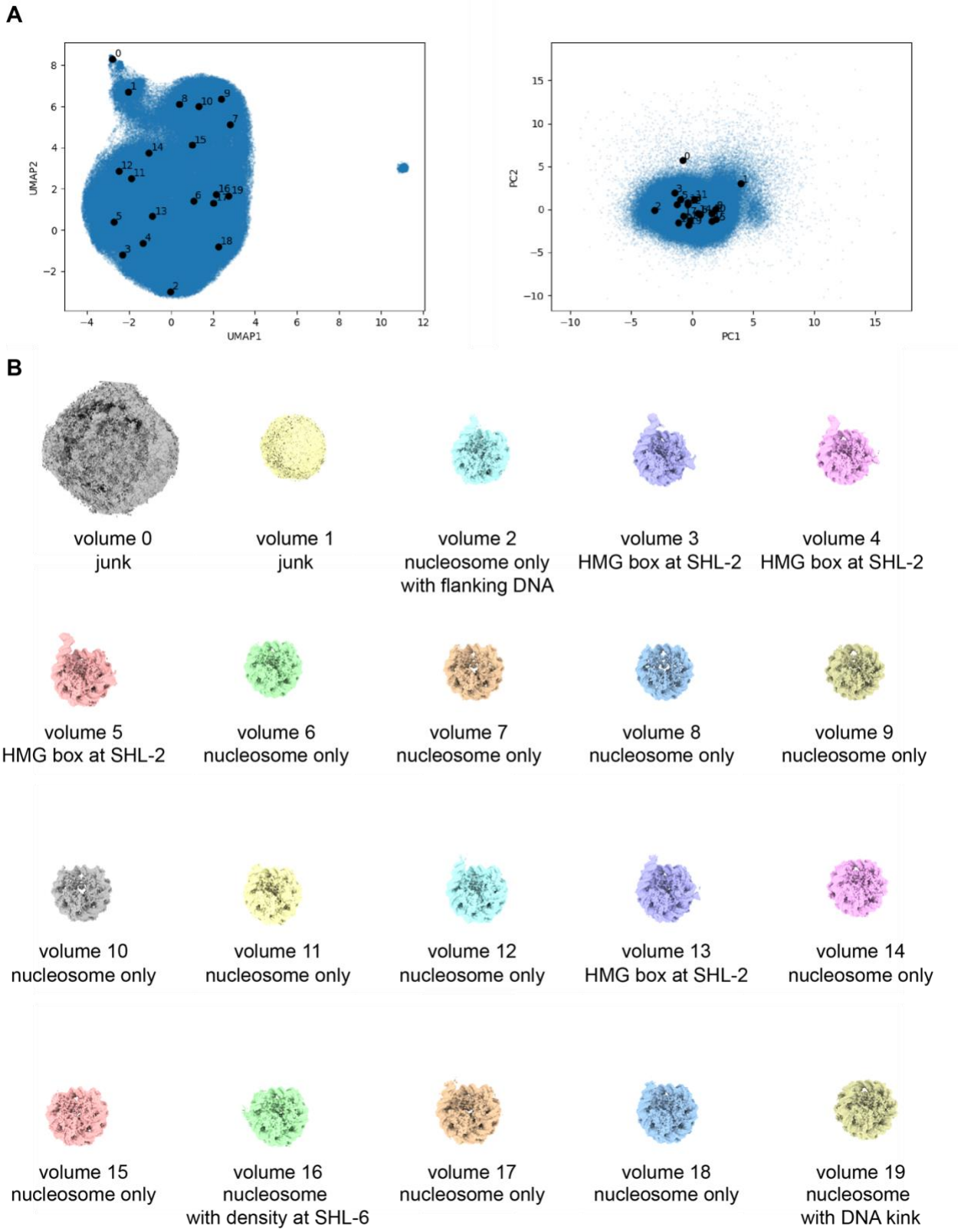

Figure S2.6 cryoDRGN analysis for HMGB1 with 0/10 nucleosome
(A) The resulting UMAP and PCA visualizations of the particle latent embeddings after training an 8-dimensional latent variable model using cryoDRGN v1.1.2. The centers of

20 different clusters determined by the k-means clustering algorithm to partition the latent space are annotated with a dot and corresponding cluster number. **(B)** The resulting 20 density maps generated from particles partitioned by the k-means clustering algorithm. Brief descriptions of each density map are provided, with most maps corresponding to either a nucleosome-only class, nucleosome with HMGB1 bound at SHL -2, and nucleosome with kinked DNA at SHL -6 with some hint of extra density for HMGB1.

Figure S2.7 Analysis of HMGB1 density at SHL -2

(A) The relatively low local resolution of the HMGB1 density at SHL -2 (~4 to 6 Å) precluded de novo model building in this region. Previously determined structures of HMGB1 box A bound to DNA (PDB 4QR9) and HMGB1 box B bound to DNA (PDB 2GZK) were docked into the current EM density as potential initial templates. The observed HMG box fold in our current structure more closely matches the previously determined structure of HMGB1 box A (left) and does not match the determined structure of HMGB1 box B (right). **(B)** Real space refined models of HMGB1 box A (left) and HMGB1 box B (right) in the observed HMG box density at SHL -2. For simplicity, only sidechains for phenylalanine and tryptophan residues are shown in pink. Density can be observed for these bulky residues if the sequence for box A is built into the density (left) but not if the sequence for box B is built (right).

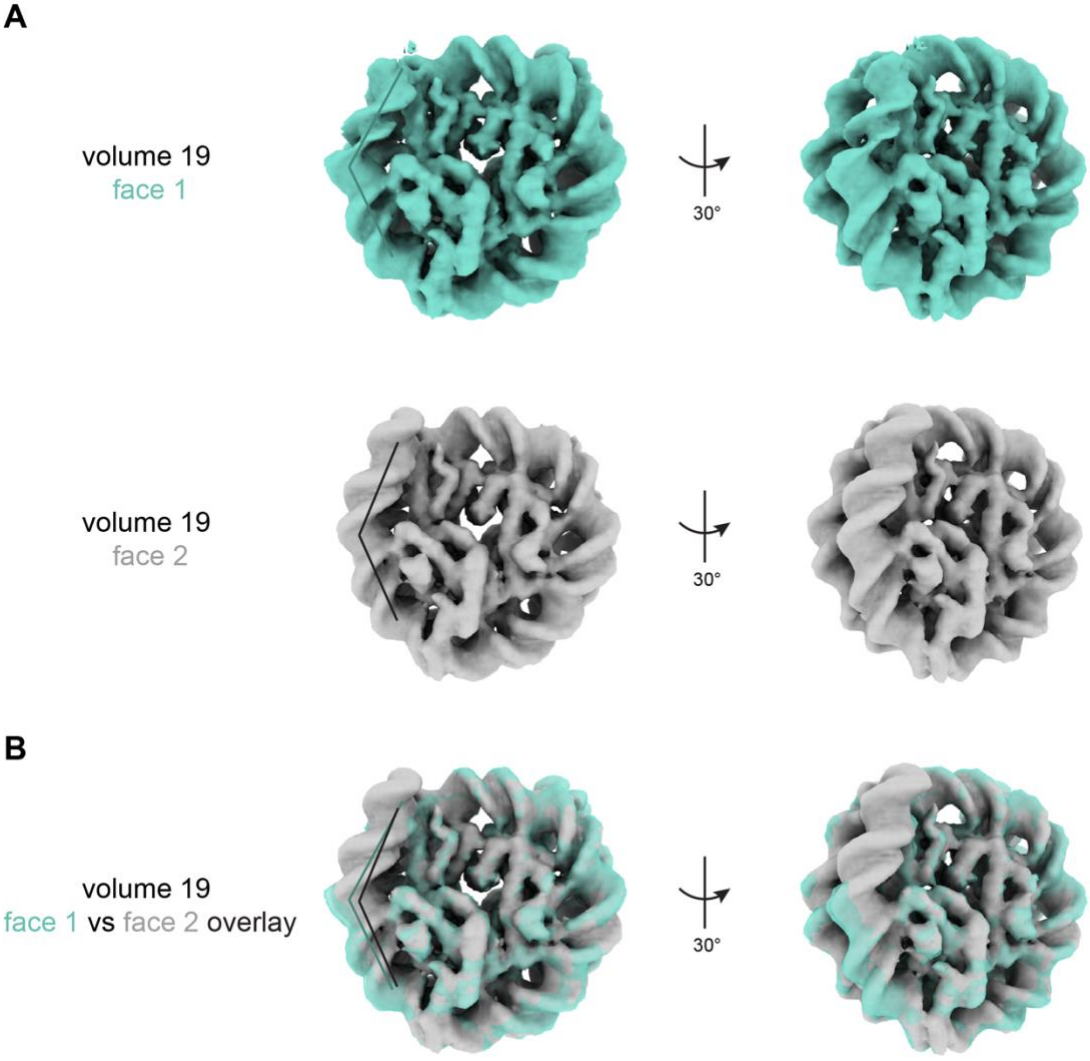

Figure S2.8 Analysis of DNA kink at SHL -6 in volume 19
(A) Density maps of both faces of the nucleosome from volume 19 from the cryoDRGN analysis. **(B)** An overlay of the density maps of both faces of the nucleosome. Face 1 (teal) shows the kink in the DNA at SHL -6.

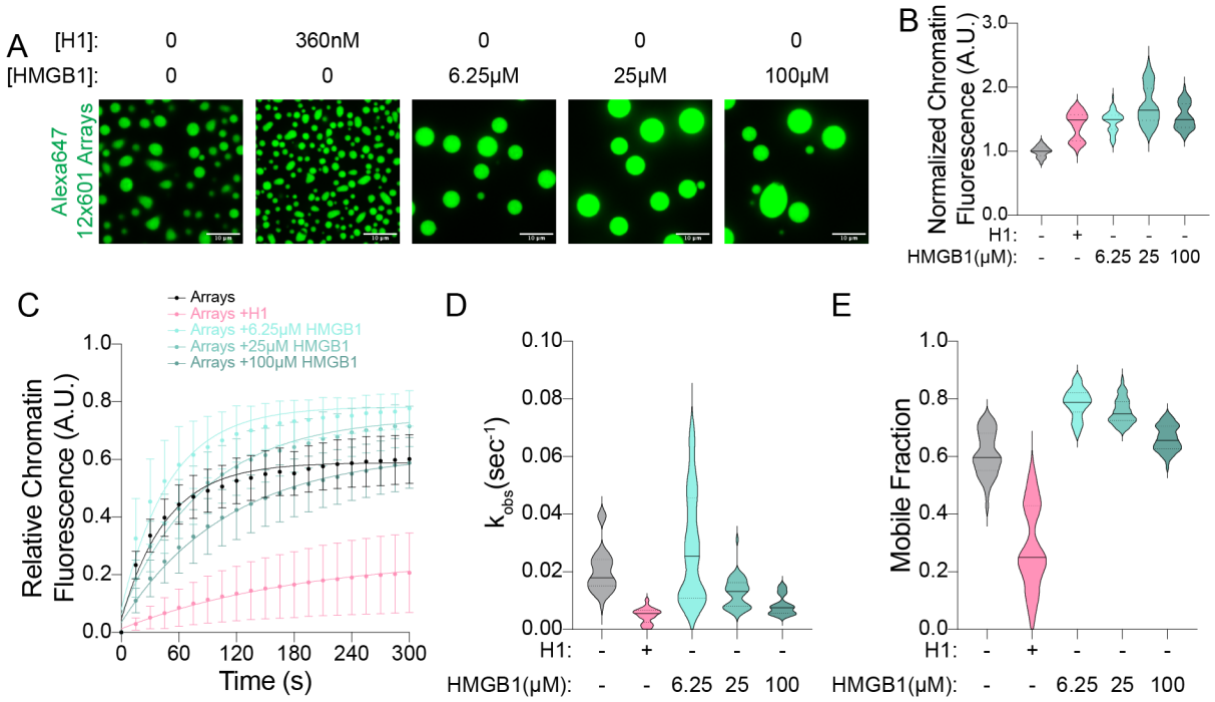

Figure S2.9 HMGB1 has minimal effect on chromatin turnover
(A) Representative images of chromatin condensates consisting of 30nM Alexa647 12x601 chromatin arrays and various concentrations of H1 or HMGB1 as indicated. Scale bars represent 10μm. **(B)** Violin plots of the quantification of the average Alexa647 12x601 chromatin arrays fluorescence intensity within chromatin condensates. All values are normalized to chromatin alone. Solid and dotted lines represent the median and interquartile values respectively. Values represent an average of three experimental replicates with n>10 condensates per replicate. **(C)** Quantification of the fluorescence recovery after photobleaching of Alexa647 12x601 chromatin arrays within condensates. Values are normalized from 0 to 1 corresponding to post and pre-bleach respectively. Points represent an average of three experimental replicates with n>10 condensates per replicate. Error bars represent standard deviation of these same replicates. Data are fit to a one-phase exponentially association. **(D and E)** Violin plots of the quantification of the fits to the FRAP data in (C). The rate constant for recovery (k_{obs}) and the plateau of recovery (Mobile Fraction) are plotted for the four different conditions in (D) and (E) respectively. Solid and dotted lines represent the median and interquartile values respectively.

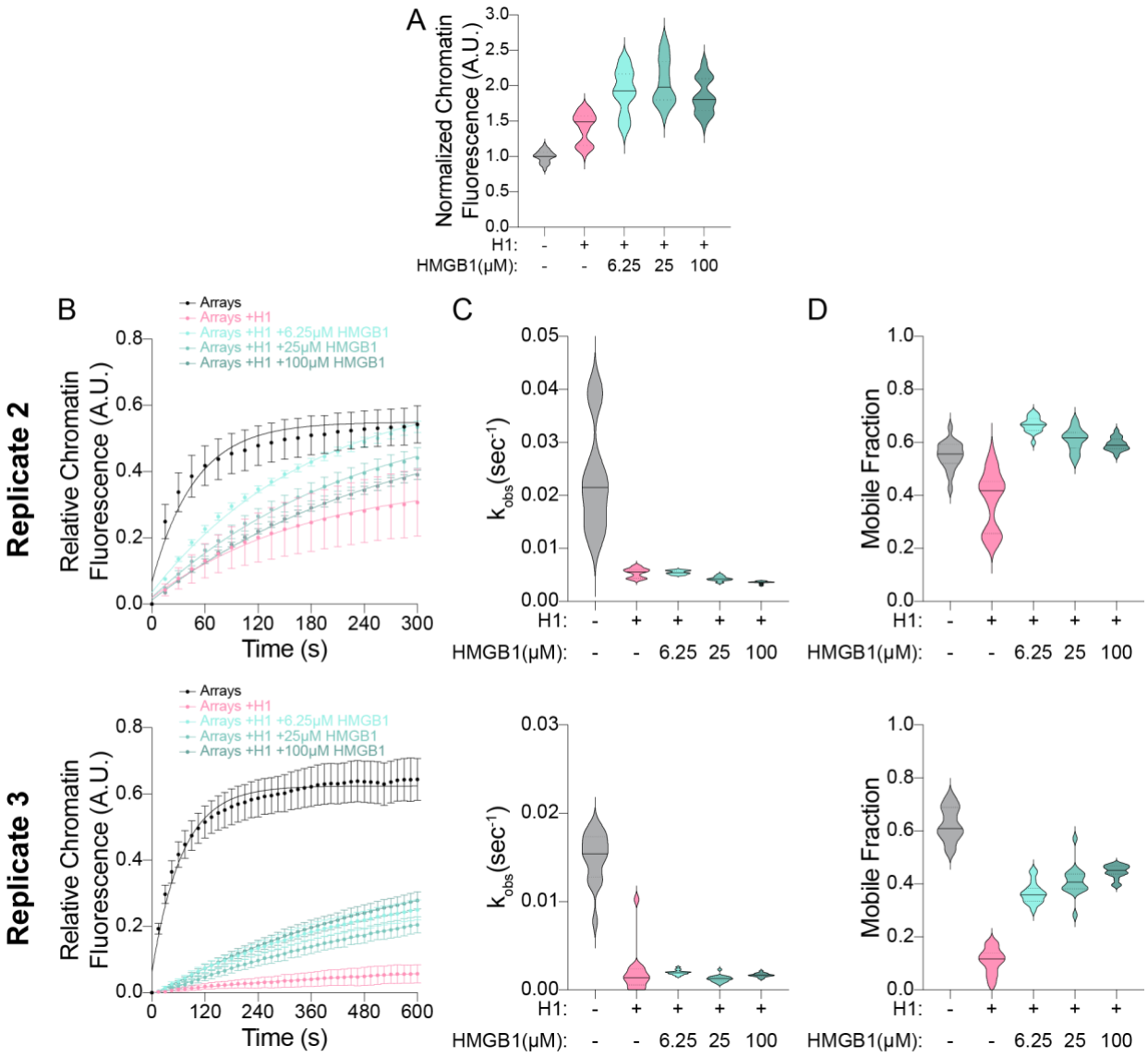

Figure S2.10 Additional replicates of H1-chromatin recovery
(A) Violin plots of the quantification of the average Alexa647 12x601 chromatin array fluorescence intensity within chromatin condensates. All values are normalized to chromatin alone. Solid and dotted lines represent the median and interquartile values respectively. Values represent an average of three experimental replicates with n>10 condensates per replicate. **(B)** Quantification of the fluorescence recovery after photobleaching of Alexa647-12x601 arrays within condensates. Values are normalized from 0 to 1 corresponding to post and pre-bleach respectively. Points represent a single experimental replicate with n>10 condensates. Error bars represent standard deviation of these same replicates. Data are fit to a one-phase exponentially association. **(C and D)** Violin plots of the quantification of the fits to the FRAP data in (F). The rate constant for recovery (k_{obs}) and the plateau of recovery (Mobile Fraction) are plotted for the five different conditions in (G) and (H) respectively. Solid and dotted lines represent the median and interquartile values respectively.

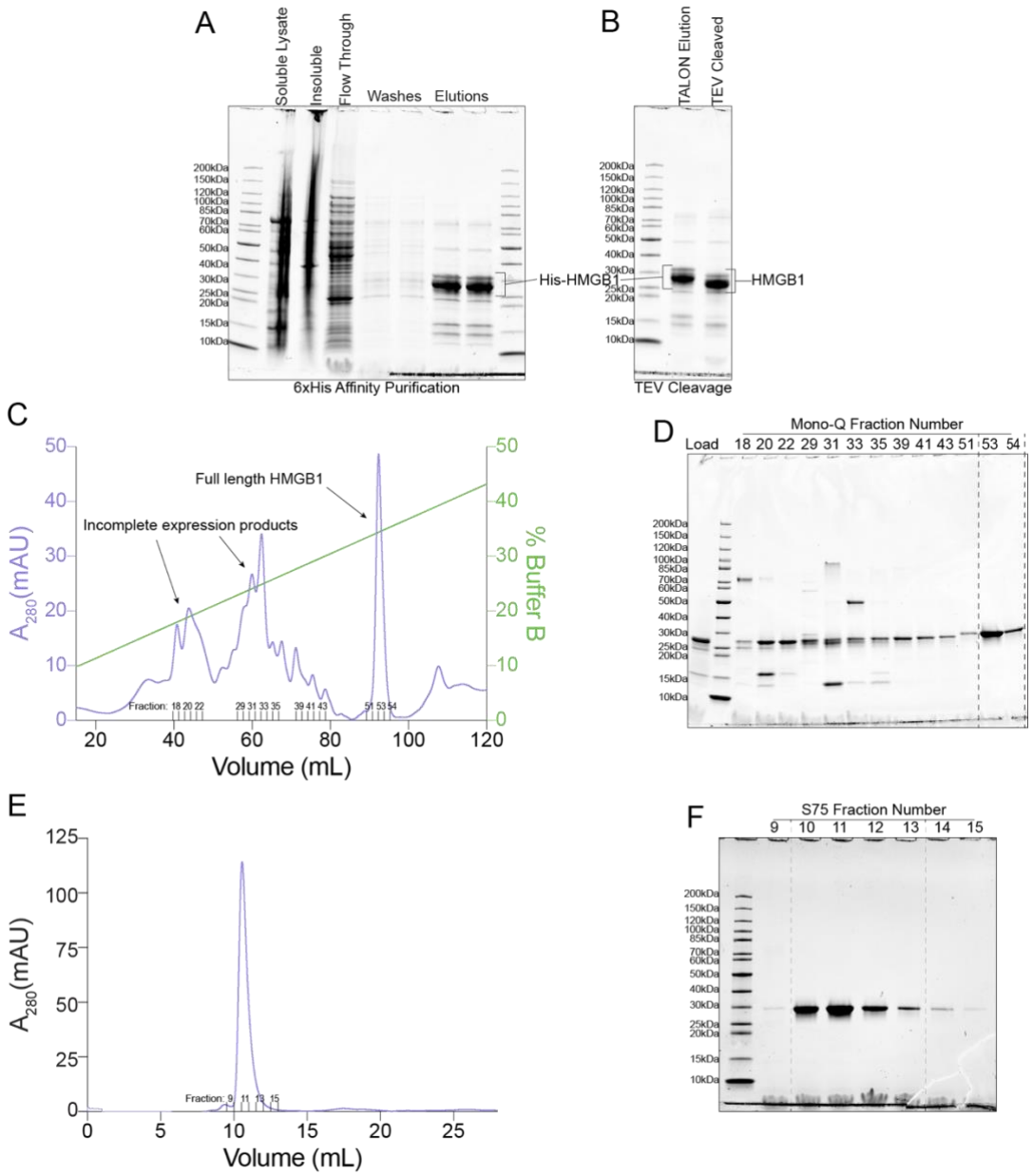

Figure S2.11 Purification of *Homo sapiens* HMGB1

(A) A gel showing the 6xHis pulldown of His-tagged HMGB1 using TALON resin. **(B)** A gel showing the cleavage of the 6xHis tag from HMGB1 using TEV protease. **(C)** A chromatogram of an anion exchange MonoQ run used to purify HMGB1. A_{280} is plotted on the left y-axis in purple to show where protein elutes from the column, while the % Buffer B (100% Buffer B = 1.5M KCl) is plotted on the right y-axis in green. Full length HMGB1 comes off between 32-35% Buffer B (~500mM KCl), while incomplete expression products elute at lower ionic strength, due to the lack of a complete C-terminal tail which is negatively charged. Fraction numbers that were run on a gel (D) are indicated. **(D)** A gel of MonoQ fractions from (C) in addition to what was loaded onto the MonoQ column (lane 1). Dashed lines represent the fractions that were pooled. **(E)** A chromatogram of a Superdex 75 Increase run used to purify HMGB1. Fractions numbers that were run on a gel (F) are indicated. **(F)** A gel of Superdex 75 Increase

fractions showing purified HMGB1. Dashed lines represent the fractions that were pooled.

Supplementary Table 1: Cryo-EM data collection, model refinement and validation statistics

Data collection and processing	
Sample	HMGB1 with 0/10 nucleosome
Grid type	Quantifoil R1.2/1.3 200 mesh Au
Microscope	Titan Krios
Voltage	300 kV
Camera	K3
Energy filter	yes
Filter slit width (eV)	20
Magnification	105,000
Pixel size	0.834
Total electron exposure ($e^-/Å^2$)	43
Defocus range (μm)	(-0.8) - (-2.0)
Automation software	SerialEM
Micrographs after curation	6,281
Particle picker	cryoSPARC template picker
Total particles extracted	8,562,925
Particles in initial consensus refinement	339,268
Reconstruction	**EMDB XXXXX**
Subset	HMGB1 Box A at SHL -2
Software	cryoSPARC Non-uniform Refinement
Final particles (dupl. removed)	47,813
Symmetry	C1
Resolution, global (Å)	
FSC 0.5 (unmasked / masked)	7.6 / 3.2
FSC 0.143 (unmasked / masked)	3.9 / 3.0
Local resolution range (Å)	1.8 - 6.6
3DFSC Sphericity	0.865
Sharpening B-factor ($Å^2$)	-68.8
Model Composition	**PDB YYYY**
Protein residues	824
DNA	308
Model Refinement	
Refinement package	COOT/Phenix/ISOLDE
Model-to-map CC	0.85
R.m.s. deviations	
Bond lengths (Å)	0.009
Bond angles (°)	1.459
Validation	
Map-to-model FSC 0.5	3.1
Ramachandran (%)	
Outliers	0.00
Allowed	1.00
Favored	99.00
MolProbity score	0.60
Poor rotamers (%)	0.46
Clashscore (all atoms)	0.26
C-beta deviations	0.00
CaBLAM outliers (%)	0.64
EMRinger score	4.56

Chapter 3: A proteomic search for nucleosome deforming proteins

3.1 Abstract

Nucleosome conformational dynamics are heavily influenced by the binding of chromatin proteins. Here we report a proteomics-based assay to identify chromatin proteins that induce conformational deformation of the histone octamer core. The results of this screen emphasize the consequence of disrupting nucleosome conformational change on the binding of a number of chromatin proteins. This work further implicates nucleosome conformational dynamics in the regulation of a number of chromatin processes, which as of yet have not been studied in this context. Finally, this screening platform is highly adaptable and could serve as a basis to explore not only the effect of nucleosome conformational dynamics on a variety of other nuclear factors but also to further understand the nature of nucleosome dynamics.

3.2 Introduction

The core unit of chromatin, the nucleosome, consists of ~147bp of DNA wrapped around an octamer of histone proteins. The histone octamer is made up of a single H3/H4 tetramer sandwiched by two H2A/H2B dimers (Luger et al., 1997). Each histone additionally contains flexible and unstructured tails which protrude from the nucleosome. The nucleosome is a dynamic macromolecular complex. In addition to the transient unwrapping of nucleosomal DNA described in Chapter 2, the histone octamer core is conformationally dynamic and deformable (Armache et al., 2019; Armeev et al., 2021; Bilokapic et al., 2018a, 2018b; Prior et al., 1983; Sanulli et al., 2019; Sinha et al., 2017). Indeed, conformational dynamics of the histone octamer have been shown to correlate

with the unwrapping of nucleosomal DNA and DNA translocation around the octamer (Armeev et al., 2021; Bilokapic et al., 2018b, 2018a). In this way, the dynamics of the histone octamer are inextricably linked to the accessibility of nucleosomal DNA. In addition to altering DNA accessibility, histone conformational dynamics could alter the chemical environment of the face of the histone octamer and the overall shape and structure of the nucleosome, potentially modifying the interaction surface for many nucleosome-binding proteins. However, how histone conformational dynamics correlate with binding of various chromatin proteins remains largely unknown.

There are many different ways chromatin proteins interact with the nucleosome – through the histone tails, the nucleosomal DNA, and the histone octamer core (Skrajna et al., 2020). Conformational dynamics within the octamer core could alter the structure or availability of all of these substrate cues, and correspondingly, the binding of various chromatin proteins could induce changes in histone octamer conformational dynamics. Indeed, this has been seen in the case of the *S. pombe* heterochromatin protein Swi6 and the mammalian ATP-dependent chromatin remodeling enzyme SNF2h (Armache et al., 2019; Sanulli et al., 2019; Sinha et al., 2017). Nuclear magnetic resonance (NMR) and cryo-EM studies have shown changes in histone octamer conformational dynamics when bound by Swi6 or SNF2h. These results suggest that binding of these proteins to the nucleosome is coupled to a conformational change of the nucleosome. Any chromatin protein that interacts with the nucleosome has the potential to conformationally deform the octamer core, so conformational dynamics are likely to affect the binding of many chromatin proteins. However, this possibility has not been

thoroughly investigated due to the technical difficulty of in-depth structural studies. Therefore, a high throughput method to explore the connection between histone octamer dynamics and nucleosome binding of various chromatin proteins would be of great interest.

To address this, a method to inhibit histone octamer dynamics is necessary. Conveniently, deformations of the octamer core can be inhibited by directing dicysteine crosslinks to limit conformational rearrangements between two regions of the histone octamer (Frouws et al., 2018; Sanulli et al., 2019; Sinha et al., 2017). In the case of Swi6, dicysteine crosslinking weakens the binding affinity of Swi6 for the nucleosome. This effect can be explained by a thermodynamic cycle where nucleosome binding is coupled to a conformational change or deformation of the histone octamer (Figure 3.1A). By inhibiting the conformational change, the dicysteine crosslink also weakens the overall binding affinity of the protein for the nucleosome (Figure 3.1B). This difference in binding affinity provides an opportunity to search for other chromatin proteins which may contain nucleosome-deforming activity. We sought to make use of this difference in affinity to design a high throughput assay that identifies nucleosome deforming proteins. We developed a proteomic screening pipeline that detects chromatin proteins from nuclear extracts that prefer to bind conformationally flexible nucleosomes. This pipeline identifies proteins whose nucleosome binding activity is likely coupled to conformational change and deformation of the histone octamer core. We find that dicysteine crosslinking within the octamer core has a broad effect on proteins with a variety of interaction modes with the nucleosome. These proteins are

involved in many different chromatin processes including chromatin remodeling, chromatin modification, and transcription. This suggests that histone octamer dynamics serves as a central point of regulation for numerous nuclear processes.

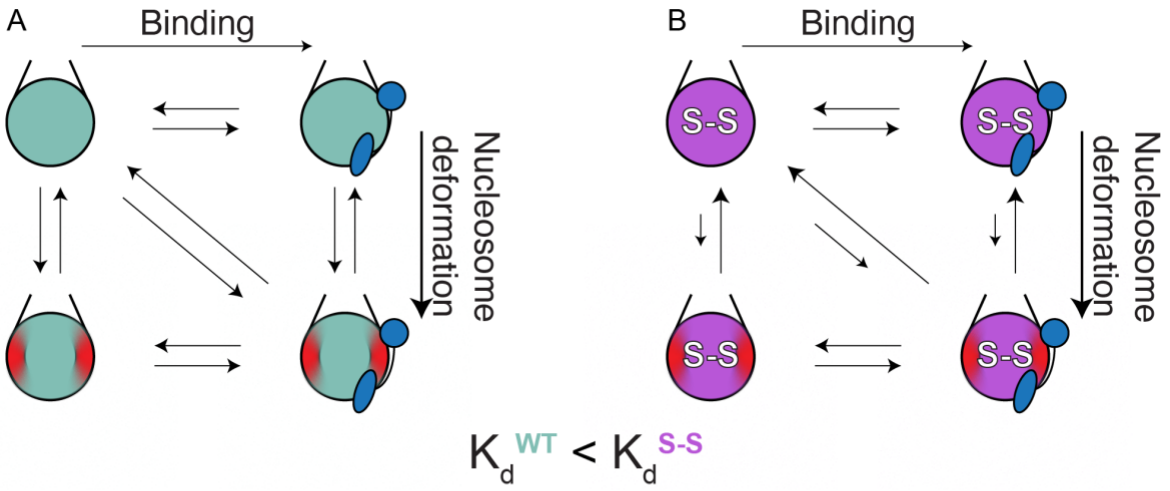

Figure 3.1 Thermodynamic basis of nucleosome deformations and how dicysteine crosslinks inhibit binding affinity
(A) A thermodynamic cycle where binding of a chromatin protein (blue) to the nucleosome is coupled to the conformational change of nucleosome deformation. **(B)** The same thermodynamic cycle as in (A) except the nucleosomes have been dicysteine crosslinked to inhibit the conformational change of nucleosome deformation. In this way, the dicysteine crosslink also limits the binding affinity of the chromatin protein to the nucleosome, because nucleosome deformation is coupled to nucleosome binding. This results in a higher dissociation constant (K_D) and weaker affinity of the chromatin protein for the dicysteine crosslinked nucleosomes.

3.3 Results

3.3.1 Validating affinity purification of dicysteine-crosslinked nucleosomes

Previous studies have shown how disruption of histone octamer dynamics by insertion of a dicysteine crosslink results in weakened binding affinity of a nucleosome-binding protein (Sanulli et al., 2019). We sought to explore what other chromatin proteins may also share this preference for conformationally free nucleosomes. We decided to test this initially using a dicysteine crosslink at the interface of two histones within the H3/H4 tetramer (Figure S3.1A, H3-L82C & H4-V81C) that has been shown to disrupt SNF2h nucleosome remodeling (Sinha et al., 2017). Histone octamers containing this dicysteine pair can be induced to form a disulfide bond via oxidation or kept in the

reduced state (Gamarra and Narlikar, 2021) (Figure S3.1A). These oxidized and reduced histone octamers (as well as wildtype histone octamer) are assembled into nucleosomes on a 200bp DNA template containing the 601 nucleosome positioning sequence followed by 53bp of flanking DNA, modified with biotin on the free end of DNA (Figures 3.2A, 3.2B, S3.1B and S3.1C). These nucleosomes are then conjugated to magnetic Streptavidin Dynabeads (Figure 3.2B). After one hour incubation in HeLa nuclear extract, followed by washing, all proteins are eluted from the beads using SDS sample buffer lacking reducing agent (Figure 3.2D and 3.2E). Samples were then analyzed on a non-reducing SDS-PAGE gel to assess the oxidation state of the dicysteine nucleosomes as described previously (Gamarra and Narlikar, 2021) (Figure 3.2E). As a control, we confirm that the redox state of the dicysteine pair survives the reducing environment of HeLa nuclear extracts (0.5mM DTT) (Figure 3.2E). This confirms that the redox state of the dicysteine pair persists through the experimental timeframe, enabling us to make quantitative comparisons of the abundance of nucleosome binding proteins based on the conformational flexibility of nucleosomes.

This SDS-PAGE analysis revealed no obvious detectable appearance or disappearance of protein bands based on the presence of the dicysteine crosslink, suggesting the need for a more sensitive technique to uncover differences in protein abundance. To do so, we turned to liquid chromatography-tandem mass spectrometry (LC-MS^2). Bead-conjugated nucleosomes were similarly incubated in HeLa nuclear extract and washed before being subjected to on-bead trypsin digestion to prepare peptides for LC-MS^2. Relative protein abundance was inferred using the number of spectral counts, which

represents the number of times a peptide of a given protein is detected by the mass spectrometer (Figure 3.3B). Using this quantitation method, we were able to confirm that control proteins (the core histones, streptavidin and trypsin) were present in relatively equal abundance in all three of our conditions: wildtype, dicysteine reduced, and dicysteine oxidized (Figure 3.3C). Although we do detect slightly elevated levels of H4 in the dicysteine oxidized conditions, which may represent different efficiency of nucleosome assembly, the core histones are largely present in equal amounts in all our conditions (Figure 3.3C), thus facilitating quantitative comparison of the presence of other chromatin proteins.

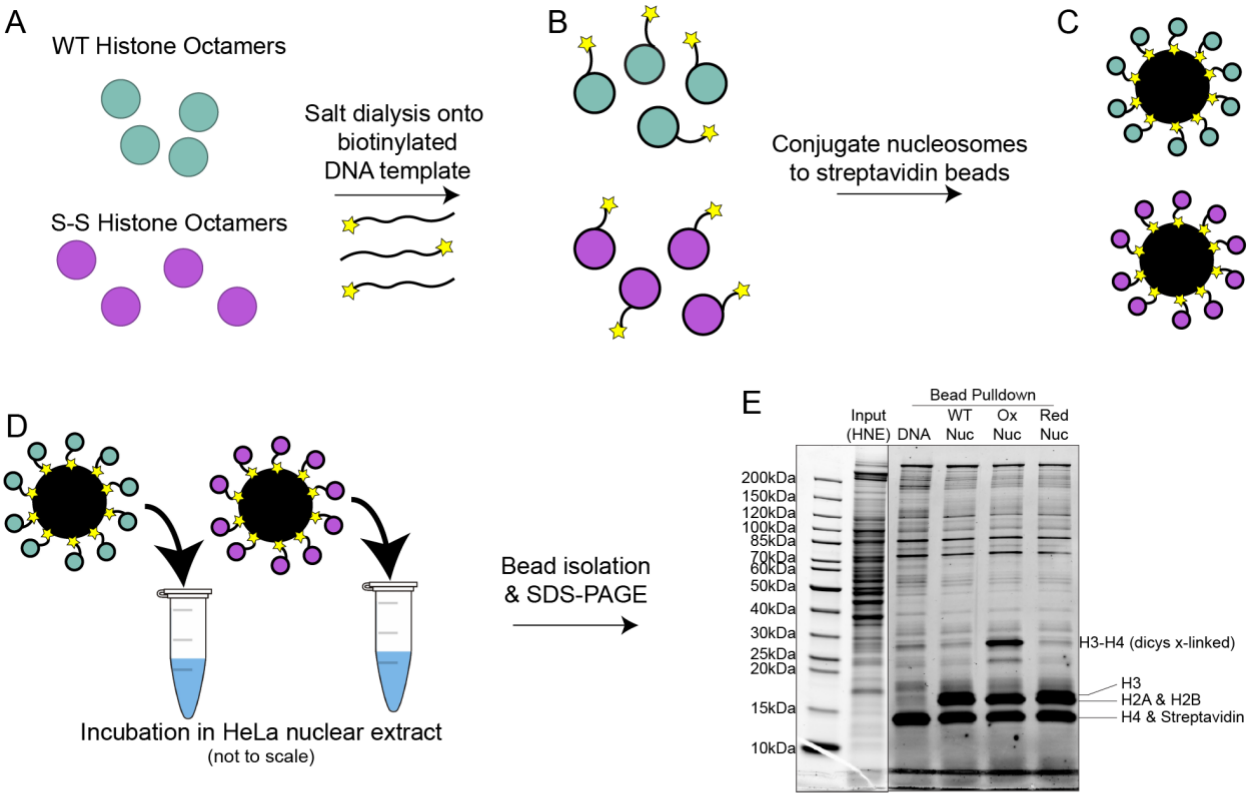

Figure 3.2 Schematic of a proteomic screening platform to identify potential nucleosome deforming proteins
(A) Wildtype (WT) and dicysteine crosslinked (S-S) histone octamers are assembled onto a 200bp biotinylated DNA template via the standard salt gradient dialysis method. **(B)** Wildtype and dicysteine crosslinked nucleosomes are conjugated to streptavidin-coated DynaBeads via the interaction between biotin and streptavidin. **(C)** DynaBeads conjugated with wildtype and dicysteine crosslinked nucleosomes are incubated in HeLa nuclear extract to allow binding of chromatin proteins. **(D)** Dynabeads are then removed from HeLa nuclear extract using a magnet, washed in buffer, and then eluted in SDS Sample Buffer. Eluted proteins are then separated using SDS-PAGE and imaged using Sypro protein stain. The core histones (H3, H4, H2A & H2B) and streptavidin are identified as the most abundant proteins along with a variety of interacting chromatin proteins.

3.3.2 Quantitative comparison of chromatin proteins dependent on nucleosome conformational state

To determine whether a protein is specifically sensitive to the dicysteine bond in the oxidized state and not merely the dicysteine mutation, we used both wildtype nucleosomes and dicysteine reduced nucleosomes as controls (Figure 3.3A). Pairwise comparisons between all three samples highlight the necessity of these controls. Volcano plots of each pairwise comparison among the three conditions reveal that, on the whole, fewer proteins bind to dicysteine oxidized nucleosomes, whether comparing to wildtype or dicysteine reduced nucleosomes (Figure S3.2A and S3.2B). This suggests that inhibiting nucleosome conformational dynamics is generally inhibitory to nucleosome binding, which is consistent with the hypothesis that many proteins induce a conformational change in the histone octamer core upon binding. When comparing the wildtype and reduced conditions to determine the effect of the dicysteine mutation, we see that some proteins prefer wildtype nucleosomes, while relatively fewer prefer binding dicysteine reduced nucleosomes (Figure S3.3C). This suggests that merely the introduction of these cysteine residues disrupts the proper interaction of some chromatin proteins or in some cases, could introduce spurious interactions with the chromatin proteins. To properly identify chromatin proteins which deform nucleosome conformation, we must control for both of these types of effects.

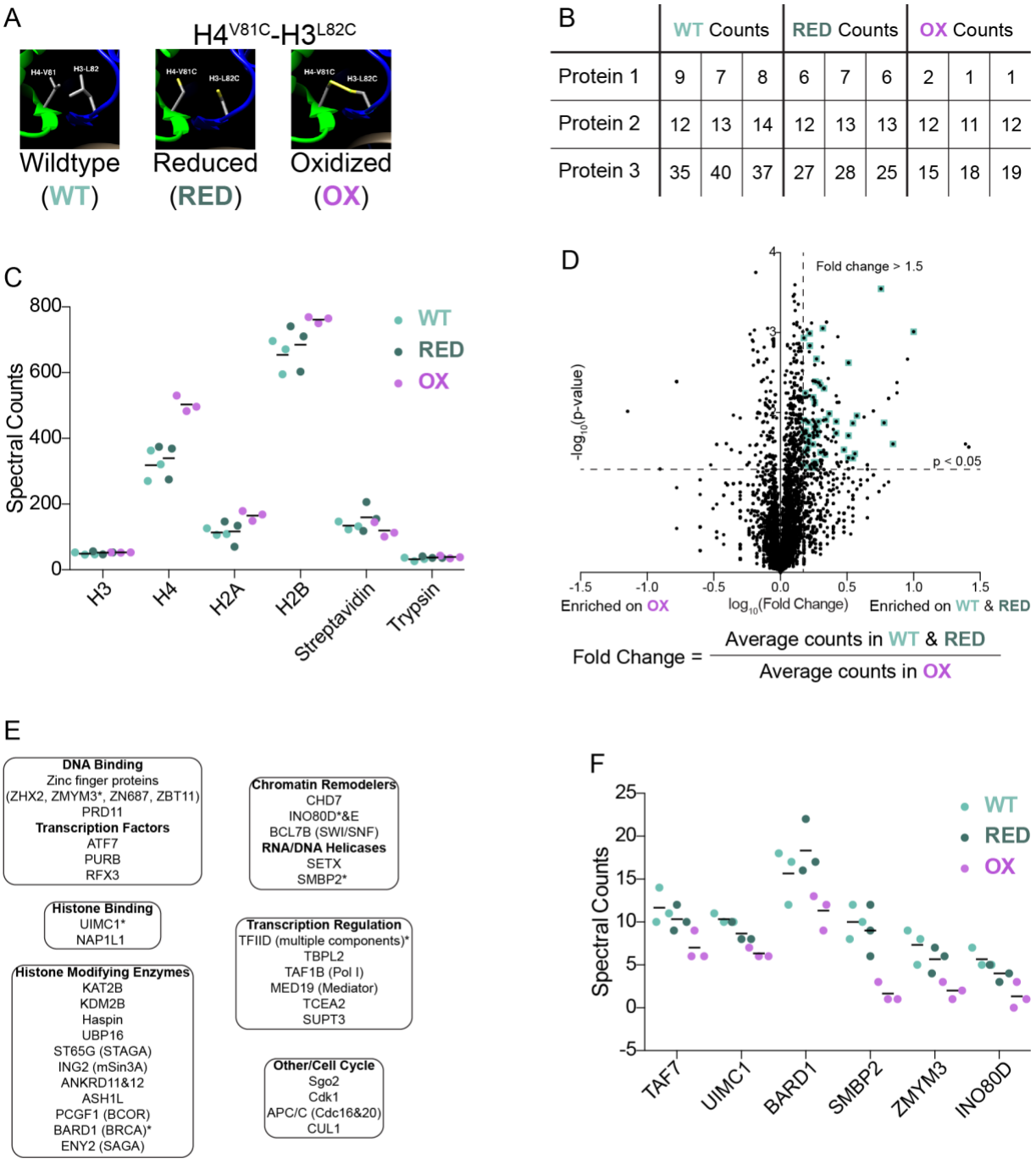

Figure 3.3 Results of a proteomic screen to identify nucleosome deforming proteins
(A) Stick diagrams showing the location between histone H3-L82 and H4-V81 where the dicysteine mutation is placed and oxidized. The three conditions tested are wildtype histones, dicysteine mutated with a reduced disulfide bond, and dicysteine mutated with an oxidized disulfide bond. **(B)** A sample showing hypothetical spectral counts for three proteins. Each condition (wildtype, reduced & oxidized) is performed in biological triplicate resulting in three spectral count values for each protein for each condition. **(C)** Spectral counts are plotted for the core histone (H3, H4, H2A & H2B), streptavidin and trypsin, which should all be present in equal amounts in the three conditions. Lines mark an average number for the three replicates for each condition. **(D)** A volcano plot for the results of the proteomic screen. The negative $\log_{10}$ of the p-value (calculated using a two-tailed T-test) is plotted as a function of the $\log_{10}$ value of the fold change between the average spectral counts of the conformationally-free conditions (WT & reduced) and the conformationally-restricted condition (oxidized). Cutoffs of fold change > 1.5 and $p < 0.05$ are marked with dashed lines. After manually removing homologous and junk proteins, hits are highlighted in turquoise. **(E)** A list of the hits identified by the analysis in (D), separated into categories based on function. **(F)** Spectral counts are plotted for a subset of the hits identified in (D) and marked with * in (E). Lines mark an average of the three replicates.

To make this comparison, we first combined the wildtype and dicysteine reduced conditions. This allowed us to directly compare between all conformationally free nucleosomes and the conformationally restricted (dicysteine oxidized) nucleosomes. Consistent with pairwise comparisons, we see that generally the disulfide bond oxidation inhibits chromatin binding proteins (Figure 3.3D). This is consistent with our model that restricting conformational dynamics inhibits binding of proteins whose binding is coupled to conformational rearrangement of the nucleosome. For this reason, we focused on proteins whose binding was inhibited by the dicysteine crosslink by at least 1.5-fold. We then performed a two-tailed t-test between the wildtype and dicysteine reduced datasets and threw out any hits that had a significant difference between these conditions ($p<0.05$). In this way, we remove any proteins that are sensitive to the dicysteine mutation itself and instead highlight the proteins that are sensitive to the presence of the disulfide bond. After manually removing artifacts such as non-nuclear proteins, we are left with 53 proteins determined as hits (Figure 3.3D and 3.3E). Spectral count data for a subset of these proteins validates that their abundance is specifically decreased in the oxidized condition and relatively similar in the wildtype and reduced conditions (Figure 3.3F). These proteins represent candidates for chromatin proteins and complexes that have the potential to induce conformational rearrangement of the histone octamer core upon binding.

The hits identified using this screening method represent a wide variety of chromatin-interacting proteins (Figure 3.3E). Many of the hits are known histone-interacting proteins, such as UIMC1 and NAP1L1, consistent with the idea that direct histone

binding is coupled to deformation of the octamer core. Additionally, a number of the hits are from complexes involved in enzymatic activities on chromatin. Both ATP-dependent chromatin remodelers (SWI/SNF, Chd7, and INO80) and histone tail post translational modifiers (KAT2B, Haspin, etc.) are identified. In addition, a number of hits are DNA-binding proteins, highlighting the interplay between nucleosomal DNA accessibility and histone octamer dynamics (Armeev et al., 2021; Bilokapic et al., 2018a, 2018b). These findings underscore the fact that histone octamer deformations are inherently coupled to dynamics of the nucleosome as a whole, and present a list of interesting candidates that may alter nucleosome conformational dynamics

3.4 Discussion

Here we have described the development of a proteomic screening pipeline to identify proteins which have the potential to deform histone octamer conformational dynamics. Below we will discuss the implications of the proteins that we have identified in this preliminary screen along with future iterations of the screen which could yield more information about nucleosome conformational dynamics.

The most obvious and easily explainable hits identified by this screen are proteins that directly interact with histones such as NAP1 and UIMC1 (Rap80), which we now propose as nucleosome-deforming proteins. NAP1 is a nucleosome assembly and disassembly factor which binds specifically to the H2A/H2B dimer (Okuwaki et al., 2010). We speculate that breaking histone-histone contacts within the octamer is essential to the process of nucleosome assembly and disassembly. Therefore, covalently linking two histones together would likely inhibit this process. This result also

hints at the possibility that H2A/H2B conformational dynamics are tightly linked to the dynamics of H3/H4, where the dicysteine pair was located, or that NAP1 additionally interacts directly with the H3/H4 tetramer. Rap80, a component of the BRCA1 complex, binds directly to ubiquitylated H2A and targets the BRCA1 complex to sites of DNA damage (Sobhian et al., 2007; Wu et al., 2009). This connects histone octamer dynamics to the process of DNA damage repair. It is possible that using a substrate with a blunt DNA end is specifically activating a DNA repair pathway in the nuclear extract, thus biasing our screen towards DNA repair machinery. However, even when controlled against conformationally free nucleosomes, we see a decrease in the amount of Rap80 and BARD1, which is also a part of the BRCA1 complex, suggesting that the BRCA1 DNA damage repair pathway specifically involves deformations of the histone octamer. Iterative screens using modified DNA templates with various damaged DNA substrates could further elucidate this mechanism along with follow up biophysical studies of how the BRCA1 complex interacts with nucleosomes. Indeed, there are reported cryo-EM structures of BRCA1 and BARD1 bound to nucleosomes (Hu et al., 2021). However, these were determined in the presence of chemical crosslinkers which would limit any effects on nucleosome conformational dynamics.

Other enzymes, such as ATP-dependent chromatin remodelers, often interact directly with the histone octamer. This screen has identified members of the INO80, CHD, and SWI/SNF family of remodelers as being sensitive to octamer conformational dynamics. Although previous work suggested that the ISWI family induces octamer deformation and is sensitive to this dicysteine pair (Sinha et al., 2017), that effect is an enzymatic

effect and not due to a decrease in binding affinity that we were screening for with this approach. Indeed, it has been proposed that the INO80 and SWI/SNF family of remodelers could distort the histone octamer to facilitate DNA translocation (Côté et al., 1994; Hsieh et al., 2022; Imbalzano et al., 1994; Kwon et al., 1994; Wu et al., 2023). However, a limit of this screening technique is that we are enriching for abundant and stable nucleosome-interacting proteins, while many remodelers are low in abundance and may interact quite transiently, limiting our sensitivity to such proteins. Activity-based iterations of this screen could be implemented by monitoring nucleosome position as a product. Crosslinks in various regions of the histone octamer could be used to determine whether dynamics in different regions are more or less important for remodeling. This could inform more broadly on how histone octamer conformation is related to nucleosome translocation and the activity of remodelers. Alternatively, ATP analogs could be used to facilitate more stable interactions between ATPases and the nucleosome.

To our surprise, a number of other chromatin modifying enzymes that act on the histone tails appeared as hits in this screen (KAT2B, KDM2B, Haspin, UBP16, STAGA, mSin3A, etc.) Since we were looking for dependencies on histone core dynamics, the presence of histone tail-modifying enzymes as hits was not expected. It is possible that we have identified novel octamer interactions for some of these complexes like in the case of the lysine methyltransferase SUV420H1 (Abini-Agbomson et al., 2023). However, a more direct way to understand how these enzymes are influenced by octamer conformational dynamics would be to monitor the products of these enzymes: histone tail modifications.

This platform could easily be adapted to quantify differences in various histone post-translation modifications, which would more directly implicate histone octamer dynamics in these enzymatic processes. Regardless, the binding preferences identified here suggest that the conformational dynamics of the nucleosome as a whole are correlated. Indeed, the histone tails (especially the H3 tail) are heavily involved in regulating the accessibility of nucleosomal DNA (Ghoneim et al., 2021; Polach et al., 2000). Additionally, changes in nucleosomal DNA wrapping are accommodated by structural changes of the histone octamer core (Armeev et al., 2021; Bilokapic et al., 2018a, 2018b), thus providing a link between histone octamer core dynamics and histone tail dynamics. Therefore, nucleosome dynamics as a whole could serve as a signaling hub, coordinating enzymatic modification of histone tails with regulation of nucleosomal DNA accessibility and deformations of the histone core.

The interconnectedness of nucleosome conformational dynamics as a whole would also explain the prevalence of DNA-binding proteins identified in our screen. To better understand how DNA-binding proteins impact nucleosome dynamics, it would be interesting to adapt our screening platform to target specific DNA-binding proteins by inserting sequences of interest within our nucleosome template, either within the nucleosomal DNA or in the flanking DNA. Similarly, instead of mononucleosomes, longer chromatin arrays (either containing 601 sequences or native genomic sequences) could be used to probe mesoscale effects of octamer dynamics.

Our screen also identified a number of transcription-associated proteins and complexes (TFIID, RNA Pol I, Mediator, etc.), which tells us that transcription of a chromatinized template is likely to involve deformation of the histone octamer. Like the prevalence of DNA damage related proteins, this likely tells us how our substrate is being acted upon by the nuclear extract, which biases the pool of chromatin proteins we identify. To this extent, this screen could be modified to target separate pools of chromatin proteins. For example, H3K9me3 nucleosomes could be used to specifically identify heterochromatin proteins that affect histone octamer dynamics. This would also facilitate the opportunity to benchmark our hits using the heterochromatin protein HP1, which was shown to have a binding preference for non-crosslinked histone octamers only when the H3K9me3 mark is present (Sanulli et al., 2019).

Finally, while we have performed this screen using only one specific dicysteine pair within the H3/H4 tetramer interface, there are a variety of different dicysteine pairs that have previously been deployed to study octamer dynamics (Frouws et al., 2018; Sanulli et al., 2019; Sinha et al., 2017), which could yield information on the variety of octamer deformations that are possible. For example, do crosslinks within the H2A/H2B dimer yield similar or different results to those used in the H3/H4 tetramer? It is possible that these sorts of iterative screens could start to reveal specific allosteric networks within the nucleosome. Or it is possible that disruption of dynamics at any site within the octamer is similarly deleterious. To this extent, non-specific chemical crosslinkers such as formaldehyde or glutaraldehyde could be employed to study the effect of disrupting nucleosome dynamics as a whole.

This proteomic screening platform could serve as the basis for further exploration of the importance of nucleosome conformational dynamics. We have identified a number of novel chromatin proteins and complexes which we implicate in deformation of the histone octamer. These hits should be investigated using careful biochemical and biophysical studies to understand their effects on nucleosome structure and dynamics. We believe these studies will shed light on the role of nucleosome conformational dynamics as an essential point of the regulation of all chromatin processes.

3.5 Materials and Methods

Assembly of oxidized and reduced dicysteine octamers and nucleosomes

Histone octamer refolding of dicysteine histones (H3-L82C & H4-V81C) was performed exactly as described in Chapter 2, except in strong reducing conditions (10mM DTT) to keep the cysteines reduced. After octamer is purified by size exclusion, half is kept as reduced and half is removed to undergo oxidation of the dicysteine pair to form a disulfide crosslink. This protocol for octamer oxidation is derived from (Gamarra and Narlikar, 2021).

This octamer was diluted to 0.5mg/mL and (~5μM) and dialyzed overnight at 4°C against 2L of buffer lacking reducing agent (10mM HEPES-KOH pH7.5 and 2M NaCl). A 10X of Copper:Phenanthroline (Cu:Phe) oxidizing agent (250μM $CuSO_4$:1mM Phenanthroline) is prepared in dialysis buffer and diluted into the octamer to 1X (25μM $CuSO_4$:100μM Phenanthroline). This is incubated at room temperature for 75 minutes before being quenched with 10mM EDTA (from a 100mM EDTA stock in dialysis buffer).

SDS-PAGE samples are prepared without reducing agent and at least 5X [reducing agent in reduced octamer sample] Iodoacetamide or N-ethylmaleimide (50mM IAA or 100mM N-EM). This cysteine alkylating agents modify any reduced cysteine residues to prevent formation of novel disulfide bonds after SDS denaturing. This alkylation reaction must go for at least an hour in the dark at room temperature. Samples are then boiled at 95°C for 5min before running on SDS-PAGE. After staining with Coomassie, the oxidized H3-H4 species can be identified as it runs ~25kDa (Figure S3.1A). Finally, Cu:Phe is fully removed by an additional overnight dialysis at 4°C in 2L of 10mM HEPES-KOH pH7.5, 2M NaCl and 1mM EDTA. This octamer can then be recovered and used like wildtype or reduced octamer in nucleosome assemblies.

Nucleosome assembly onto biotinylated DNA and purification over a glycerol gradient is performed identical to as it is described in Chapter 2 with the exception that reduced nucleosomes are assembled and purified in the presence of 3mM TCEP.

Attachment of biotinylated nucleosomes to Streptavidin Dynabeads

M-280 Streptavidin Dynabeads (Invitrogen) with a capacity of 10µg biotinylated dsDNA per mg Dynabeads (10mg/mL) were used. A typical reaction of 30µg of biotinylated nucleosomes was incubated with 300µL Dynabeads in 600µL buffer (50mM Tris-HCl pH8, 0.25mM EDTA, 75mM NaCl, 0.02% NP-40, 2.5% polyvinyl alcohol and 3mM TCEP only for dicysteine reduced conditions). Beads were first equilibrated into this buffer before addition of nucleosomes. Beads and nucleosomes were incubated together nutating (sometimes shaking was necessary to keep the beads in suspension for

smaller volumes) at room temperature for 45 minutes. Beads were then washed 2x with 300µL buffer before being stored at 4°C in 300µL buffer. Beads were only prepared with nucleosomes the day before being used in pulldown assays.

To quantify the efficiency of bead binding, 5µL of the supernatant from the binding reaction was digested with 5µL buffer (20mM Tris-HCl pH8, 10mM EDTA, 20% glycerol, 2% SDS) and 1µL ProteinaseK (NEB, 800U/mL) for 20 minutes at 50-55°C. This reaction was spun down and loaded onto a 5% acrylamide (29:1 acrylamide:bis) native PAGE gel with a standard curve of biotinylated DNA. The concentration of biotinylated DNA left over in the supernatant was used to infer the amount of nucleosomes bound the Dynabeads. Typically 80-90% of the 30µg of nucleosomes in the initial binding reaction were calculated to be bound to the beads.

HeLa cell nuclear extract preparation

HeLa nuclear extract was prepared according to (Nilsen, 2013). Five T182 flasks (182cm^2 surface area) of HeLa cells were grown to 100% confluency in DMEM GlutaMax (Gibco) supplemented with 1% Pennicillin-Streptomycin (Gibco) and 10% heat-inactivated fetal bovine serum (Sigma-Aldrich). Each flask was washed with 30mL warm phosphate-buffered saline (PBS). Cells were detached with 20mL Accutase (Millipore Sigma) at 37°C for ~5 minutes. 30mL of media with FBS was added to inactivate the Accutase before cells were pelleted by spinning at 1000 x g for 3 minutes at room temperature. Media was aspirated off and cell pellets were resuspended in 10mL total of cold PBS (2mL per pellet). Cells were then pelleted again and washed

again in 5mL cold PBS and pelleted again. The pelleted cell volume was estimated using markings on the side of the 15-mL falcon tube (typically ~350-450µL).

Cells were swollen by addition of 3x the pelleted cell volume of ice cold hypotonic buffer (10mM Tris-HCl pH8, 1.5mM $MgCl_2$, 10mM KCl, 0.5mM DTT, 1mM PMSF, 1µg/mL Pepstatin A, 3µg/mL Leupeptin, and 2µg/mL Aprotinin). Cells were lysed by pulling the swollen cell suspension through a 23G needle attached to a 5mL syringe on ice, taking care not to induce air bubbles. Cell lysis was checked by microscopy every 10 pulls (1 pull = 1 up and down) by adding 2µL cells with 2µL Trypan blue (Gibco) to a coverslip slide and estimating the percent of cells stained meaning the outer plasma membrane had been lysed and only the nucleus remained. Once 75-80% of cells had been lysed (typically between 30-40 pulls through the 23G needle), nuclei are isolated from the cytosolic supernatant by spinning at 2000 x g for 15 minutes at 4°C. The pelleted nuclear volume was measured using the markings on the side of the falcon tube (typically similar or slightly larger volume to the pelleted cell volume due to swelling).

Nuclei were resuspended in 0.5x low salt buffer (20mM Tris-HCl pH8, 25% glycerol, 1.5mM $MgCl_2$, 20mM KCl, 0.2mM EDTA, 0.5mM DTT, 1mM PMSF, 1µg/mL Pepstatin A, 3µg/mL Leupeptin, and 2µg/mL Aprotinin). High salt buffer (20mM Tris-HCl pH8, 25% glycerol, 1.5mM $MgCl_2$, 1.2M KCl, 0.2mM EDTA, 0.5mM DTT, 1mM PMSF, 1µg/mL Pepstatin A, 3µg/mL Leupeptin, and 2µg/mL Aprotinin) to a final concentration of 300mM KCl. High salt buffer was added dropwise with slow mixing of the solution to avoid lysing of nuclei with transiently high KCl concentrations. Salt extraction of nuclear proteins

proceeded for 30 minutes at 4°C while nutating. Extract was then separated from nuclei by pelleting at 21,100 x g for 30 minutes at 4°C. The supernatant of this spin is the nuclear extract, and was dialyzed against 20mM Tris-HCl pH8, 20% glycerol, 150mM KCl, 0.2mM EDTA, 0.5mM DTT, 1mM PMSF, 1µg/mL Pepstatin A, 3µg/mL Leupeptin, and 2µg/mL Aprotinin for 2 hours at 4°C. Going from 300mM KCl in the salt extraction to 150mM KCl in dialysis induced the precipitation of some material, so the nuclear extract was spu at 21,100 x g for 10 minutes at 4°C. The supernatant is then removed. The protein concentration within the extract is calculated using a Bradford Assay (Bio-Rad Protein Assay kit) against a BSA standard. Typical yields from 5 T182 flasks were ~5-10mg/mL of nuclear extract in ~300-400µL. Nuclear extract was flash frozen in liquid nitrogen and stored at -80°C.

Nucleosome affinity purification from nuclear extract

For a typical pulldown reaction, 5µg of nucleosomes attached to Dynabeads was incubated in 50µg HeLa nuclear extract in 100µL. Dynabeads-bound nucleosomes were equilibrated into binding buffer (20mM Tris-HCl pH8, 20% glycerol, 150mM KCl, 0.2mM EDTA, 0.1% NP-40, 0.5mM DTT, 1mM PMSF) with two washes of 100µL. Beads were then resuspended in 100µL of 0.5mg/mL HeLa nuclear extract (50µg). Chromatin proteins from the extract were allowed to bind for 1 hour at room temperature while the reaction was shaking to keep the beads in suspension. Beads were then washed 2x with 100µL of wash buffer (20mM Tris-HCl pH8, 75mM KCl, and 0.1% NP-40). Beads were either eluted in SDS sample buffer to run on a gel or prepared for mass spectrometry.

Peptide preparation for mass spectrometry

Trypsin digest to prepare peptides for mass spectrometry was performed on the beads. Beads were washed 2x with 100µL of 20mM Tris-HCl pH8 and 2mM $CaCl_2$, before they were resuspended in 9µL 20mM Tris-HCl pH8. All cysteines were reduced by addition of 0.4µL of 200mM DTT (~8.5mM final). Beads were incubated shaking for 30 minutes at room temperature. All cysteines were the alkylated by addition of 0.6µL 200mM iodoacetamide (12mM IAA final). Alkylation occurred for 20 minutes at room temperature while shaking and in the dark. 100ng of trypsin (0.25µL 400ng/µL stock, Promega) was added and samples were incubated overnight shaking at 37°C. In the morning, the supernatant was removed to a new tube add another 100ng of trypsin was added for 4 hours at 37°C. The remaining volume was measured, and the solution was acidified by addition of 50% formic acid to a final 2%. Samples were then desalted using C-18 ZipTips with 0.6µL resin (EMD-Millipore) according to manufacturer's instructions. Peptides were eluted in 10µL 70% acetonitrile and 0.3% trifluoroacetic acid. Samples were flash frozen in liquid nitrogen and lyophilized. Dried peptide samples were stored at -80°C mass spectrometry analysis.

Mass spectrometry

Peptide samples were resuspended in 0.1% formic acid for mass spectrometry analysis. Briefly, peptides were loaded onto a C18 column in 2% acetonitrile, before being eluted with a gradient of acetonitrile from 2 to 30% over 90 minutes. Peptides were ionized and

vaporized via electrospray ionization before tandem mass spectrometry (MS/MS or MS^2).

As ions enter the mass spectrometer, MS^1 scans are performed every 50ms or once $4x10^5$ ions have been collected. Initial m/z of the precursor ions are recorded at this point. Monoisotopic peaks from the MS^1 spectra are chosen starting with the most abundant ion in the spectra. Only ions with charge $2<z<7$ are considered and a minimum of $2x10^4$ ions. Each ion selected is then excluded to 30 seconds to maximize the number of ions analyzed by MS^2 scans.

Peptide fragmentation or MS^2 scans are induced using higher-energy C-trap dissociation (HCD). Product ions are measured at 30k resolution. Product ion mass, charge and intensity are stored in a table along with precursor ion mass, charge and intensity from MS^1 scans.

Mass spec data analysis

Peptide identification search was performed using Protein Prospector (UCSF). *Homo sapiens*, *Xenopus laevis* histones, trypsin, and streptavidin are used as reference proteomes. False discovery rates of 5% for peptides and 1% for proteins were used against a scrambled proteome. Spectral counts, or the number of times any peptide of a given protein is identified is used as a proxy for protein abundance.

3.6 Supplemental Figures

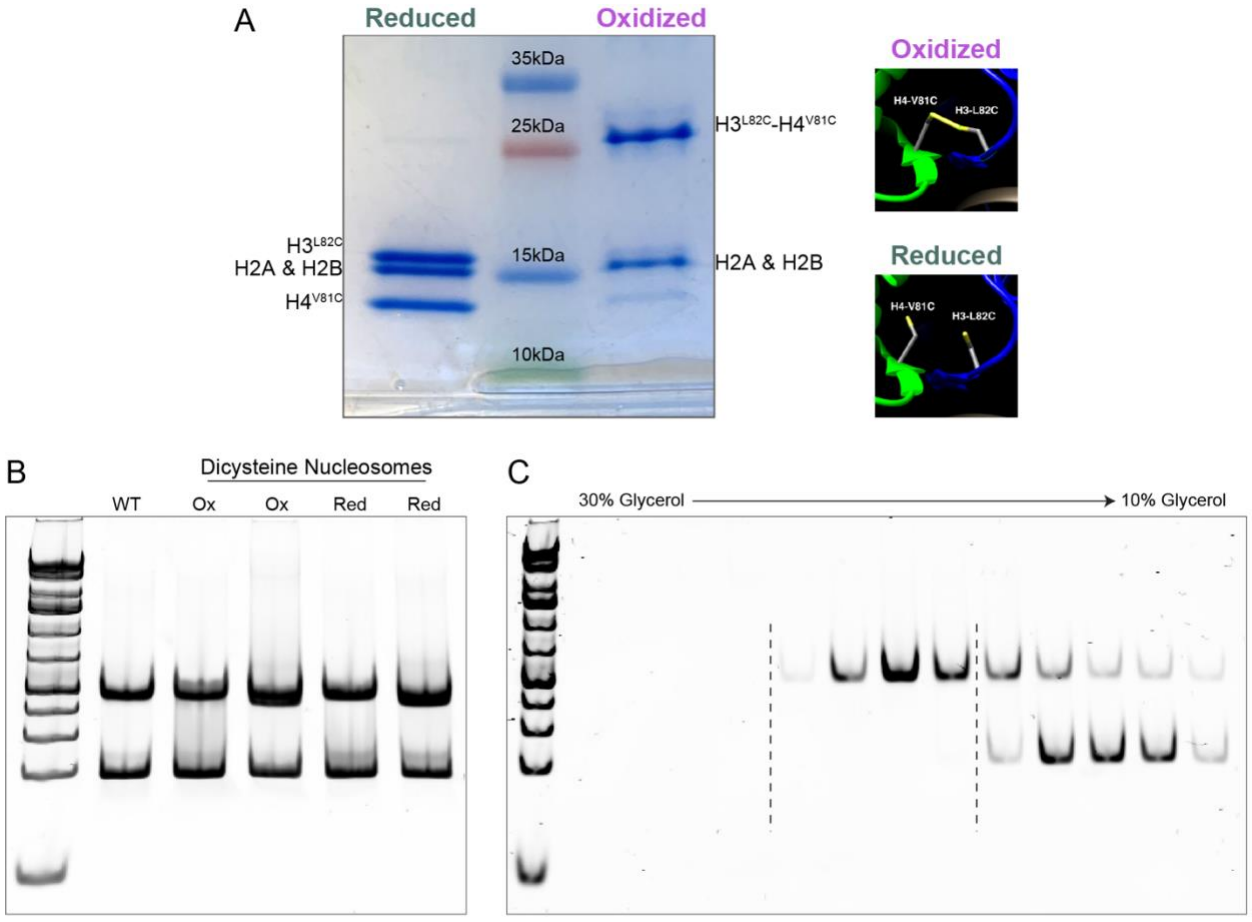

Figure S3.1 Validation of crosslinked histone octamer and nucleosomes
(A) SDS-PAGE of dicysteine-mutated purified histone octamers in both the disulfide reduced and oxidized states. When oxidized, a covalent interaction between H3 and H4 leads to an upward shift in those two bands. **(B)** A native PAGE of nucleosomes assembled on wildtype (WT), dicysteine oxidized (Ox) and dicysteine reduced (Red) histone octamers. The upper band represents fully assembled nucleosomes, while the lower band represents unassembled DNA. **(C)** A native PAGE of glycerol gradient fractions showing an example of purification of fully assembled nucleosomes from (B). Dashed lines represent the fractions that were pooled.

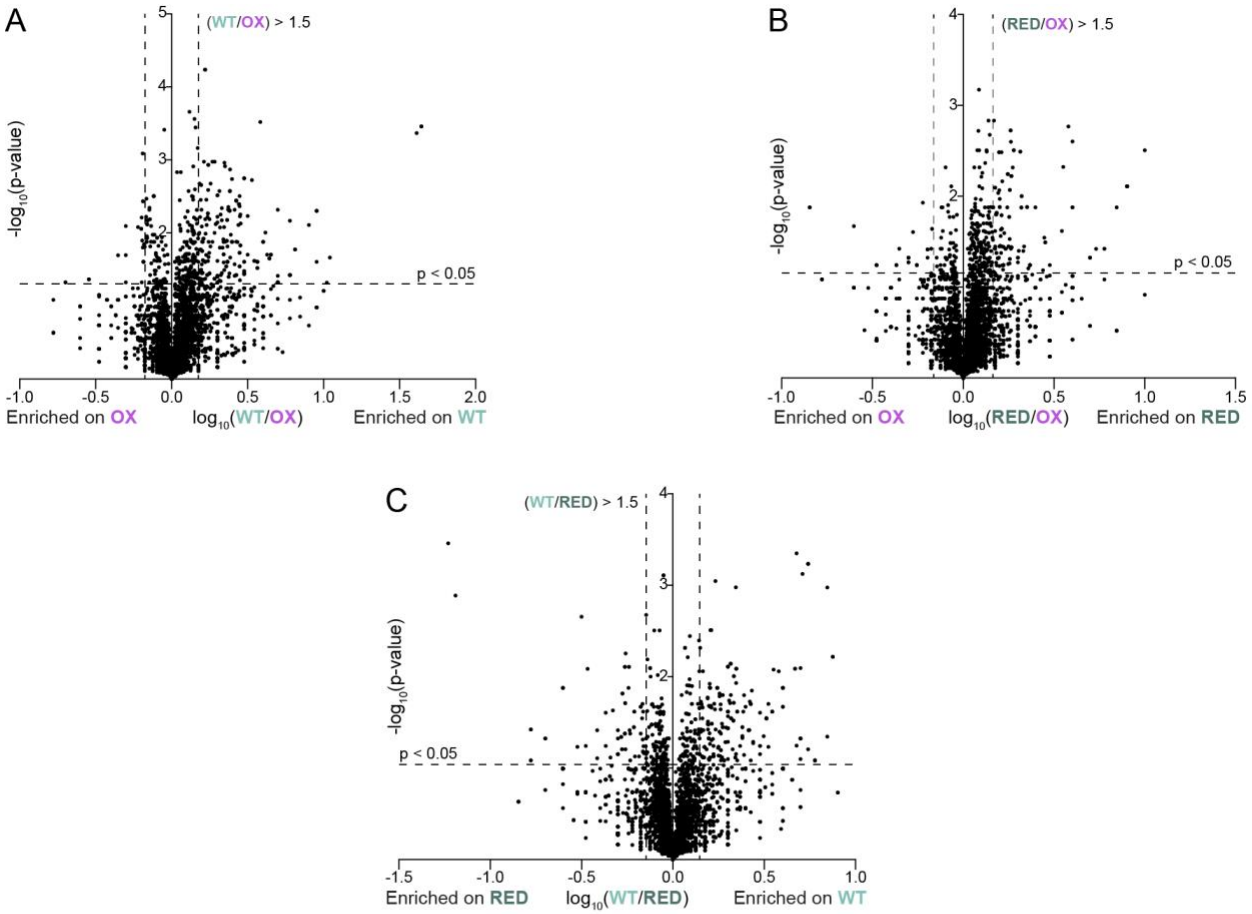

Figure S3.2 Pairwise comparisons of all three nucleosome pulldown conditions
(A, B and C) Volcano plots of the three pairwise comparisons of the three conditions (wildtype, dicysteine reduced and dicysteine oxidized). The negative $\log_{10}$ of the p-value is plotted as a function of the $\log_{10}$ of the fold change between the average number of counts in each condition for each protein identified by the proteomic screen. Cutoffs of fold change > 1.5 and $p < 0.05$ are marked with dashed lines.

References

Abdulhay, N.J., Hsieh, L.J., McNally, C.P., Ostrowski, M.S., Moore, C.M., Ketavarapu, M., Kasinathan, S., Nanda, A.S., Wu, K., Chio, U.S., Zhou, Z., Goodarzi, H., Narlikar, G.J., Ramani, V., 2023. Nucleosome density shapes kilobase-scale regulation by a mammalian chromatin remodeler. Nat Struct Mol Biol 30, 1571–1581. https://doi.org/10.1038/s41594-023-01093-6

Abdulhay, N.J., McNally, C.P., Hsieh, L.J., Kasinathan, S., Keith, A., Estes, L.S., Karimzadeh, M., Underwood, J.G., Goodarzi, H., Narlikar, G.J., Ramani, V., 2020. Massively multiplex single-molecule oligonucleosome footprinting. eLife 9. https://doi.org/10.7554/eLife.59404

Abini-Agbomson, S., Gretarsson, K., Shih, R.M., Hsieh, L., Lou, T., De Ioannes, P., Vasilyev, N., Lee, R., Wang, M., Simon, M.D., Armache, J.-P., Nudler, E., Narlikar, G., Liu, S., Lu, C., Armache, K.-J., 2023. Catalytic and non-catalytic mechanisms of histone H4 lysine 20 methyltransferase SUV420H1. Molecular Cell 83, 2872-2883.e7. https://doi.org/10.1016/j.molcel.2023.07.020

Agresti, A., Bianchi, M.E., 2003. HMGB proteins and gene expression. Current Opinion in Genetics & Development 13, 170–178. https://doi.org/10.1016/S0959-437X(03)00023-6

Aizawa, S., Nishino, H., Saito, K., Kimura, K., Shirakawa, H., Yoshida, M., 1994. Stimulation of Transcription in Cultured Cells by High Mobility Group Protein 1: Essential Role of the Acidic Carboxyl-Terminal Region. Biochemistry 33, 14690–14695. https://doi.org/10.1021/bi00253a006

An, W., van Holde, K., Zlatanova, J., 1998. The Non-histone Chromatin Protein HMG1 Protects Linker DNA on the Side Opposite to That Protected by Linker Histones*. Journal of Biological Chemistry 273, 26289–26291. https://doi.org/10.1074/jbc.273.41.26289

Anderson, J.D., Widom, J., 2000. Sequence and position-dependence of the equilibrium accessibility of nucleosomal DNA target sites1. Journal of Molecular Biology 296, 979–987. https://doi.org/10.1006/jmbi.2000.3531

Arimura, Y., Shih, R.M., Froom, R., Funabiki, H., 2021. Structural features of nucleosomes in interphase and metaphase chromosomes. Mol Cell 81, 4377-4397.e12. https://doi.org/10.1016/j.molcel.2021.08.010

Armache, J.P., Gamarra, N., Johnson, S.L., Leonard, J.D., Wu, S., Narlikar, G.J., Cheng, Y., 2019. Cryo-EM structures of remodeler-nucleosome intermediates suggest allosteric control through the nucleosome. eLife 8, e46057. https://doi.org/10.7554/eLife.46057

Armeev, G.A., Kniazeva, A.S., Komarova, G.A., Kirpichnikov, M.P., Shaytan, A.K., 2021. Histone dynamics mediate DNA unwrapping and sliding in nucleosomes. Nat Commun 12, 2387. https://doi.org/10.1038/s41467-021-22636-9

Asarnow, D., Palovcak, E., Cheng, Y., 2019. asarnow/pyem: UCSF pyem v0.5. https://doi.org/10.5281/zenodo.3576630

Balliano, A., Hao, F., Njeri, C., Balakrishnan, L., Hayes, J.J., 2017. HMGB1 Stimulates Activity of Polymerase β on Nucleosome Substrates. Biochemistry 56, 647–656. https://doi.org/10.1021/acs.biochem.6b00569

Bhattacharjee, R.N., Banks, G.C., Trotter, K.W., Lee, H.-L., Archer, T.K., 2001. Histone H1 Phosphorylation by Cdk2 Selectively Modulates Mouse Mammary Tumor Virus Transcription through Chromatin Remodeling. Mol Cell Biol 21, 5417–5425. https://doi.org/10.1128/MCB.21.16.5417-5425.2001

Bilokapic, S., Strauss, M., Halic, M., 2018a. Structural rearrangements of the histone octamer translocate DNA. Nat Commun 9, 1330. https://doi.org/10.1038/s41467-018-03677-z

Bilokapic, S., Strauss, M., Halic, M., 2018b. Histone octamer rearranges to adapt to DNA unwrapping. Nat Struct Mol Biol 25, 101–108. https://doi.org/10.1038/s41594-017-0005-5

Bonaldi, T., Längst, G., Strohner, R., Becker, P.B., Bianchi, M.E., 2002. The DNA chaperone HMGB1 facilitates ACF/CHRAC-dependent nucleosome sliding. EMBO J 21, 6865–6873. https://doi.org/10.1093/emboj/cdf692

Boonyaratanakornkit, V., Melvin, V., Prendergast, P., Altmann, M., Ronfani, L., Bianchi, M.E., Taraseviciene, L., Nordeen, S.K., Allegretto, E.A., Edwards, D.P., 1998. High-Mobility Group Chromatin Proteins 1 and 2 Functionally Interact with Steroid Hormone Receptors To Enhance Their DNA Binding In Vitro and Transcriptional Activity in Mammalian Cells. Mol Cell Biol 18, 4471–4487.

Cai, S., Böck, D., Pilhofer, M., Gan, L., 2018a. The in situ structures of mono-, di-, and trinucleosomes in human heterochromatin. Mol Biol Cell 29, 2450–2457. https://doi.org/10.1091/mbc.E18-05-0331

Cai, S., Chen, C., Tan, Z.Y., Huang, Y., Shi, J., Gan, L., 2018b. Cryo-ET reveals the macromolecular reorganization of S. pombe mitotic chromosomes in vivo. Proc Natl Acad Sci U S A 115, 10977–10982. https://doi.org/10.1073/pnas.1720476115

Cai, S., Song, Y., Chen, C., Shi, J., Gan, L., 2018c. Natural chromatin is heterogeneous and self-associates in vitro. Mol Biol Cell 29, 1652–1663. https://doi.org/10.1091/mbc.E17-07-0449

Catez, F., Yang, H., Tracey, K.J., Reeves, R., Misteli, T., Bustin, M., 2004. Network of Dynamic Interactions between Histone H1 and High-Mobility-Group Proteins in Chromatin. Mol Cell Biol 24, 4321–4328. https://doi.org/10.1128/MCB.24.10.4321-4328.2004

Cato, L., Stott, K., Watson, M., Thomas, J.O., 2008. The Interaction of HMGB1 and Linker Histones Occurs Through their Acidic and Basic Tails. Journal of Molecular Biology 384, 1262–1272. https://doi.org/10.1016/j.jmb.2008.10.001

Celona, B., Weiner, A., Di Felice, F., Mancuso, F.M., Cesarini, E., Rossi, R.L., Gregory, L., Baban, D., Rossetti, G., Grianti, P., Pagani, M., Bonaldi, T., Ragoussis, J., Friedman, N., Camilloni, G., Bianchi, M.E., Agresti, A., 2011. Substantial Histone Reduction Modulates Genomewide Nucleosomal Occupancy and Global Transcriptional Output. PLoS Biol 9, e1001086. https://doi.org/10.1371/journal.pbio.1001086

Chio, U.S., Palovcak, E., Smith, A.A.A., Autzen, H., Muñoz, E.N., Yu, Z., Wang, F., Agard, D.A., Armache, J.-P., Narlikar, G.J., Cheng, Y., 2024. Functionalized graphene-oxide grids enable high-resolution cryo-EM structures of the SNF2h-nucleosome complex without crosslinking. Nat Commun 15, 2225. https://doi.org/10.1038/s41467-024-46178-y

Clapier, C.R., Iwasa, J., Cairns, B.R., Peterson, C.L., 2017. Mechanisms of action and regulation of ATP-dependent chromatin-remodelling complexes. Nat Rev Mol Cell Biol 18, 407–422. https://doi.org/10.1038/nrm.2017.26

Contreras, A., Hale, T.K., Stenoien, D.L., Rosen, J.M., Mancini, M.A., Herrera, R.E., 2003. The Dynamic Mobility of Histone H1 Is Regulated by Cyclin/CDK Phosphorylation. Mol Cell Biol 23, 8626–8636. https://doi.org/10.1128/MCB.23.23.8626-8636.2003

Côté, J., Quinn, J., Workman, J.L., Peterson, C.L., 1994. Stimulation of GAL4 Derivative Binding to Nucleosomal DNA by the Yeast SWI/SNF Complex. Science 265, 53–60. https://doi.org/10.1126/science.8016655

Croll, T.I., 2018. ISOLDE: a physically realistic environment for model building into low-resolution electron-density maps. Acta Cryst D 74, 519–530. https://doi.org/10.1107/S2059798318002425

Das, D., Peterson, R.C., Scovell, W.M., 2004. High Mobility Group B Proteins Facilitate Strong Estrogen Receptor Binding to Classical and Half-Site Estrogen Response Elements and Relax Binding Selectivity. Molecular Endocrinology 18, 2616–2632. https://doi.org/10.1210/me.2004-0125

Decoville, M., Giraud-Panis, M.J., Mosrin-Huaman, C., Leng, M., Locker, D., 2000. HMG boxes of DSP1 protein interact with the Rel homology domain of transcription factors. Nucleic Acids Res 28, 454–462.

Dodonova, S.O., Zhu, F., Dienemann, C., Taipale, J., Cramer, P., 2020. Nucleosome-bound SOX2 and SOX11 structures elucidate pioneer factor function. Nature 580, 669–672. https://doi.org/10.1038/s41586-020-2195-y

Dou, Y., Gorovsky, M.A., 2000. Phosphorylation of Linker Histone H1 Regulates Gene Expression In Vivo by Creating a Charge Patch. Molecular Cell 6, 225–231. https://doi.org/10.1016/S1097-2765(00)00024-1

Dou, Y., Mizzen, C.A., Abrams, M., Allis, C.D., Gorovsky, M.A., 1999. Phosphorylation of Linker Histone H1 Regulates Gene Expression In Vivo by Mimicking H1 Removal. Molecular Cell 4, 641–647. https://doi.org/10.1016/S1097-2765(00)80215-4

Duguet, M., de Recondo, A.M., 1978. A deoxyribonucleic acid unwinding protein isolated from regenerating rat liver. Physical and functional properties. Journal of Biological Chemistry 253, 1660–1666. https://doi.org/10.1016/S0021-9258(17)34916-5

Falciola, L., Spada, F., Calogero, S., Längst, G., Voit, R., Grummt, I., Bianchi, M.E., 1997. High Mobility Group 1 Protein Is Not Stably Associated with the Chromosomes of Somatic Cells. J Cell Biol 137, 19–26.

Frouws, T.D., Barth, P.D., Richmond, T.J., 2018. Site-Specific Disulfide Crosslinked Nucleosomes with Enhanced Stability. Journal of Molecular Biology 430, 45–57. https://doi.org/10.1016/j.jmb.2017.10.029

Fyodorov, D.V., Zhou, B.-R., Skoultchi, A.I., Bai, Y., 2018. Emerging roles of linker histones in regulating chromatin structure and function. Nat Rev Mol Cell Biol 19, 192–206. https://doi.org/10.1038/nrm.2017.94

Gamarra, N., Narlikar, G.J., 2021. Histone dynamics play a critical role in SNF2h-mediated nucleosome sliding. Nat Struct Mol Biol 28, 548–551. https://doi.org/10.1038/s41594-021-00620-7

Ghoneim, M., Fuchs, H.A., Musselman, C.A., 2021. Histone Tail Conformations: A Fuzzy Affair with DNA. Trends in Biochemical Sciences 46, 564–578. https://doi.org/10.1016/j.tibs.2020.12.012

Gibson, B.A., Doolittle, L.K., Schneider, M.W.G., Jensen, L.E., Gamarra, N., Henry, L., Gerlich, D.W., Redding, S., Rosen, M.K., 2019. Organization of Chromatin by Intrinsic and Regulated Phase Separation. Cell 179, 470-484.e21. https://doi.org/10.1016/j.cell.2019.08.037

Hepp, M.I., Alarcon, V., Dutta, A., Workman, J.L., Gutiérrez, J.L., 2014. Nucleosome remodeling by the SWI/SNF complex is enhanced by yeast High Mobility Group Box (HMGB) proteins. Biochim Biophys Acta 1839, 764–772. https://doi.org/10.1016/j.bbagrm.2014.06.014

Hsieh, L.J., Gourdet, M.A., Moore, C.M., Muñoz, E.N., Gamarra, N., Ramani, V., Narlikar, G.J., 2022. A hexasome is the preferred substrate for the INO80 chromatin remodeling complex, allowing versatility of function. Molecular Cell 82, 2098-2112.e4. https://doi.org/10.1016/j.molcel.2022.04.026

Hu, Q., Botuyan, M.V., Zhao, D., Cui, G., Mer, E., Mer, G., 2021. Mechanisms of BRCA1–BARD1 nucleosome recognition and ubiquitylation. Nature 596, 438–443. https://doi.org/10.1038/s41586-021-03716-8

Imbalzano, A.N., Kwon, H., Green, M.R., Kingston, R.E., 1994. Facilitated binding of TATA-binding protein to nucleosomal DNA. Nature 370, 481–485. https://doi.org/10.1038/370481a0

Jayaraman, L., Moorthy, N.C., Murthy, K.G.K., Manley, J.L., Bustin, M., Prives, C., 1998. High mobility group protein-1 (HMG-1) is a unique activator of p53. Genes Dev 12, 462–472.

Joshi, S.R., Ghattamaneni, R.B., Scovell, W.M., 2011. Expanding the Paradigm for Estrogen Receptor Binding and Transcriptional Activation. Molecular Endocrinology 25, 980–994. https://doi.org/10.1210/me.2010-0302

Joshi, S.R., Sarpong, Y.C., Peterson, R.C., Scovell, W.M., 2012. Nucleosome dynamics: HMGB1 relaxes canonical nucleosome structure to facilitate estrogen receptor binding. Nucleic Acids Res 40, 10161–10171. https://doi.org/10.1093/nar/gks815

Ju, B.-G., Lunyak, V.V., Perissi, V., Garcia-Bassets, I., Rose, D.W., Glass, C.K., Rosenfeld, M.G., 2006. A Topoisomerase IIß-Mediated dsDNA Break Required for Regulated Transcription. Science 312, 1798–1802. https://doi.org/10.1126/science.1127196

Kato, H., van Ingen, H., Zhou, B.-R., Feng, H., Bustin, M., Kay, L.E., Bai, Y., 2011. Architecture of the high mobility group nucleosomal protein 2-nucleosome complex as revealed by methyl-based NMR. Proceedings of the National Academy of Sciences 108, 12283–12288. https://doi.org/10.1073/pnas.1105848108

Kawase, T., Sato, K., Ueda, T., Yoshida, M., 2008. Distinct Domains in HMGB1 Are Involved in Specific Intramolecular and Nucleosomal Interactions. Biochemistry 47, 13991–13996. https://doi.org/10.1021/bi8013449

Kitevski-LeBlanc, J.L., Yuwen, T., Dyer, P.N., Rudolph, J., Luger, K., Kay, L.E., 2018. Investigating the Dynamics of Destabilized Nucleosomes Using Methyl-TROSY NMR. J. Am. Chem. Soc. 140, 4774–4777. https://doi.org/10.1021/jacs.8b00931

Knapp, S., Müller, S., Digilio, G., Bonaldi, T., Bianchi, M.E., Musco, G., 2004. The Long Acidic Tail of High Mobility Group Box 1 (HMGB1) Protein Forms an Extended and Flexible Structure That Interacts with Specific Residues within and between the HMG Boxes. Biochemistry 43, 11992–11997. https://doi.org/10.1021/bi049364k

Kwon, H., Imbalzano, A.N., Khavari, P.A., Kingston, R.E., Green, M.R., 1994. Nucleosome disruption and enhancement of activator binding by a human SW1/SNF complex. Nature 370, 477–481. https://doi.org/10.1038/370477a0

Lange, S.S., Mitchell, D.L., Vasquez, K.M., 2008. High mobility group protein B1 enhances DNA repair and chromatin modification after DNA damage. Proceedings of the National Academy of Sciences 105, 10320–10325. https://doi.org/10.1073/pnas.0803181105

Li, H., 2018. Minimap2: pairwise alignment for nucleotide sequences. Bioinformatics 34, 3094–3100. https://doi.org/10.1093/bioinformatics/bty191

Lorch, Y., Cairns, B.R., Zhang, M., Kornberg, R.D., 1998. Activated RSC–Nucleosome Complex and Persistently Altered Form of the Nucleosome. Cell 94, 29–34. https://doi.org/10.1016/S0092-8674(00)81218-0

Lorch, Y., LaPointe, J.W., Kornberg, R.D., 1987. Nucleosomes inhibit the initiation of transcription but allow chain elongation with the displacement of histones. Cell 49, 203–210. https://doi.org/10.1016/0092-8674(87)90561-7

Luger, K., Mäder, A.W., Richmond, R.K., Sargent, D.F., Richmond, T.J., 1997. Crystal structure of the nucleosome core particle at 2.8 Å resolution. Nature 389, 251–260. https://doi.org/10.1038/38444

Luger, K., Rechsteiner, T.J., Richmond, T.J., 1999. Preparation of nucleosome core particle from recombinant histones, in: Methods in Enzymology, Chromatin. Academic Press, pp. 3–19. https://doi.org/10.1016/S0076-6879(99)04003-3

McCauley, M.J., Huo, R., Becker, N., Holte, M.N., Muthurajan, U.M., Rouzina, I., Luger, K., Maher, L.J., Israeloff, N.E., Williams, M.C., 2019. Single and double box HMGB proteins differentially destabilize nucleosomes. Nucleic Acids Res 47, 666–678. https://doi.org/10.1093/nar/gky1119

McCauley, M.J., Zimmerman, J., Maher, L.J., C.Williams, M., 2007. HMGB Binding to DNA: Single and Double Box Motifs. J Mol Biol 374, 993–1004. https://doi.org/10.1016/j.jmb.2007.09.073

Meshorer, E., Yellajoshula, D., George, E., Scambler, P.J., Brown, D.T., Misteli, T., 2006. Hyperdynamic Plasticity of Chromatin Proteins in Pluripotent Embryonic Stem Cells. Dev Cell 10, 105–116. https://doi.org/10.1016/j.devcel.2005.10.017

Müller, S., Ronfani, L., Bianchi, M.E., 2004. Regulated expression and subcellular localization of HMGB1, a chromatin protein with a cytokine function. Journal of Internal Medicine 255, 332–343. https://doi.org/10.1111/j.1365-2796.2003.01296.x

Ner, S.S., Travers, A.A., 1994. HMG-D, the Drosophila melanogaster homologue of HMG 1 protein, is associated with early embryonic chromatin in the absence of histone H1. EMBO J 13, 1817–1822.

Ngo, T.T.M., Zhang, Q., Zhou, R., Yodh, J.G., Ha, T., 2015. Asymmetric Unwrapping of Nucleosomes under Tension Directed by DNA Local Flexibility. Cell 160, 1135–1144. https://doi.org/10.1016/j.cell.2015.02.001

Nightingale, K., Dimitrov, S., Reeves, R., Wolffe, A.P., 1996. Evidence for a shared structural role for HMG1 and linker histones B4 and H1 in organizing chromatin. EMBO J 15, 548–561.

Nilsen, T.W., 2013. Preparation of Nuclear Extracts from HeLa Cells. Cold Spring Harb Protoc 2013, pdb.prot075176. https://doi.org/10.1101/pdb.prot075176

Ogawa, Y., Aizawa, S., Shirakawa, H., Yoshida, M., 1995. Stimulation of Transcription Accompanying Relaxation of Chromatin Structure in Cells Overexpressing High Mobility Group 1 Protein *. Journal of Biological Chemistry 270, 9272–9280. https://doi.org/10.1074/jbc.270.16.9272

Okuwaki, M., Kato, K., Nagata, K., 2010. Functional characterization of human nucleosome assembly protein 1-like proteins as histone chaperones. Genes to Cells 15, 13–27. https://doi.org/10.1111/j.1365-2443.2009.01361.x

Oñate, S.A., Prendergast, P., Wagner, J.P., Nissen, M., Reeves, R., Pettijohn, D.E., Edwards, D.P., 1994. The DNA-bending protein HMG-1 enhances progesterone receptor binding to its target DNA sequences. Mol Cell Biol 14, 3376–3391.

Osmanov, T., Ugrinova, I., Pasheva, E., 2013. The chaperone like function of the nonhistone protein HMGB1. Biochemical and Biophysical Research Communications 432, 231–235. https://doi.org/10.1016/j.bbrc.2013.02.008

Patenge, N., Elkin, S.K., Oettinger, M.A., 2004. ATP-dependent Remodeling by SWI/SNF and ISWI Proteins Stimulates V(D)J Cleavage of 5 S Arrays*. Journal of Biological Chemistry 279, 35360–35367. https://doi.org/10.1074/jbc.M405790200

Phair, R.D., Scaffidi, P., Elbi, C., Vecerová, J., Dey, A., Ozato, K., Brown, D.T., Hager, G., Bustin, M., Misteli, T., 2004. Global Nature of Dynamic Protein-Chromatin Interactions In Vivo: Three-Dimensional Genome Scanning and Dynamic Interaction Networks of Chromatin Proteins. Mol Cell Biol 24, 6393–6402. https://doi.org/10.1128/MCB.24.14.6393-6402.2004

Polach, K.J., Lowary, P.T., Widom, J., 2000. Effects of core histone tail domains on the equilibrium constants for dynamic dna site accessibility in nucleosomes1. Journal of Molecular Biology 298, 211–223. https://doi.org/10.1006/jmbi.2000.3644

Polach, K.J., Widom, J., 1995. Mechanism of Protein Access to Specific DNA Sequences in Chromatin: A Dynamic Equilibrium Model for Gene Regulation. Journal of Molecular Biology 254, 130–149. https://doi.org/10.1006/jmbi.1995.0606

Prior, C.P., Cantor, C.R., Johnson, E.M., Littau, V.C., Allfrey, V.G., 1983. Reversible changes in nucleosome structure and histone H3 accessibility in transcriptionally active and inactive states of rDNA chromatin. Cell 34, 1033–1042. https://doi.org/10.1016/0092-8674(83)90561-5

Punjani, A., Rubinstein, J.L., Fleet, D.J., Brubaker, M.A., 2017. cryoSPARC: algorithms for rapid unsupervised cryo-EM structure determination. Nat Methods 14, 290–296. https://doi.org/10.1038/nmeth.4169

Ragab, A., Travers, A., 2003. HMG-D and histone H1 alter the local accessibility of nucleosomal DNA. Nucleic Acids Res 31, 7083–7089. https://doi.org/10.1093/nar/gkg923

Robinson, P.J.J., Fairall, L., Huynh, V.A.T., Rhodes, D., 2006. EM measurements define the dimensions of the “30-nm” chromatin fiber: Evidence for a compact, interdigitated structure. Proceedings of the National Academy of Sciences 103, 6506–6511. https://doi.org/10.1073/pnas.0601212103

Rosenzweig, R., Kay, L.E., 2014. Bringing Dynamic Molecular Machines into Focus by Methyl-TROSY NMR. Annu. Rev. Biochem. 83, 291–315. https://doi.org/10.1146/annurev-biochem-060713-035829

Sánchez-Giraldo, R., Acosta-Reyes, F.J., Malarkey, C.S., Saperas, N., Churchill, M.E.A., Campos, J.L., 2015. Two high-mobility group box domains act together to underwind and kink DNA. Acta Cryst D 71, 1423–1432. https://doi.org/10.1107/S1399004715007452

Sanulli, S., Trnka, M.J., Dharmarajan, V., Tibble, R.W., Pascal, B.D., Burlingame, A.L., Griffin, P.R., Gross, J.D., Narlikar, G.J., 2019. HP1 reshapes nucleosome core to promote phase separation of heterochromatin. Nature 575, 390–394. https://doi.org/10.1038/s41586-019-1669-2

Scaffidi, P., Misteli, T., Bianchi, M.E., 2002. Release of chromatin protein HMGB1 by necrotic cells triggers inflammation. Nature 418, 191–195. https://doi.org/10.1038/nature00858

Scheres, S.H.W., 2012. RELION: Implementation of a Bayesian approach to cryo-EM structure determination. Journal of Structural Biology 180, 519–530. https://doi.org/10.1016/j.jsb.2012.09.006

Sinha, K.K., Gross, J.D., Narlikar, G.J., 2017. Distortion of histone octamer core promotes nucleosome mobilization by a chromatin remodeler. Science 355, eaaa3761. https://doi.org/10.1126/science.aaa3761

Skrajna, A., Goldfarb, D., Kedziora, K.M., Cousins, E.M., Grant, G.D., Spangler, C.J., Barbour, E.H., Yan, X., Hathaway, N.A., Brown, N.G., Cook, J.G., Major, M.B., McGinty, R.K., 2020. Comprehensive nucleosome interactome screen establishes fundamental principles of nucleosome binding. Nucleic Acids Research 48, 9415–9432. https://doi.org/10.1093/nar/gkaa544

Sobhian, B., Shao, G., Lilli, D.R., Culhane, A.C., Moreau, L.A., Xia, B., Livingston, D.M., Greenberg, R.A., 2007. RAP80 Targets BRCA1 to Specific Ubiquitin Structures at DNA Damage Sites. Science 316, 1198–1202. https://doi.org/10.1126/science.1139516

Sofiadis, K., Josipovic, N., Nikolic, M., Kargapolova, Y., Übelmesser, N., Varamogianni-Mamatsi, V., Zirkel, A., Papadionysiou, I., Loughran, G., Keane, J., Michel, A., Gusmao, E.G., Becker, C., Altmüller, J., Georgomanolis, T., Mizi, A., Papantonis, A., 2021. HMGB1 coordinates SASP-related chromatin folding and RNA homeostasis on the path to senescence. Mol Syst Biol 17, e9760. https://doi.org/10.15252/msb.20209760

Song, F., Chen, P., Sun, D., Wang, M., Dong, L., Liang, D., Xu, R.-M., Zhu, P., Li, G., 2014. Cryo-EM Study of the Chromatin Fiber Reveals a Double Helix Twisted by Tetranucleosomal Units. Science 344, 376–380. https://doi.org/10.1126/science.1251413

Stott, K., Tang, G.S.F., Lee, K.-B., Thomas, J.O., 2006. Structure of a Complex of Tandem HMG Boxes and DNA. Journal of Molecular Biology 360, 90–104. https://doi.org/10.1016/j.jmb.2006.04.059

Stott, K., Watson, M., Howe, F.S., Grossmann, J.G., Thomas, J.O., 2010. Tail-Mediated Collapse of HMGB1 Is Dynamic and Occurs *via* Differential Binding of the Acidic Tail to the A and B Domains. Journal of Molecular Biology 403, 706–722. https://doi.org/10.1016/j.jmb.2010.07.045

Syed, S.H., Goutte-Gattat, D., Becker, N., Meyer, S., Shukla, M.S., Hayes, J.J., Everaers, R., Angelov, D., Bednar, J., Dimitrov, S., 2010. Single-base resolution mapping of H1–nucleosome interactions and 3D organization of the nucleosome. Proceedings of the National Academy of Sciences 107, 9620–9625. https://doi.org/10.1073/pnas.1000309107

Tan, Z.Y., Cai, S., Noble, A.J., Chen, J.K., Shi, J., Gan, L., 2023. Heterogeneous non-canonical nucleosomes predominate in yeast cells in situ. eLife 12, RP87672. https://doi.org/10.7554/eLife.87672

Teo, S.-H., Grasser, K.D., Thomas, J.O., 1995. Differences in the DNA-Binding Properties of the Hmg-Box Domains of HMG1 and the Sex-Determining Factor SRY. European Journal of Biochemistry 230, 943–950. https://doi.org/10.1111/j.1432-1033.1995.0943g.x

Thomas, J.O., Stott, K., 2012. H1 and HMGB1: modulators of chromatin structure. Biochemical Society Transactions 40, 341–346. https://doi.org/10.1042/BST20120014

Thomas, J.O., Travers, A.A., 2001. HMG1 and 2, and related 'architectural' DNA-binding proteins. Trends in Biochemical Sciences 26, 167–174. https://doi.org/10.1016/S0968-0004(01)01801-1

Travers, A.A., 2003. Priming the nucleosome: a role for HMGB proteins? EMBO Rep 4, 131–136. https://doi.org/10.1038/sj.embor.embor741

Tugarinov, V., Hwang, P.M., Ollerenshaw, J.E., Kay, L.E., 2003. Cross-Correlated Relaxation Enhanced 1H−13C NMR Spectroscopy of Methyl Groups in Very High Molecular Weight Proteins and Protein Complexes. J. Am. Chem. Soc. 125, 10420–10428. https://doi.org/10.1021/ja030153x

Ueda, T., Chou, H., Kawase, T., Shirakawa, H., Yoshida, M., 2004. Acidic C-Tail of HMGB1 Is Required for Its Target Binding to Nucleosome Linker DNA and Transcription Stimulation. Biochemistry 43, 9901–9908. https://doi.org/10.1021/bi035975l

Ugrinova, I., Pashev, I.G., Pasheva, E.A., 2009. Nucleosome Binding Properties and Co-Remodeling Activities of Native and in Vivo Acetylated HMGB-1 and HMGB-2 Proteins. Biochemistry 48, 6502–6507. https://doi.org/10.1021/bi9004304

Watson, M., Stott, K., Fischl, H., Cato, L., Thomas, J.O., 2014. Characterization of the interaction between HMGB1 and H3—a possible means of positioning HMGB1 in chromatin. Nucleic Acids Res 42, 848–859. https://doi.org/10.1093/nar/gkt950

Watson, M., Stott, K., Thomas, J.O., 2007. Mapping Intramolecular Interactions between Domains in HMGB1 using a Tail-truncation Approach. Journal of Molecular Biology 374, 1286–1297. https://doi.org/10.1016/j.jmb.2007.09.075

White, A.E., Hieb, A.R., Luger, K., 2016. A quantitative investigation of linker histone interactions with nucleosomes and chromatin. Sci Rep 6, 19122. https://doi.org/10.1038/srep19122

Winkler, D.D., Luger, K., 2011. The Histone Chaperone FACT: Structural Insights and Mechanisms for Nucleosome Reorganization. Journal of Biological Chemistry 286, 18369–18374. https://doi.org/10.1074/jbc.R110.180778

Wu, H., Muñoz, E.N., Hsieh, L.J., Chio, U.S., Gourdet, M.A., Narlikar, G.J., Cheng, Y., 2023. Reorientation of INO80 on hexasomes reveals basis for mechanistic versatility. Science 381, 319–324. https://doi.org/10.1126/science.adf4197

Wu, J., Huen, M.S.Y., Lu, L.-Y., Ye, L., Dou, Y., Ljungman, M., Chen, J., Yu, X., 2009. Histone Ubiquitination Associates with BRCA1-Dependent DNA Damage Response. Mol Cell Biol 29, 849–860. https://doi.org/10.1128/MCB.01302-08

Zappavigna, V., Falciola, L., Helmer-Citterich, M., Mavilio, F., Bianchi, M.E., 1996. HMG1 interacts with HOX proteins and enhances their DNA binding and transcriptional activation. EMBO J 15, 4981–4991.

Zheng, S.Q., Palovcak, E., Armache, J.-P., Verba, K.A., Cheng, Y., Agard, D.A., 2017. MotionCor2: anisotropic correction of beam-induced motion for improved cryo-electron microscopy. Nat Methods 14, 331–332. https://doi.org/10.1038/nmeth.4193

Zhong, E.D., Bepler, T., Berger, B., Davis, J.H., 2021. CryoDRGN: reconstruction of heterogeneous cryo-EM structures using neural networks. Nat Methods 18, 176–185. https://doi.org/10.1038/s41592-020-01049-4

Zhou, B.-R., Feng, H., Kato, H., Dai, L., Yang, Y., Zhou, Y., Bai, Y., 2013. Structural insights into the histone H1-nucleosome complex. Proceedings of the National Academy of Sciences 110, 19390–19395. https://doi.org/10.1073/pnas.1314905110

Zwilling, S., König, H., Wirth, T., 1995. High mobility group protein 2 functionally interacts with the POU domains of octamer transcription factors. EMBO J 14, 1198–1208.

Publishing Agreement

It is the policy of the University to encourage open access and broad distribution of all theses, dissertations, and manuscripts. The Graduate Division will facilitate the distribution of UCSF theses, dissertations, and manuscripts to the UCSF Library for open access and distribution. UCSF will make such theses, dissertations, and manuscripts accessible to the public and will take reasonable steps to preserve these works in perpetuity.

I hereby grant the non-exclusive, perpetual right to The Regents of the University of California to reproduce, publicly display, distribute, preserve, and publish copies of my thesis, dissertation, or manuscript in any form or media, now existing or later derived, including access online for teaching, research, and public service purposes.

DocuSigned by:
Hayden Saunders
67DC01135CAD4AA
Author Signature

11/14/2024
Date